DIPLOMARBEIT

Evaluation of multi-photon induced grafting and cleaving as methods to spatially guide cell migration in gelatin-based hydrogels

ausgeführt zum Zwecke der Erlangung des akademischen Grades eines Diplom-Ingenieurs
unter der Leitung von

Prof. Dr.rer.nat. Aleksandr Ovsianikov

E308 - Institut für Werkstoffwissenschaften und Werkstofftechnologie

Eingereicht an der Technischen Universität Wien
Fakultät für Maschinenwesen und Betriebswissenschaften

von

Simon Laurent Sayer
01309249
Helferstorferstraße 5
1010 Wien

Wien, Dezember 2020

Ich nehme zur Kenntnis, dass ich zur Drucklegung meiner Arbeit unter der Bezeichnung

Diplomarbeit

nur mit Bewilligung der Prüfungskommission berechtigt bin.

Ich erkläre an Eides statt, dass die vorliegende Arbeit nach den anerkannten Grundsätzen für wissenschaftliche Abhandlungen von mir selbstständig erstellt wurde. Alle verwendeten Hilfsmittel, insbesondere die zugrunde gelegte Literatur, sind in dieser Arbeit genannt und aufgelistet. Die aus den Quellen wörtlich entnommenen Stellen, sind als solche kenntlich gemacht.

Das Thema dieser Arbeit wurde von mir bisher weder im In- noch Ausland einer Beurteilerin/einem Beurteiler zur Begutachtung in irgendeiner Form als Prüfungsarbeit vorgelegt. Diese Arbeit stimmt mit der von den Begutachterinnen/Begutachtern beurteilten Arbeit überein.

Wien, im Dezember 2020

Simon Laurent Sayer

Abstract

Hydrogels can assume the role of the extra cellular matrix and enable cell-to-cell and cell-to-matrix interactions. Advances in various biofabrication techniques are facilitating the creation of biomimetic materials with distinct biochemical and biophysical characteristics. As important as the fine-tuning of the hydrogel as a whole is the creation of an individual microenvironment within which the cells reside. To that end, multi-photon lithography is a promising tool that enables the modification of transparent cell-laden hydrogels at a micrometer resolution in an arbitrary three-dimensional manner. The aim of this thesis was to analyze two multi-photon lithography-based methods, namely photografting and photocleaving, for their potential to induce directional cell migration and subsequently directional endothelial sprouting. Multi-photon induced photografting is a universal technique that can be applied to any hydrogel without the requirement of specific functional groups. It refers to the local immobilization of a molecule on the backbone of a polymer upon multi-photon absorption. Multi-photon induced photocleaving utilizes crosslinkers that are containing photocleavable moieties, which allows to locally reverse the crosslinking process upon multi-photon absorption. By adding a multi-photon sensitizer the cleaving threshold can be decreased to cytocompatible laser powers. In a first step, different gelatin-based hydrogels have been selected and the cytocompatability of the respective materials has been assessed. For the most promising combination, which was photocleaving in gelatin methacryloyl, various parameters have been tested for their potential to enhance the induced directionality of cell migration.

Kurzfassung

Hydrogele können die Rolle der extrazellulären Matrix übernehmen und dadurch Interaktionen zwischen den Zellen untereinander und den Zellen und der Matrix ermöglichen. Fortschritte in verschiedenen Biofabrikationstechniken erleichtern die Herstellung biomimetischer Materialien mit speziellen biochemischen und biophysikalischen Eigenschaften. Ebenso wichtig wie die Feinabstimmung des gesamten Hydrogels ist die Schaffung einer individuellen Mikroumgebung, in der sich die Zellen befinden. Zu diesem Zweck ist die Multi-Photonen-Lithographie ein vielversprechendes Werkzeug, das die Modifizierung transparenter, zellbeladener Hydrogele mit einer Auflösung im Mikrometerbereich in einer beliebigen dreidimensionalen Art und Weise ermöglicht. Ziel dieser Arbeit war es, zwei auf der Multi-Photonen-Lithographie basierende Methoden, nämlich das Photografting und das Photocleaving, auf ihr Potenzial zu analysieren, eine gerichtete Zellmigration und anschließend eine gerichtete Endothelzellensprossung zu induzieren. Das Multi-Photonen-induzierte Photografting ist ein universelles Verfahren, das auf jedes Hydrogel angewendet werden kann, ohne dass spezifische funktionelle Gruppen erforderlich sind. Es bezieht sich auf die lokale kovalente Bindung eines Moleküls an eine Polymerkette infolge einer Multi-Photonen-Absorption. Bei der Multiphotonen-induzierten Photospaltung werden Crosslinker verwendet, die photospaltbare Anteile enthalten, wodurch der Vernetzungsprozess infolge einer Multiphotonen-Absorption lokal umgekehrt werden kann. Durch Hinzufügen eines Mehrphotonen-Sensibilisators kann die Reaktionsschwelle auf zytokompatible Laserleistungen herabgesetzt werden. In einem ersten Schritt wurden verschiedene gelatine-basierte Hydrogele ausgewählt und die Zytokompatibilität der jeweiligen Materialien bewertet. Für die vielversprechendste Kombination, das Photografting in Gelatine-Methacryloyl, wurden verschiedene Parameter auf ihr Potential zur Verbesserung der induzierten Richtungsabhängigkeit der Zellmigration getestet.

Acknowledgement

First of all, I would like to thank Aleksandr Ovsianikov for giving me the opportunity to work in the fascinating field of biofabrication and for always guiding me in the right direction during the research.

What made the past year especially remarkable, was the whole team of the research group for 3D Printing and Biofabrication. They always offered a helping hand and it was a great experience to work with talented people from different disciplines.

I want to express my gratitude to my supervisor Tommaso Zandrini, who supported me in all aspects of the thesis and to Marica Markovic, who taught me a lot about working with cells and performed many of the experiments together with me. They have both contributed significantly to this thesis.

Contents

List of Figures viii

List of Tables ix

1 Introduction 1

2 Theoretical Background 4
2.1 Extracellular matrix . . . 4
2.2 Three-dimensional cell culture systems . . . 4
2.2.1 Microenvironment and durotaxis . . . 6
2.3 Blood vessels . . . 9
2.3.1 Natural formation of blood vessels . . . 10
2.4 Tissue engineering . . . 14
2.4.1 Vascular tissue engineering . . . 16
2.5 Multi-photon lithography . . . 18
2.5.1 Multi-photon absorption . . . 18
2.5.2 Multi-photon lithography system . . . 19
2.5.3 Multi-photon induced grafting . . . 20
2.5.4 Multi-photon induced cleaving . . . 21

3 Materials 22
3.1 Hydrogels . . . 22
3.1.1 Gelatin methacryloyl . . . 22
3.1.2 Collagen type 1 . . . 23
3.1.3 Thiolated gelatin . . . 23
3.2 Cell culture . . . 24
3.2.1 Human adipose-derived stem cells . . . 24
3.2.2 Human umbilical vein endothelial cells . . . 24
3.3 Li-TPO-L photoinitiator . . . 25
3.4 DSSA photografting agent . . . 25
3.5 PEG-(oNB-A)$_2$ photocleavable crosslinker . . . 25
3.6 DAS multi-photon sensitizer . . . 25

4 Methods 27
4.1 Spheroid formation . . . 27
4.1.1 Methyl cellulose . . . 27
4.1.2 Casting of agarose molds . . . 27
4.1.3 Cell seeding . . . 27
4.2 Functionalization of microscopy dishes . . . 28

4.3 Hydrogel preparation . . . 28
4.3.1 Gelatin methacryloyl - photografting . . . 28
4.3.2 Collagen type 1 - photografting . . . 29
4.3.3 Thiolated gelatin - photocleaving . . . 29
4.4 Analytical biochemical assays . . . 29
4.4.1 PrestoBlue cell viability assay . . . 29
4.4.2 Live/ dead staining . . . 30
4.4.3 Ki67 staining . . . 31
4.5 Printing procedure . . . 31
4.6 Image acquisition . . . 32
4.7 Statistical analysis . . . 32

5 Results and Discussion **34**
5.1 Photocleaving of thiolated gelatin to induce guided cell migration . . . 34
5.1.1 PEG-(oNB-A)$_2$ cytotoxicity . . . 34
5.1.2 Guided cell migration . . . 37
5.2 Photografting of gelatin methacryloyl to induce guided cell migration . . . 39
5.2.1 Material modification . . . 39
5.2.2 Threshold test . . . 40
5.2.3 DSSA cytotoxicity . . . 41
5.2.4 Effect of hydrogel concentration on cell behavior . . . 42
5.2.5 Cell alignment . . . 46
5.2.6 Parameter optimization . . . 47
5.2.7 Guided cell migration . . . 59
5.3 Photografting of collagen type 1 to induce guided cell migration . . . 61
5.3.1 Concentration and threshold test . . . 61
5.3.2 Problems and perspectives . . . 62

6 Outlook and Conclusion **63**

References **83**

Abbreviations **84**

List of Figures

2.1 Illustration of the cell microenvironment 6
2.2 Illustration of adaptable parameters for ECM-mimicking biomaterials . . . 8
2.3 Illustration of mural cells on the cerebral vasculature 10
2.4 Illustration of the mechanisms of blood vessel formation 12
2.5 Illustration of the hierarchical structure of the vascular tree 16
2.6 Illustration of the principal behind multi-photon lithography 19
2.7 Illustration of the multi-photon lithography setup 20

3.1 Illustration of synthesis and photopolimerization of gel-MA 23
3.2 Illustration of the chemical structure, Michael-type thiol-ene addition and the photocleaving process of (PEG-(oNB-A)$_2$ 26

5.1 Determination of cytotoxic behavior of DAS on HUVECs 35
5.2 Cell behavior in response to oNB moieties 36
5.3 Migration of GFP-ASCs into photocleaved microchannels in gel-SH ds 56 . 38
5.4 Threshold test for photografting in 5% gel-MA ds 63 for a DSSA soaking time of 2 hours 40
5.5 Threshold test for photografting in 5% gel-MA ds 63 for a DSSA soaking time of 24 hours 41
5.6 Determination of cytotoxic behavior of DSSA with a PrestoBlue cell viability assay 42
5.7 Quantification of the proliferation of ASCs encapsulated in gel-MA ds 63 . 43
5.8 Live/dead staining of ASCs encapsulated in gel-MA ds 63 on day 1 44
5.9 Live/dead staining of ASCs encapsulated in gel-MA ds 63 on day 7 45
5.10 Quantification of metabolic activity of ASCs encapsulated in gel-MA ds 63 46
5.11 Alignment of GFP-ASCs to photografted mesh-like structures 47
5.12 Overview of the different printing designs 49
5.13 Migration of ASCs (suspension) and RFP-HUVECs (spheroid) into photografted microchannels in gel-MA ds 63 51
5.14 Effect of gel-MA ds 63 concentration on cell migration into photografted microchannels 53
5.15 Effect of coculture ratio and early/ late encapsulation on cell migration into photografted microchannels 55
5.16 Effect of coculture ratio on cell migration into photografted microchannels 57
5.17 Quantificaton of the migration distance over time 58
5.18 Migration of GFP-ASCs into photografted microchannels in gel-MA ds 63 . 59
5.19 Migration of GFP-ASCs and RFP-HUVECs into photografted microchannels in gel-MA ds 63 60
5.20 Threshold test for photografting in collagen type 1 61

List of Tables

2.1 Overview of the different endothelial cell types used in VTE 17

1 Introduction

Hydrogels are crosslinked hydrophilic polymer chains with a high swelling ratio and permeability [1]. They can provide an environment which enables cell-to-cell and cell-to-matrix interactions by assuming the role of the extra cellular matrix (ECM). This reduces the difference between the physiological environment and cell cultures [2]. Besides providing a homogeneous platform in which cells are behaving more similarly to the natural conditions, subsequently improving the transferability of *in vitro* research, in areas such as drug development, to the actual *in vivo* effect, advances in techniques relying on the local modification of the cell-laden matrix allow for the adaption of the individual cells' microenvironments [3], [4].

The ECM is a key aspect of the cell's microenvironment and can differ in terms of the composition and the biochemical (e.g. chemical functional groups) and biophysical parameters (e.g. mechanical stiffness, degradability) [5]. *In vitro* studies have shown that these factors influence cell behavior and functions, such as migration [6], proliferation [7], [8], differentiation [9], gene and protein expression [10], polarity and apoptosis [11]. Various studies have demonstrated that the matrix stiffness can have a distinct impact on cell proliferation, differentiation and motility [6, 7, 12]. The influence on the migration behavior of motile cells has been extensively studied. In a two-dimensional (2D) setup, with hydrogels of different bulk stiffnesses, cells have been seeded on top of the hydrogels and the subsequent migration has been observed over time. These studies have shown, that the matrix stiffness has an effect on the migration speed of cells [13]–[15]. By creating an inhomogeneous stiffness distribution, Lo et al. [16] have demonstrated that cells can be guided by a stiffness gradient. They termed this stiffness-dependent cell migration durotaxis. Further studies have taken a similar approach, with cells seeded on a 2D substrate with an inherent stiffness gradient, thereby confirming the preceding results [17], [18].

During embryonic development, wound healing and tumor growth, new blood vessels are formed from existing ones. This process, called angiogenesis, relies on cell-to-matrix interactions and the remodeling of the ECM [19]. The physiochemical properties of the matrix as well as the entire microenvironment play a crucial role in the regulation of angiogenesis [20]. A functioning blood vessel network is necessary to maintain homeostasis and facilitate the exchange of oxygen, nutrients, biochemicals and waste. Moreover, it seems that it also acts as a structural template and thereby influences the organization of tissue [21], [22]. The diffusion range of oxygen (100-200 µm) is the limiting factor to the size of implantable engineered tissue [23], [24]. Although the host vasculature will generally grow into the tissue and form a network, this process can be very slow, subjecting parts of the tissue to oxygen and nutrient deficiency for a size-dependent time period [25], [26]. Despite the importance of vascularization in tissue engineering, it remains one of the biggest challenges in the field [27].

Besides the natural organization of endothelial cells, which relies on remodeling after implantation and offers most likely no clear area for anastomosis, there are many different approaches to control vascularization [28]. These approaches range from different patterning techniques, such as the formation and subsequent seeding of hollow channels, the micropatterning by means such as photopatterning [29], 3D bioprinting [30] or electrospinning [31], to cell guiding approaches, where either biochemical signals, mechanobiological cues [32] or a spatial inhomogeneity of the ECM mimicking scaffold's material properties [8], [33], are responsible for the preferential migration and sprouting of endothelial cells. Further areas of application for the fabrication of *in vitro* vessels, besides implantable tissue, are organs-on-a-chip [34], platforms for studying blood vessel formation under physiological [35] and pathological conditions [36] and setups for observing endothelial cell functions and interactions [37].

The human vasculature is a complex, hierarchical system with a feature size that ranges over three orders of magnitude. Arterioles, capillaries and venules are the constituents of what is called the microcirculation. Capillaries, the smallest and most numerous blood vessels in the body, have an inner diameter between 5-10 µm and a very thin vessel wall [38]. Some vascular tissue engineering techniques, such as sheet rolling and tubular molding, are not suitable for the fabrication of vessels at the necessary micrometer scale [39]. Others, such as embedded bioprinting [40], inkjet bioprinting [41] or extrusion bioprinting [42] are capable of producing vessels at a spatial resolution that is sufficient for arterioles and venules but not for capillaries and are limited in the 3D control. The biofabrication of microvessels is therefore reliant on biocompatible techniques that allow for the creation of complex structures at a sufficiently high resolution.

In general, light-based techniques are an exception with their ability to create vessels at relevant sizes for capillaries, venules and arterioles (5-100 µm) and their comparatively high cell viability [39]. Laser-induced forward transfer (LIFT) [43] and digital light processing (DLP) [44] meet those criteria, but they are limited in their ability to create fully arbitrary 3D structures.

Multi-photon lithography, a process by which a femtosecond (fs) near-infrared laser is focused through an objective, can initiate a photochemical reaction at a nanometer resolution, in an arbitrary 3D manner within transparent materials. The high-resolution and 3D-nature of the process are achieved due to the non-linear relation between the distance from the focal point and the probability of multi-photon absorption. Multi-photon lithography has been used for the selective polymerization of materials, to create microporous scaffolds [45] or branched tubular structures [46]. Various multi-photon lithography approaches are applicable to already formed structures. Hydrogels can be patterned with chemical functionalities, by covalent crosslinking [47] or photocaging [48], previously formed crosslinks can be degraded [49] or the material can be densified upon multi-photon absorption [50]. Another method is photoablation, which is the degradation of a material through the photolysis of nonspecific chemical bonds, extreme local heating or microcavitation [51], [52].

This thesis explores the potential of two multi-photon lithography-based methods, namely photografting and photocleaving, for their potential to induce directional adipose-derived stem cell (ASC) and human umbilical vein endothelial cell (HUVEC) migration. In a first step, suitable hydrogels have been selected and the biocompatibility of the approaches has been analyzed. This was followed by a fine tuning of relevant parameters, such as several printing parameters, most notably the laser power, the material concentration, the cell encapsulation method, the design of the grafted structure and the cell ratios in coculture setups. It has been previously shown that ASC and HUVEC coculture spheroids form endothelial sprouts and subsequently assemble in a microvascular-like network [53]. Ultimately, the idea is to spatially guide these endothelial sprouts with the aforementioned light-based hydrogel modification techniques. Photografting is a universal approach to altering the chemical properties of hydrogels in a 3D-manner and refers to the introduction of a molecule into the polymer backbone. The selection of a cytocompatible, water-soluble grafting agent allowed us to apply this process to cell-laden hydrogels. To enable photocleaving, the hydrogel needs to be crosslinked with a molecule that contains a photolabile moiety which can be cleaved upon light-irradiation. Both methods can be used to adapt the microenvironment of cell-laden hydrogels.

2 Theoretical Background

2.1 Extracellular matrix

The extracellular matrix (ECM) is a structurally stable network, composed of different interconnected proteins, most notably collagen, elastin and various microfibrillar proteins, adhesive glycoproteins, matricellular proteins and proteoglycans [54]. Besides its static role in contributing to the mechanical properties of the tissue and providing structural support to the cells, the ECM is a highly dynamic system, which is exposed to a continuous remodeling process and influences various cell functions and behaviors, such as proliferation, adhesion, migration, polarity, differentiation and apoptosis [55]. The interaction between matrix and cells is of reciprocal nature, within which the cells are producing, assembling and modifying the ECM, consequently influencing cell functions and behaviors and providing the cells with information regarding their spatial and temporal status [54]. Although the fundamental building blocks, proteins, polysaccharides and water, are ubiquitous, the composition and structure of the ECM is heterogeneous and tissue specific. Thereby, the biochemical, biophysical, protective and organizational properties of the matrix can vary [56]. The ECM can influence cell behavior via its biochemical and biophysical properties. Through various surface receptors, such as integrins, discoidin domain receptors (DDRs) or cell surface proteoglycans (PGs), the cells are able to interact with the appropriate cues, which will be further discussed in Section 2.2.1 [57]. In short, the chemical cues are provided, amongst others, by adhesive proteins, growth factors, cytokines and chemokines. Physical and mechanical properties include the stiffness, density, solubility and porosity. The mechanical properties are sensed by integrins, which are connecting the ECM with the actin cytoskeleton of the cell [58].

2.2 Three-dimensional cell culture systems

The term cell culture refers to the controlled cultivation of cells outside of a living organism at a specific temperature, pH, nutrient and waste level [59]. With the development of *in vitro* cell cultures, a new method besides the *in vivo* animal models, to be used for differentiation studies, drug discovery and pharmacological applications, cancer research, gene and protein expressions studies and for studying cell biology/ physiology, has been

established [3]. In a conventional 2D cell culture system cells are either cultured on a substrate or suspended in a cell culture medium. This method possesses significant shortcomings in terms of the tissue-specific architecture, biochemical and biophysical cues and cell–to-cell communication [2].

In contrast, 3D cell cultures are providing an environment which allows cell-to-cell and cell-to-matrix interactions by assuming the role of the ECM, consequently reducing the difference between the physiological environment and traditional cell culture systems [2]. Besides providing a heterogeneous platform in which cells are behaving more similarly to the natural conditions, which subsequently improves the transferability of *in vitro* research in areas such as drug development, to the actual *in vivo* effect, advances in techniques to locally modify the cell-laden matrix allow for the adaption of the individual cells' microenvironments [3], [4].

There are various 3D cell culture systems, each with their individual advantages and disadvantages. A rough classification can be made between scaffold-based and scaffold-free systems. Scaffold-free systems rely on the tendency of cells to aggregate under the right conditions [60], allowing for the creation of microtissue in various shapes. The most common shape is ellipsoidal and such systems are referred to as spheroids [61]. Compared to 2D monolayer cultures, spheroids have been reported to enable cell-to-cell and cell-to-matrix interactions and thereby provide a physical and chemical environment that is more similar to the actual *in vivo* condition. On the basis of mesenchymal stem/ stromal cells (MSCs), it has been demonstrated that an agglomeration into spheroids helps to maintain their intrinsic phenotypic properties, promotes the stemness marker expression and the secretion of cytokines, chemokines and angiogenic factors and improves cell viability. However, due to the inherent diffusion gradient, the core can be exposed to a lack of nutrients and oxygen, dependent on the spheroids' size [62].

Scaffold-based systems are utilizing biomaterials with different properties to provide the cells with a structure that is mimicking the functions of the ECM. In the most basic version, cells are encapsulated in or seeded on top of a biomaterial, consisting of naturally-derived or synthetic polymers, that can be synthetically modified to enable a fine-tuning of the chemical and physical properties. Prefabricated scaffolds possess a distinct architecture, facilitated by different fabrication methods, such as 3D printing or stereolithography [60], [63]. Nanofibrous, microporous and hydrogel polymers have been used as scaffolds for cell encapsulation experiments [64]–[68]. Compared to hydrogels, both nanofibrous and microporous scaffolds are limited in their ability to mimic the ECM [69].

Hydrogels are crosslinked hydrophilic polymer chains with a high swelling ratio and permeability. The mechanical characteristics of hydrogels are similar to soft tissue and they are permeable to oxygen, nutrients and other soluble metabolites, making them a suitable material for scaffold-based 3D cell culture systems [1]. An alternative approach is the use of decellularized tissue as a 3D cell culture system [70]. Scaffold-based models hold a clear advantage over 2D monolayer cultures in various aspects, such as the cell morphology, cell viability, differentiation capacities, gene and protein expressions or cellular interactions. Disadvantages can arise in terms of sample handling and high-throughput screening [71].

2.2.1 Microenvironment and durotaxis

All cells reside within their respective microenvironment, which can be defined by the following four key constituents: the surrounding ECM, the neighboring cells, soluble factors and the biophysical fields, according to a classification by Huang et al. [5], whose extensive work on functional and biomimetic materials acts as the template for the following section.

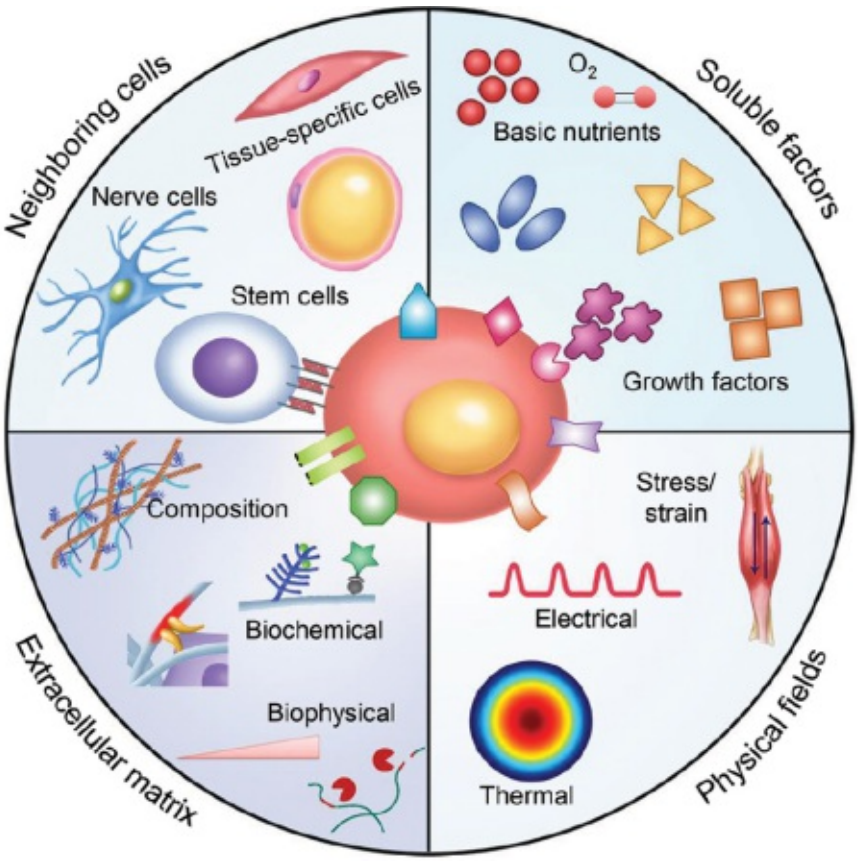

Figure 2.1. Illustration of the four key constituents and their subsequent components of the cell microenvironment. Reproduced from [5].

The comprehensive classification with the corresponding components is displayed in Fig. 2.1 and elaborated in the following paragraph. Besides the composition, which has been briefly touched on in Section 2.1, the ECM interacts with the cells via biochemical cues, namely cell adhesion ligands, stored and sequestered soluble signaling molecules and different chemical functional groups, and via biophysical cues, namely structural features, mechanical stiffness and degradability. Cells are communicating and interacting with each other either direct, through cell-to-cell contact, or indirect, through soluble factors. Direct interactions are tightly regulated by various signaling pathways and are facilitated by physical junctions, classified as tight junctions, anchoring junctions and gap junctions. Tight junctions, as the closest cell-to-cell contacts, are holding cells together and enable the formation of layers that act as barriers to substances and as separators between tissue. Anchoring junctions are mediating the cell-to-cell and cell-to-ECM adhesion. Gap junctions are responsible for coupling the metabolic activities of adjacent cells and synchronizing contractible cells. As mentioned before, cell-to-cell interaction occurs partly via soluble signal molecules, such as growth factors, cytokines and hormones. With oxygen, glucose and amino acids, various basic nutrients are also influencing cell behavior. Physical fields is the subgroup that refers to different physical stimuli, including strain and stress, which in case of blood vessels arises from the blood flow that exerts shear forces on the vessel walls, electrical, magnetic, acoustic and thermal fields.

In an effort to create biomimetic materials that are mimicking the respective *in vivo* ECM and the individual microenvironments, and to construct synthetic microenvironents for fundamental studies of cell functions and behaviors, various biochemical parameters, namely cell adhesion ligands, immobilized soluble factors and chemical functional groups, as well as biophysical parameters, such as structural and mechanical properties, degradability and electrical conductivity, have been adapted. An overview of the different parameters is provided in Fig. 2.2.

In accordance with the nature of the present study, the focus of the following paragraph lies on the material stiffness, a major component of the mechanical properties in terms of cell influence. Cells are sensing mechanical cues and translating them into intracellular signals, called mechanotransduction, which is facilitated by the adhesion of the cells to the substrate. The matrix stiffness has been reported to influence cell behavior and functions, most notably, proliferation [7], migration [6], differentiation [9] and gene and protein expression [10]. Directional cell migration can be induced by gradients of soluble factors, cell-adhesion ligands and as aforementioned material stiffness, which is then referred to as chemotaxis, haptotaxis and durotaxis, respectively [72]. Durotaxis has been observed

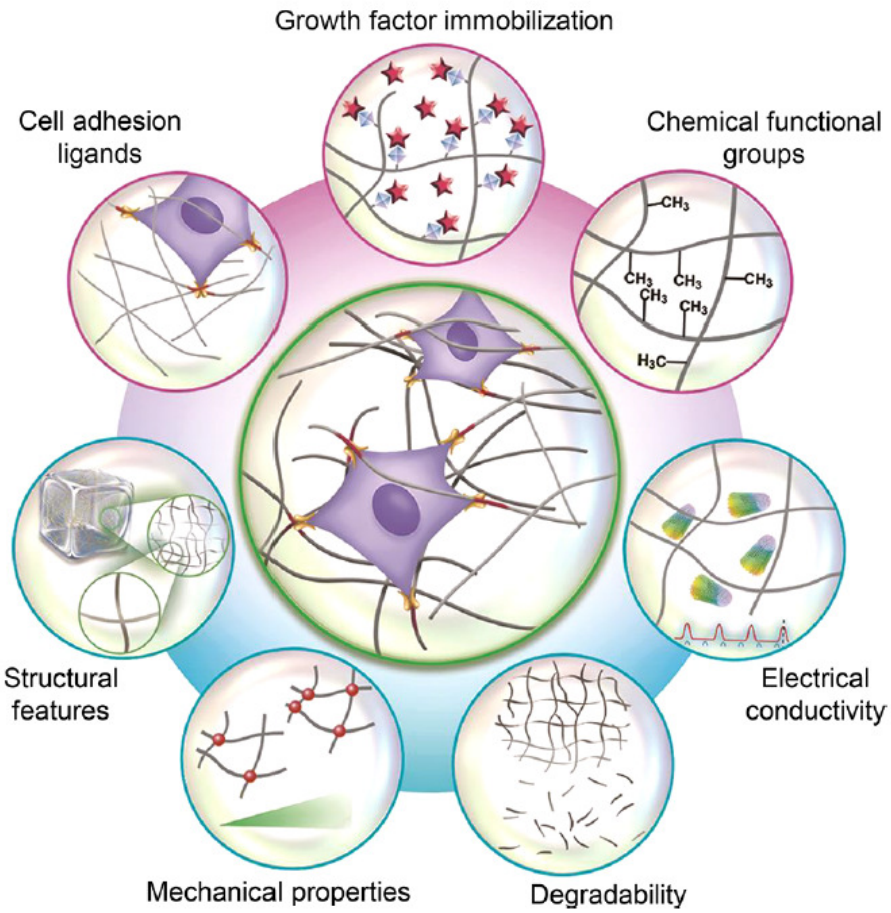

Figure 2.2. Illustration of the parameters that can be adapted in an effort to create ECM-mimicking biomaterials. The parameters can be grouped into two classes, biochemical (cell adhesion ligands, soluble factor immobilization, and chemical functional groups) and biophysical (structural features, mechanical properties, degradability, and electrical conductivity) parameters. Reproduced from [5].

in vivo, in processes such as wound healing, embryonic development and pathogenesis [73].

Various studies have demonstrated the potential of stiffness gradients for guiding cell migration *in vitro*. Different approaches, such as an inhomogeneous crosslinker and/ or material distribution [74], [75], photolithography [76] and the adaption of oligomer chain length [77], have been utilized for the creation of stiffness gradients. Furthermore, by adapting the hydrogel thickness a cell-perceived stiffness gradient can be created [78]. A variety of studies have employed such methods to create a substrate with an inherent stiffness gradient, on which cells have been seeded to subsequently observe their migration. Various cell types, such as fibroblasts [74], [79], [77], [16], MSCs [80], [78], [81], [82], [18], ASCs [17] and HUVECs [83], have been used to this end. It is stated in a number of publications that not only the steepness of the gradient itself but also the overall substrate

stiffness (minimum and maximum value) has an effect on cell migration [79], [76], [82]. Raab et al. [81] aimed to establish a 3D environment, with MSCs seeded on a Polyacrylamide (PA) hydrogel onto which a further layer of collagen had been deposited, and observed that the cells migrate in the gradient direction (min.: 1 kPa, max.: 34 kPa, gradient: 16.5 kPa/mm). In [83], coculture spheroids of HUVECs and human umbilical arterial smooth muscles cells (HUASMCs), that have been encapsulated in a PEG-based hydrogel with a stiffness gradient of 80 Pa/mm, showed a directionality in the outgrowing vascular sprouts. The number of sprouts was highest in the opposite gradient direction (by roughly 2 times), but also higher in gradient direction (by roughly 1.5 times) compared to perpendicular directions. Cells in the low elastic modulus region (0.7 kPa) showed the highest invasion area and longest sprout length over 7 days, followed by the intermediate elastic modulus region (1 kPa) and the high elastic modulus region (1.3 kPa). In accordance with these findings, the study by Cross et al. [15] also shows that the migration speed of HUVECs into a collagen hydrogel decreases with an increase in collagen concentration from 0.3% to 2%, which translates to an increase in stiffness from 0.03 kPa to 1.8 kPa. The study by Hosseini et al. [14] came to similar results. Duan et al. [13] seeded either ECs or MSCs on top of hyaluronic acid-based hydrogels with two storage moduli of 15.77 kPa and 4.8 kPa, and observed that the ECs migrated deeper into the softer hydrogel (by roughly 1.5 times) and MSCs into the stiffer hydrogel (by roughly 1.4 times). It has further been shown that cells preferably align on patterned regions with higher stiffness, which basically represents a very steep gradient [84], [85], [18].

2.3 Blood vessels

The vasculature, as a part of the cardiovascular system, is responsible for carrying blood and plasma all over the body, substances which are relevant for transporting molecules, such as oxygen, carbon dioxide, nutrients, waste and hormones, the regulation of the temperature, pH and osmotic pressure and the immune process, protecting against foreign molecules and disease, as well as for clotting to prevent excessive loss of blood [38].

In order to reach all requisite cells, a dynamic and hierarchical network of vessels, that starts with arteries, branching into arterioles and subsequently into billions of tiny capillaries, which act as a diffusion and filtration system, ultimately regrouping into veins through venules, with changing vessel diameters from over 1 cm down to a couple of µm, spans across the body [86].

Two main cell types, ECs and mural cells, which are, depending on the type of vessel,

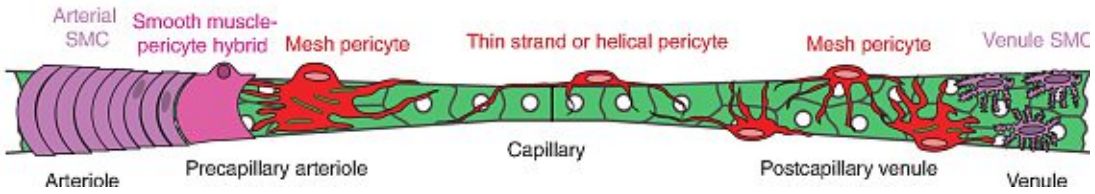

Figure 2.3. Illustration of the mural cell types and their distribution along the cerebral vasculature. Adapted from [87].

either smooth muscle cells (SMCs), regulating peripheral vascular resistance, vascular diameter and the direction of blood flow, or pericytes, and are surrounded by ECM, are present in blood vessels [88]–[90]. In general, blood vessels consist of three concentric layers, the tunica intima, tunica media and tunica adventitia, seperated by the inner and outer limiting membranes (membrane limitans interna and externa). The innermost layer is the tunica intima, which consists of a monolayer of ECs, followed by the tunica media, usually the thickest layer, which houses the mural cells, completed by the tunica adventitia, linking the vessel to the surrounding connective tissue. Depending on the vessel types, this generic architecture varies according to the individual tasks [91]. The composition of the vessel ECM is not discussed here, but interested readers can find extensive information in the works of Eble and Niland [91] and Fung [92].

Arterioles, capillaries and venules are the constituents of what is called the microcirculation [38]. With decreasing vessel diameter the number of SMC layers decreases and they are ultimately superseded by perictyes [93]. Pericytes are most abundant on small arterioles and venules and comparably scarce on capillaries. They are associated with vessel stabilization, hemodynamic processes, transendothelial transport, sensing angiogenic stimuli, guiding sprouts and eliciting endothelial survival functions [94]. The continuous shift of the mural cell type and their respective arrangement is visualized in Fig.2.3. Heterogeneity in vessel morphology regarding the type and arrangement of cells is not limited to mural cells, with ECs forming a continuous monolayer in arteries and veins, in contrast to capillaries where the ECs can be continuous, fenestrated or discontinuous [95].

2.3.1 Natural formation of blood vessels

The formation of blood vessels occurs in various physiological and pathological processes, namely during embryonic development, wound healing, collateral formation, tumor growth and various other disorders, such as ocular neovascularization [19]. It is a highly complex process, that is reliant on the correct cross-talk between various signaling systems. Deviations from this process can lead to an unorganized and immature vascular network, as

observed during tumor angiogenesis [96], [97]. A comprehensive, in-depth understanding of the mechanisms behind the formation of blood vessels is needed to facilitate the development of a stable and functional engineered vasculature.

A distinction can be made between the *de novo* formation of blood vessels based on the differentiation of hemangioblasts, a process that is called vasculogenesis and is most relevant during embryonic development, and angiogenesis, the formation of blood vessels from existing vessels. The general mechanisms are illustrated in Fig. 2.4, and in the following, the differences and similarities between the two mechanisms will be presented in detail, with a distinct focus on the individual steps within the respective processes. Due to the nature of the conducted experiments in the present work, angiogenic vessel formation is emphasized.

Vasculogenesis

The first functional organ that develops in the embryo of vertebrates is the cariovascular system in a process called vasculogenesis. The first step is the formation of the mesoderm, the middle layer of the three germ layers, from the epiblast by differentiation of epiblast cells into mesodermal cells during gastrulation. Hemangioblasts, a type of mesodermal cells, are giving rise to blood islands, the earliest discernible vascular structure, in the extra-embryonic yolk sac. They are proliferating and differentiating into angioblasts, precursors of ECs located at the outer layer, and hematopoietic stem cells (HSCs), located at the center of the blood islands [100], [101]. By fusion of the blood islands and ECs differentiation, the primary capillary plexus is formed, which differentiates into an arteriovenous vascular system upon the onset of blood flow [102]. The *in-situ* development of blood vessels also takes place inside the embryo, and the intra- and extra-embryonic primordia fuse at the 2-somite stage [101], [103], [104].

It has long been believed that vasculogenesis is a process only occuring during embryonic development, however, recent studies suggest that endothelial progenitor cells (EPCs) play a role in the neovascularization of ischmic or malign tissue, a phenomena that is referred to as postnatal vasculogenesis [105]–[107].

Although, compared to angiogenesis, the molecular signaling during vasculogenesis is poorly understood, several relevant bioactive molecules, which are fibroblast growth factors (FGFs), the hedgehog family of morphogens, vascular endothelial growth factors (VEGFs) and the transformation growth factor-β, have been identified [108].

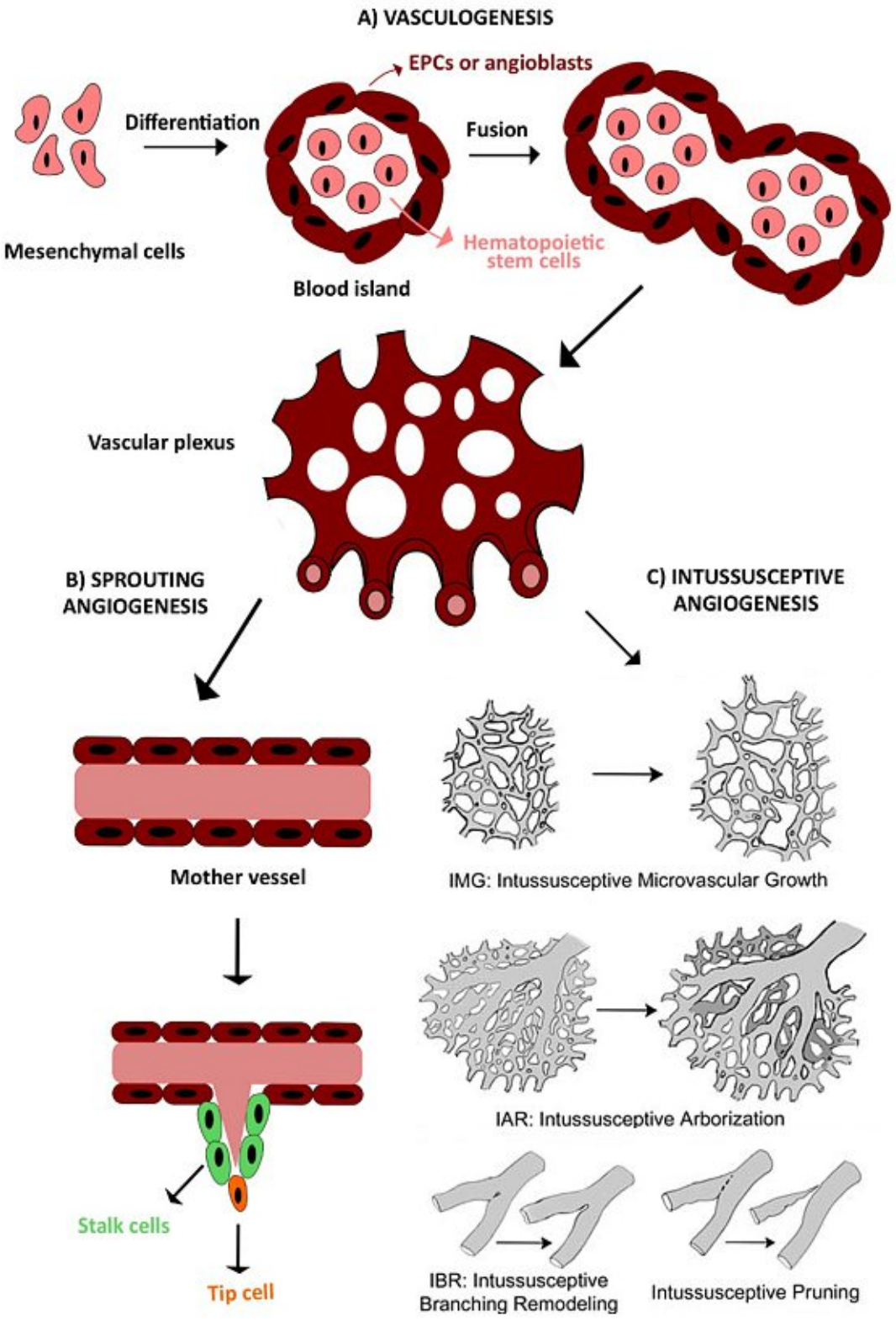

Figure 2.4. Illustration of the different mechanisms behind the formation of blood vessels. A general overview of vasculogenesis and angiogenesis, with a further differentiation into sprouting and intussusceptive angiogensis, is given. Adapted from [98], [99]

Angiogenesis

Angiogenesis refers to the formation of blood vessels from pre-existing vessels. The works of Folkman [109], [110], in which he observed a reciprocal effect between tumor formation and ECs, laid the foundation for a thorough understanding of angiogenesis. The process can be classified according to two different mechanisms (see Fig. 2.4). The first one being sprouting angiogenesis, where cells migrate to form a new vessel, and the second one being intussuseptive angiogenesis, which relies on remodeling of the vessel [111]. In the following, the two mechanisms will be thoroughly examined.

Sprouting angiogenesis is a multi-step process with the distinct phases of 1) degradation of the basement membrane, 2) migration of the ECs into the connective tissue, 3) formation of a lumen and subsequent perfusion, 4) formation of a network, 5) remodeling and pruning and 6) stabilization and maturation of the vessel [112], [100], [113]. The following in-depth description of the aforementioned individual phases is, if not further specified, based on the extensive review by Kolte et al. [112]. Upon the exposure to pro-angiogenic factors, mostly triggered by hypoxia, previously quiescent ECs are activated and start the angiogenic process [114]. Preceeding the degradation of the basement membrane, which is mediated by several proteinases, such as matrix metalloproteinases (MMPs), plasminogen activators, heparanases, chymases, tryptases and cathepsins, is the detachment of the mural cells. The degradation of the matrix does not only remove the physical barrier but also releases matrix-bound growth or anti-angiogenic factors, thereby mediating the angiogenic sprouting. This is followed by a collective migration of ECs in the form of a sprout, with a tip cell in the front and highly proliferative stalk cells behind. Only one cell can take the leading role, which is regulated by a feedback-loop based on VEGF signaling and the Notch/Dll4 system [115]. Different mechanisms have been observed in the formation of a lumen, namely, cell hollowing, which depends on the fusion of larger intracellular vesicles, and cord hollowing, enabled by the rearrangement of the position and morphology of cells [116], [117]. In order to form a network, the filopodia of neighboring tip cells interact with each other to initiate VE-cadherin containing junctions, leading to an anastomosis of the sprouts. This temporary homogeneous network is shaped into its final distinct form, in terms of vessel size, morphology and vascular density, by means of vascular remodeling and pruning. It further matures and specializes into its organ and tissue specific form, in terms of arterious-venous determination, formation of homotypic and heterotypic junctions, differentiation of ECs and the patterning of vessel specific cells lining the EC layer [118]. The recruitment of mural cells and the deposition of an ECM stabilizes the vessel and the ECs turn into quiescent non-proliferating phalanx cells [21].

Various signaling molecules and the subsequent receptors mediating the sprouting angiogenesis have been discussed by Patel-Hett and D'Amore [108]. Beyond the most noteworthy VEGF family of proteins and their corresponding receptors, notch signaling, which acts as a negative feedback mechanism to regulate VEGF signaling, semaphorins, netrins, the slit-robo signaling complex and the sprouty proteins are regulating the process. PDGFs, angiopoietins and the Tie receptors are of importance for vessel stabilization.

Intussusceptive microvascular growth (IMG) has been first described by Caduff et al. [119], who observed the insertion of numerous transcapillary pillars during the transformation of the capillary network in postnatal lungs of rats, seemingly resulting in a more complex network with a larger vascular surface area without sprouting of the individual capillary segments, which they termed in-itself or intussusceptive growth. They have identified four distinct phases, 1) beginning with the establishment of a contact between opposing vessel walls, 2) the reorganization of junctions between the ECs and subsequent perforation of fused endothelial leaflets, 3) the formation of the interstital core, stabilized by connective tissue, and lastly 4) the growth and maturation leading to a capillary mesh [120]. IMG has been furthermore demonstrated in the capillary plexuses, small arteries and veins in the myocardium, the skeletal muscle, the kidney and the retina [121]. Although the mechanism is not fully understood, both shear stress and the blood flow rate are believed to be major factors of influence in this process [121]. With the observation of the formation of feeding vessels from capillaries, termed intussusceptive aborization, and the remodeling of vascular bifurcation junctions, termed intussusceptive branching remodelling (IBR), further mechanisms based on the formation of transcapillary pillars have been identified, creating the need for the general term of intussusceptive angiogenesis (IA), as a mechanism of blood vessel formation that occurs without sprouting by internal division of the vasculature [122], [123].

2.4 Tissue engineering

Tissue engineering (TE) is a multidisciplinary field, positioned at the interface between engineering, the life sciences, chemistry and physics, with the aim to repair, maintain, reconstruct or improve specific tissues or organs [124], [125]. It is to be classified within the broader field of regenerative medicine [126]. The materials, the cells and the tissue architecture are the major components that can be adapted and harmonized to satisfy the requirements of the respective application [127]. The in Section 2.2 discussed approaches

to culturing cells in the corresponding materials also apply to TE, with the addition of approaches that do not rely on cell-seeding prior to implantation [128]. Cells that are being used for implantation can be either harvested from the patients themselves, from a donor within the same species or from a different species, which are referred to as autologous, allogeineic and xenogeineic cells, respectively [129].

In recent years, various TE applications have been successfully demonstrated, some of which are showing a clinical potential and others that have already been approved by the Food and Drug Administration (FDA) and/ or the European Medicines Agency (EMA) [130], [131]. Zhou et al. [132] have implanted an ear-shaped cartilage, fabricated by seeding of autologous chondrocytes in a compound scaffold. They reported cartilage formation in four out of five cases six months after implantation. By seeding autologous urothelial and muscle cells in a bladder-shaped scaffold and implanting it after seven weeks of culture, Atala et al. [133] were able to demonstrate improved urodynamics and an adequate structural architecture and phenotype. In a clinical trial, Grafix (Osiris Therapeutics), a cryopreserved human placental tissue, was compared to standard woundcare in the healing of diabetic foot ulcers (DFUs) and a significantly improved wound healing and reduced complications were reported [134]. Clinical follow-ups of matrix-associated autologous chondrocyte implantation (MACI) (i.e. the implantation of a chondrocyte seeded collagen matrix) after 5 and 15 years indicated that MACI is a suitable treatment of local cartilage defects in the knee [135], [136].

Despite the success in engineering various tissue types, such as bladder, blood vessels, skin, trachea, cartilage, bone and cardiac tissue, for which applications are either close to or already clinically available, and major advances in biomaterials, biofabrication techniques, mechanobiology, immunomodulation, the discovery and advancement of methods to create induced pluripotent stem cells (iPSCs) and improved spatial and temporal control of bioactive molecule presentation, there are still some considerable hurdles to be overcome to fabricate complex tissues of clinically relevant size, specifically complex organs such as the liver, lung, kidney and heart [127], [137]–[141]. Major challenges are the availability of sufficient amounts of immunological compatible cells, adequate biomaterials in terms of chemical, mechanical and biological properties and a sufficient vascularization of the engineered tissue [140]. In a review on the advances in TE, Langer and Vacanti [142] have identified the unreliability of maintaining a healthy and functional cell mass after implantation as the key obstacle in their effort to fabricate a human liver [143]. The next section is therefore focused on vascular tissue engineering, discussing recent achievements and challenges.

2.4.1 Vascular tissue engineering

A functioning blood vessel network is necessary to maintain homeostasis and facilitate the exchange of oxygen, nutrients, biochemicals and waste. Moreover, it seems that it also acts as a structural template and thereby influences the organization of tissue [22], [21]. The diffusion range of oxygen (100-200 µm, see Fig. 2.5) is the limiting factor to the size of engineered tissue [24], [23]. Although the host vasculature will generally grow into the tissue and form a network, this process can be very slow, subjecting parts of the tissue to oxygen and nutrient deficiency for a size-dependent time period [25, 26, 144].

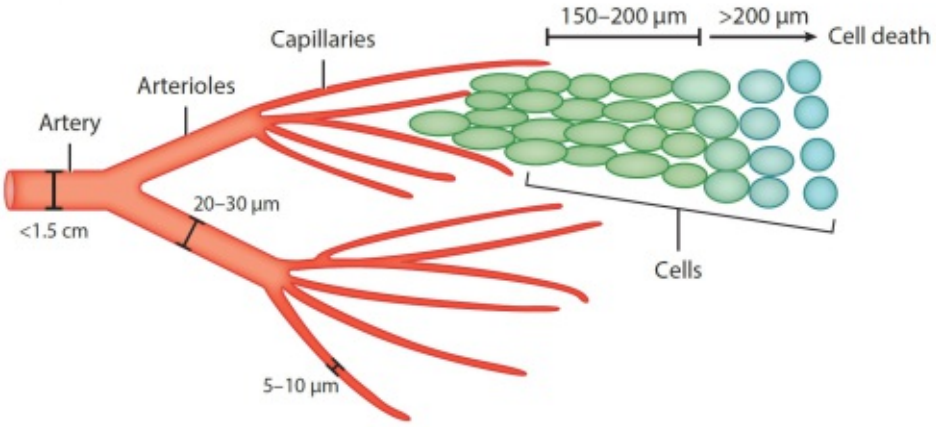

Figure 2.5. Illustration of the hierarchical structure of the vascular tree, indicating the required presence of capillaries for the survival of cells. Adapted from [145].

Therefore, the research field of vascular tissue engineering (VTE), originally defined by Couet et al. [146] as "[...] the development of a vascular construction that demonstrates biological and mechanical properties as close as possible to those of a native vessel", is concerned with the creation of functional blood vessels for either 1) the engineering of *in vitro* vascularized tissue or 2) the implantation of a tissue engineered vascular graft (TEVG) for the treatment of cardiovascular disease (CVD) [145]. Since the present work is concerned with the *in vivo* vascularization of engineered tissue, the following paragraphs will focus hereon.

An optimal engineered vascular network must meet the requirements of a well-distributed spatial organization, illustrated in Fig. 2.5, to ensure proper coverage of all cells, while minimizing the blood pressure, which is ensured by the hierarchical structure of the vascular tree, consisting of branching vessels with decreasing diameter, ultimately resulting in finely dispersed vessels that can get as small as 5 µm, called capillaries. It must be selectively permeable for the adequate delivery and removal of molecules and it should be

easily connectable to the patients' vasculature [147], [28]. There are different parameters that can be adjusted in the creation of a vascular network, namely, the matrix, the cells, the fabrication technique and the biochemical and biophysical cues [28]. Various cell types are used in the context of VTE. Table 2.1 gives an overview of the different human EC types and endothelial progenitor cells (EPGs) with the respective number of publications, indicating that at a share of more than 60%, HUVECs are the most commonly used ECs. Other widely used cells, either as a supporting cell line or for their potential to differentiate into ECs, are smooth muscle cells (SMCs), adult stem cells, most notably MSCs and ASCs, and pluripotent stem cells (PSCs) [148]–[150]. HUVECs are widely used because they are easy to obtain and to handle. Moreover, they have also been reported to form a functional monolayer within 11 days, compared to 28 days for arterial ECs, and the large number of published studies provides a good level of comparability. There are, however, downsides to this cell type, in that the origin in the umbilical vein limits potential *in vivo* applications to allografts, and that due to the site-specific phenotype it is most likely not the best fitting cell type for all applications [150], [148].

Vessel Type	EC Type	Abbreviaton	No. of PUBs
Marcrovascular EC	Human aortic EC	HAEC	25
	Human coronary arter EC	HCAEC	10
	Human pulmonary artery EC	HPAEC	5
	Human umbilical vein EC	HUVEC	540
Microvascular EC	Human dermal microvasculature EC	HDMEC	18
	Human pulmonary microvasculature EC	HPMEC	9
	Human brain microvasculature EC	HBMEC	7
Circulating EC	Endothelial progenitor cell	EPC	175
	Endothelial colony forming cell/ outgrowth EC	ECFC/ OEC	37
EC lines	HMEC-1		18
	Ea.Hy926		16

Table 2.1. Overview of the different endothelial cell types that are being used in the context of VTE. Their respective origin and the number of publications as of 2017 are listed. Adpated from [150].

As described in Section 2.3, other cell types, besides ECs, are present in blood vessels. While, generally, ECs have been shown to form tube-like structures on their own, a

supporting cell type is necessary for the formation of a perfusable, functional and stable vessel, whereby they can be from the same or from a different cell source [151]. Besides being indispensable due to their contribution to functional vessels, coculture systems of ECs and supporting cells can also recreate intercellular signaling and are thereby better mimicking the *in vivo* conditions [151]. By implanting 3D constructs in mice, seeded with either HUVECs monoculture or HUVECs and 10T1/2 mesenchymal precursor cells, and studying the vessel formation over a period of 56 days, Koike et al. [152] have shown that the total length of perfused vessel structure per unit area is overall significantly higher for the coculture implant, and, as opposed to the monoculture implant, there is no vessel decline in long term culture, indicating an improved long-term stability. A study by Pati et al. [153] found that a coculture of HUVECs and MSCs reduces permeability of the cell layer, linked to a higher expression of VE-cadherin and β-catenin. Melero-Martin et al. [154] implanted a matrigel plug, seeded with different ratios of EPCs and MSCs and studied the vessel density after 7 days, revealing a bell-shaped curve which indicates the interdependence of the cell types in the vessel formation process. A variety of publications indicate the suitability of ASCs as a supporting cell type. Verseijden et al. [155] encapsulated HUVEC and ASC spheroids, either as mono- or cocultures, in fibrin and studied network formation and protein expression over the course of 14 days. They observed that sprouting from HUVEC monoculture spheroids, compared to coculture and ASC monoculture spheroids, was low. ASCs formed a network and expressed α-smooth muscle actin, CD34, hepatocyte growth factor and inhibitor of MMP 1 and MMP 2. Furthermore, ASC conditioned medium induced HUVEC sprouting. A similar study, with OECs encapsulated in fibrin and ASCs either in microcarrier beads, in suspension, seeded on top or as conditioned media, came to the conclusion that ASCs are inducing vessel growth by secreting pro-angeogenic and regulatory proteins and stabilize the vessels by differentiating towards pericytes, and are therefore required for a stable vascular network formation [156]. Other studies came to similar conclusions, supporting the overall notion of suitability of coculture systems with ASCs as the supporting cell type for VTE [157]–[160].

2.5 Multi-photon lithography

2.5.1 Multi-photon absorption

Göppert-Mayer (1931) was the first to theoretically investigate two-photon absorption in her PhD thesis [161]. Subsequently, with the development of lasers, it became possible to provide the experimental validation [162]. Multi-photon absorption enables the initiation

of a chemical or physical reaction within a resolution of around 100 nm. This is possible due to the optical non-linearity, displayed on the left in Fig. 2.6, according to which the probability of multi-photon absorption shows a non-linear dependence on the laser intensity, and the chemical non-linearity (displayed on the right in Fig. 2.6), according to which a certain threshold must be reached to trigger a chemical reaction [163]. As illustrated on the right side of Fig. 2.6, a single photon in the ultraviolet (UV) spectrum might carry enough energy to transfer an atom or molecule from the ground state to an excite state, whereas in the near-infrared region two or more photons might carry the same amount of energy, and therefore the simultaneous absorption of an appropriate number of photons is necessary. To ensure a significant probability of the occurrence of multiple photons at the same place and time, the laser intensity must be sufficiently high, therefore, a pulsed laser is utilized to keep the average power comparably low [163].

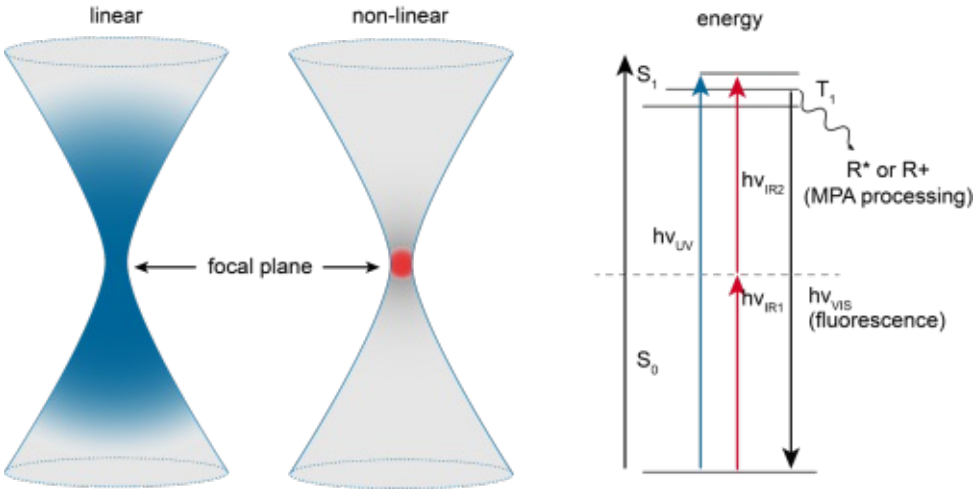

Figure 2.6. Illustration of the optical non-linearity and the difference between single- and two-photon absorption. Reproduced from [164].

2.5.2 Multi-photon lithography system

A schematic of the multi-photon lithography setup, that has been used within the scope of the present work, is shown in Fig. 2.7 and the individual components will be discussed in the following. The light source is a femtosecond Ti:Sapphire laser (MaiTai eHP DeepSe, Spectra-Physics) with a tunable wavelength between 690 nm and 1040 nm. The pulse width is 70 fs, the repetition rate 80 MHz and the average power 2.4 W. The linearly polarized beam is passing through a half-wave plate mounted on a motorized rotary stage, that rotates light polarization, followed by a beam splitter cube which transmits the p-polarized part of the light and reflects the s-polarized part into a beam dump, thereby regulating the maximum laser power in the system. After deflection of the beam in an acousto-optical modulator (AOM, AA Opto-Electronic) a pinhole ensures that only

the first order beam can pass through. This allows for the rapid modulation of the laser power during printing. To make sure that the beam is overfilling the rear aperture of the objective, it is expanded with a 5x achromatic beam expander. A galvanometer-scanner (Scanlab), followed by a scan lens, a tube lens, and a microscope objective, allows high speed scanning of the objective's field of view with the focused laser beam. Linear stages (Märzhäuser Wetzlar) are enabling a movement of the sample holder in xy-direction and the objective in the z-direction, thereby changing the relative position of the focal point to the sample. The sample can be observed during printing via a CMOS-camera located under the objective behind a semi-transparent mirror.

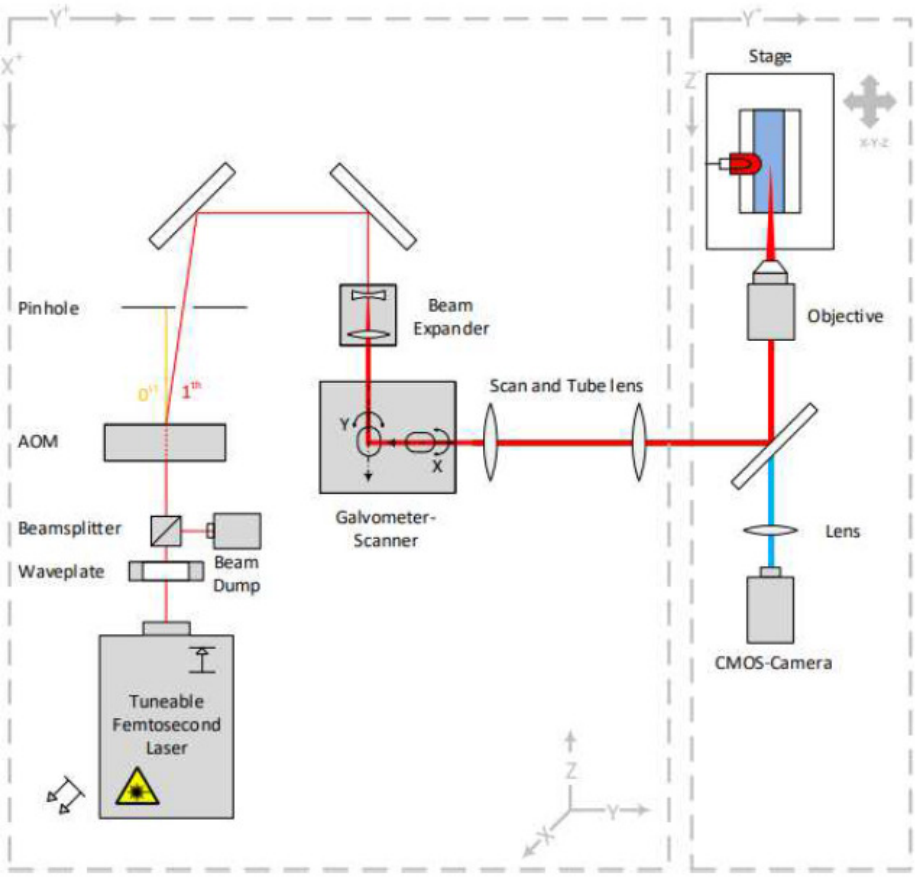

Figure 2.7. Schematic illustration of the multi-photon lithography setup that has been used in the present work. Reproduced from [164].

2.5.3 Multi-photon induced grafting

Molecular grafting refers to the immobilization of individual molecules on different materials and has been previously applied in electronics and biomedical engineering to alter the surface of substrates [165], [166]. In photografting, functional molecules are activated by light and subsequently immobilized on a polymer matrix [167]. To this end, different

moieties such as aryl azides, aryldiazirine or benzophenone which are activated to highly reactive nitrenes, carbenes and benzhydrol radicals, respectively, have been used [168]. Ovsianikov et al. [169] were the first group to utilize multi-photon lithography for the photolysis of the azide groups of BAC-M, a commercially available aryl azide, which allowed them to photograft in an arbitrary 3D-manner with a resolution down to 4 µm.

2.5.4 Multi-photon induced cleaving

Photodegradation, a process in which photolabile functional groups are cleaved upon light irradiation, allows for the creation of spatiotemporal tunable hydrogels, which are capable of a controlled release of biomolecules by photocleavage of photolabile groups on a photostable backbone [170], or which are capable of altering the crosslinking density by either forming the hydrogel from photodegradable crosslinking macromers [171] or by using a photodegradable crosslinker on a pre-formed polymer [172]. Two popular photocleavable linkers are based on o-nitrobenzyl (oNB) alcohol derivatives [173] and coumarin derivatives [174], [175]. Judkewitz et al. [176] have demonstrated the potential of multi-photon lithography as a method to initiate photocleavage at a very low scale and Wylie and Shoichet [177] created 3D-micropatterns of reactive amines in an agarose hydrogel modified with coumarin-caged amines upon multi-photon absorption. Since the multi-photon absorption cross section for oNB derivatives is rather low, subsequently requiring high laser intensities to induce photocleavage, several optimization strategies have been pursued, among which Lunzer et al. [172] have introduced a modular system, in which the addition of a small molecule sensitizer significantly decreases the photocleaving threshold.

3 Materials

3.1 Hydrogels

Hydrogels are composed of hydrophilic polymer chains, interconnected via crosslinks and therefore capable of taking up comparably large amounts of polar liquids while retaining their shape. The characteristics are similar to soft tissue and they are highly permeable to oxygen, nutrients and other water-soluble metabolites, making them an overall suitable material for scaffold-based 3D cell cultures [1]. Hydrogels can be of either synthetic or natural origin. Natural hydrogels can be further differentiated into protein- and polysaccharide-based polymers [178]. Among the various natural polymers, gelatin, which is derived from collagen by breaking the triple-helix structure into single-strands, is commonly used for tissue engineering applications [179]. Gelatin is highly biocompatible [178], it facilitates cell adhesion, it is bioactive [178], enzymatically degradable by metalloproteases and considered safe by the FDA, moreover, it is abundantly available [180]. The reversible sol-gel transition (gelation) occurs at the phase temperature of 30-35 °C through the formation of triple helices and hydrogen bonds [180]. Since the solubility at body temperature and the low mechanical properties [178] limits the *in vivo* applicability, different modifications approaches have been developed to stabilize the hydrogel via chemical crosslinking [180]. Two such modified gelatin hydrogels have been used in the present work, namely gelatin methacryloyl (gel-MA) and thiolated gelatin (gel-SH).

3.1.1 Gelatin methacryloyl

Gelatin methacryloyl, also referred to as methacrylated gelatin, gelatin methacrylate, methacrylamide modified gelatin or gelatin methacrylamide, is a photo-crosslinkable gelatin-based hydrogel that is synthesized by the direct reaction of gelatin with methacrylic anhydride (MA) in a phosphate buffer [181]. In this reaction, which is illustrated in Fig. 3.1i, the amine and hydroxyl groups of the amino acid residues are substituted by a majority of methacrylamide and a minority of methacrylate groups, respectively [181]. The degree of substitution (ds) can be varied by changing the amount of MA or the pH during the reaction [181]. Photopolymerization is facilitated by a water-soluble photoinitiator

which starts a free radical chain-growth polymerization of the reactive functionalities (methacrylamide and methacrylate) upon light irradiation, as illustrated in Fig. 3.1ii. This results in the formation of short synthetic oligomer/ polymer chains in between the gelatin polypeptide chains [180].

Gel-MA with a degree of substitution of 63% was synthesized [45] and provided by the Polymer Chemistry and Biomaterials Group at the Ghent University.

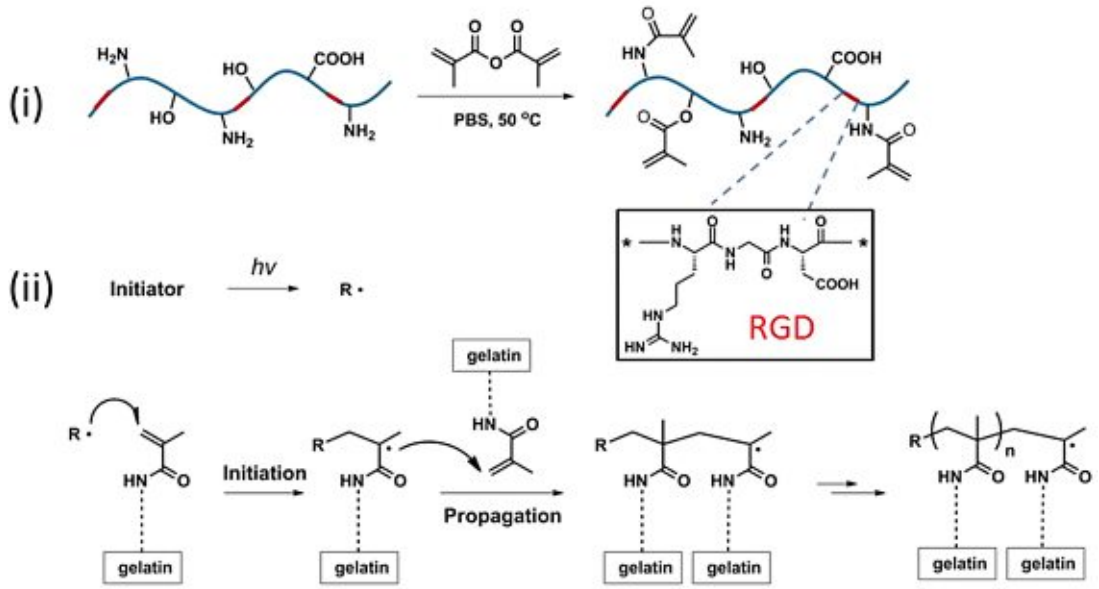

Figure 3.1. Illustration of i) the synthesis of gel-MA, with RGD domains highlighted in red and their chemical structure depicted, and ii) the photopolimerization process of methacrylamide functionalities. Adapted from [181].

3.1.2 Collagen type 1

Highly viscous, commercially available high concentration collagen type 1 (Corning) with a concentration range of 8-11 mg/mL, extracted from rat tails and supplied in 0.02 N acetic acid, was used for the formation of collagen hydrogel pellets. Collagen is an abundant structural protein that can be easily extracted with minimal contamination. The acid solubilized collagen turns into a structurally stable hydrogel at neutral pH, which causes the polymerization of collagen fibrils into fibers [182].

3.1.3 Thiolated gelatin

Thiolated gelatin is synthesized by functionalizing gelatin with thiol groups through the reaction of a thiolating agent with the amines of (hydroxy)lysine in the gelatin backbone [183]. The gel-SH can be crosslinked in a Michael-type thiol-ene addition, the

reaction between a thiol and an electron deficient, activated double bond, which is in the present work an acrylate [180]. It needs to be highlighted, that Michael-type thiol-ene additions are nucleophilic additions which are not reliant on photoinitiators or light irradiation. They take place without the formation of potentially cytotoxic side products at physiological pH [180].

Gel-SH with a degree of substitution of 56% was synthesized [183] and provided by the Polymer Chemistry and Biomaterials Group at the Ghent University.

3.2 Cell culture

Endothelial Cell Growth Medium-2 (EGM-2) was prepared by supplementing the Endothelial Cell Basal Medium-2 (EBM-2, Lonza) with the EGM-2 SingleQuots Supplements (Lonza), both from the EGM-2 Endothelial Cell Growth Medium-2 BulletKit (Lonza). All cell lines were cultivated in an incubator (BINDER) at 37 °C with 5% CO_2 in a humid atmosphere and split at around 80 percent confluency. The media were changed every 2 to 3 days.

3.2.1 Human adipose-derived stem cells

hTERT immortalized human adipose-derived mesenchymal stem cell line (hASCs/TERT1, Evercyte), in the following abbreviated as ASCs, were either used in their normal state or retrovirally infected with green fluorescent proteins (GFP-ASCs) according to the protocol by Knezevic et al. [184]. The fluorescent protein expression enables fluorescent imaging with a laser scanning microscope (LSM). ASCS/ GFP-ASCs were cultured in T-75 cell culture flasks (Greiner Bio-One) in EGM-2 supplemented with 10% fetal calf serum (FCS, Sigma-Aldrich).

3.2.2 Human umbilical vein endothelial cells

Human umbilical vein endothelial cells (HUVECs) transfected with lentiviral vectors expressing red fluorescent proteins (RFP-HUVECs, PELOBiotech), were cultured in EGM-2 supplemented with 5% FCS in T-25 cell culture flasks (Greiner Bio-One). The fluorescent protein expression enables fluorescent imaging with a LSM.

3.3 Li-TPO-L photoinitiator

The photoinitiator lithium (2,4,6-trimethylbenzoyl)phenylphosphinate (Li-TPO-L) was prepared according to a previously reported protocol [185]. Li-TPO-L was stored as a 6 mM stock solution in a light protecting glass vial and used in a working concentration of 0.6 mM, in accordance with the cell viability study by Markovic et al. [185].

Li-TPO-L was synthesized [185] and provided by the Polymer Chemistry and Technology Group at the TU Wien.

3.4 DSSA photografting agent

The commercially available, water soluble and hydrophilic molecule 4,4'-Diazido-2,2'-stilbenedisulfonic acid (DSSA, Sigma-Aldrich) was selected as the photografting agent. It contains two azide functional groups which can be activated to highly reactive nitrenes upon light irradiation, capable of binding to C-H and N-H bonds.

3.5 PEG-(oNB-A)$_2$ photocleavable crosslinker

Poly(ethylene) glycol-(o-nitrobenzyl acrylate) (PEG-(oNB-A)$_2$) is a photocleavable crosslinker. The chemical structure is displayed in Fig. 3.2i. The acrylate functional groups can react with thiols in a Michael-type thiol-ene addition, as shown in Fig. 3.2ii. Upon light irradiation (single- or multi-photon absorption) the photolabile o-nitrobenzyl ester functionalities are photocleaved, according to the depiction in Fig. 3.2iii.

PEG-(oNB-A)$_2$ was synthesized [172] and provided by the Polymer Chemistry and Technology Group at the TU Wien.

3.6 DAS multi-photon sensitizer

Tetrapotassium 4,4'-(1,2-ethenediyl)bis[2-(3-sulfophenyl) diazenesulfonate] (DAS/ AS7) has been used as multi-photon photosensitizer. It is a cytocompatible, water soluble, diazosulfonate-based molecule that absorbs light irradiation and, as used in the present work, transfers the energy to the oNB functionalities [186].

DAS was synthesized [186] and provided by the Polymer Chemistry and Technology Group at the TU Wien.

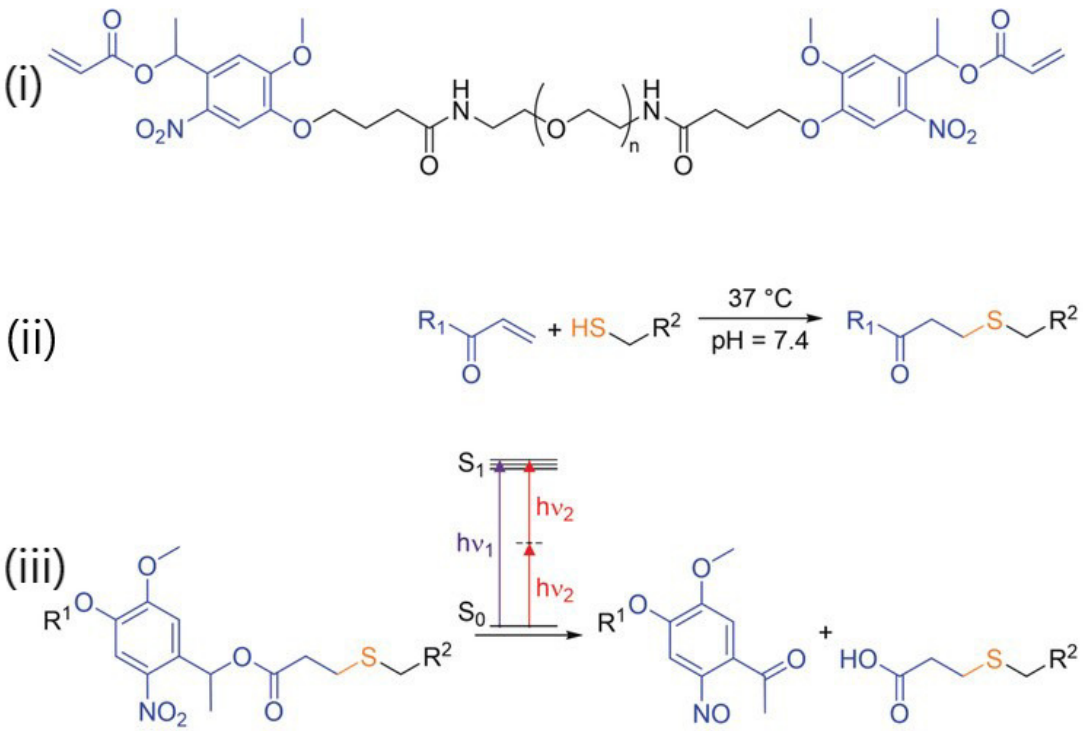

Figure 3.2. Illustration of i) the chemical structure of the (PEG-(oNB-A)$_2$) photocleavable crosslinker, ii) the Michael-type thiol-ene addition between the acrylate group and a thiol and iii) the photocleavage of the photolabile o-nitrobenzyl ester functionalities. Adapted from [172].

4 Methods

4.1 Spheroid formation

4.1.1 Methyl cellulose

For the preparation of methyl cellulose, 600 mg of methyl cellulose powder (Sigma-Aldrich) was weighted, transferred to a magnetic stirrer and autoclaved (Vapour-LineECO, VWR). 50 mL of EGM-2 medium was heated to 60 °C and added to the methylcellulose powder. The solution was then stirred for 20-30 minutes at room temperature and afterwards for 2 hours at 4 °C. The stirred methylcellulose solution was transferred to a falcon tube and centrifuged for 2 hours at 5 000 g and 4 °C. The clear, highly viscous supernatant was transferred to a new falcon tube and stored as methyl cellulose stock solution at 4 °C.

4.1.2 Casting of agarose molds

The spheroids were formed using MicroTissues 3D Petri Dish micro-molds (Sigma-Aldrich) casted with a 2% agarose solution. This solution was created by autoclaving 1 g agarose powder (Sigma-Aldrich) and dissolving it in 50 mL sterile water. The heated agarose solution was pipetted into the micro-mold and left for a couple of minutes to ensure physical gelation. The agarose molds were transferred to a 12-well plate and soaked in 3 mL PBS for 30 minutes for equilibration. Each agarose mold has 81 microwells.

4.1.3 Cell seeding

RFP-HUVECs and ASCs/ GFP-ASCs were detached from the cell-culture flask by washing them twice with PBS and then exposing them to Trypsin-EDTA 0.25% (Gibco) for 5 minutes. Medium was added after successful detachment for neutralization. The cells were counted and a solution containing 40 500 RFP-HUVECs and 40 500 ASCs/ GFP-ASCs was aliquoted. For ratios other than 1 to 1, a total of 81 000 cells was split accordingly to the desired ratio. After spinning the cells down in a benchtop centrifuge (Rotina 380 R, Hettich), the remaining solution was carefully removed and the cells were resuspended in 190 µL of medium containing 20% methyl cellulose. After carefully mixing the media, to ensure an even distribution of cells, it was pipetted into the agarose mold. The 12-well

plate was incubated for 1 hour, so that the cells could gather in the micro-cavities, before carefully adding 2 mL of 80% EGM-2 5% and 20% methyl cellulose stock solution. After 24 hours of incubation the spheroids were checked under a brightfield microscope, the methyl cellulose medium was removed, fresh medium was added and the spheroids were harvested.

4.2 Functionalization of microscopy dishes

The µ-dishes with glass bottom were methacrylated, to ensure a more durable attachment of the gel-MA hydrogel, according to the following procedure. In a first step the methacrylation solution was prepared by mixing 48 mL ethanol (Sigma-Aldrich), 0.3 mL acetic acid (Sigma-Aldrich) and 50 mL deionized water (Sigma-Aldrich) with a magnetic stirrer. After having slowly added 2 mL of 3-(Trimethoxysilyl)propyl methacrylate (Sigma-Aldrich) dropwise, the solution was stirred for 30 minutes and transferred to the plasma-cleaned µ-dishes with glass bottom (ibidi), covering the glass bottoms for 15 minutes. The methacrylation solution was disposed and the µ-dishes were washed with deionized water. To evaporate the remaining liquid, the µ-dishes were placed in an oven for 30 minutes at 110 °C.

4.3 Hydrogel preparation

Cells in suspension were seeded at a density of 1.2 million cells per mL. Spheroids, each containing a total of 81 000 cells, were encapsulated at a density of 81 spheroids per 100 µL. The actual number of spheroids encapsulated in the hydrogel pellet depends on the success rate of the transfer from mold to pellet.

4.3.1 Gelatin methacryloyl - photografting

Stock solutions with different concentrations were prepared by dissolving gel-MA in phosphate-buffered saline (PBS, Sigma-Aldrich) in a water bath at 37 °C. Depending on the desired gel-MA working concentration, a stock solution was mixed with the photoinitiator Li-TPO-L (working solution of 0.6 mM) and either PBS or cells/ spheroids suspended in EGM-2 5% at an appropriate ratio. The solution was mixed thoroughly to ensure an even distribution of cells/ spheroids. 30 µL of the solution was pipetted onto a methacrylated glass bottom dish and placed in the UV crosslinker (Boekel, 1 J, 365 nm). After crosslinking, 2 mL of 1 mM DSSA dissolved in EGM-2 5% was added. The pellets were incubated for 24 hours and thereafter, transferred to the multi-photon lithography setup to mod-

ify the chemical properties. Right after, the pellets were washed twice with medium to remove any residual DSSA.

4.3.2 Collagen type 1 - photografting

The collagen hydrogel pellets were prepared by slowly mixing the optically clear viscous collagen solution with PBS or cell/ spheroids containing EGM-2 in different ratios and 10% of 10 mM DSSA, dissolved in PBS, to achieve a working concentration of 1 mM. After letting the collagen gelate in the incubator for an hour, a 1 mM DSSA solution (either PBS or cell culture medium) was added and the samples were stored in the incubator for 24 hours. Finally, the samples were transferred to the multi-photon lithography setup to modify the chemical properties, and after grafting the samples were washed twice with medium to remove residual DSSA.

4.3.3 Thiolated gelatin - photocleaving

The first step in the preparation of a photocleavable, multi-photon sensitive gel-SH was the preparation of a 5% stock solution, by dissolving gel-SH in PBS in a water bath at 37 °C. This process takes up to 7 hours and can be shortened to 1-2 hours by periodical stirring with a vortex mixer. Besides the gel-SH stock solution, a 30% solution of the PEG-(oNB-A)$_2$ photocleavable crosslinker, which was prepared by dissolving the powder in PBS or in a cells/ spheroids containing cell culture medium, and the DAS multi-photon sensitizer, which was stored as a 40 mM stock solution, and can be prepared by dissolving 1 mg of DSA powder in 35,27 µL of PBS, is needed. To create 100 µL of hydrogel, 82 µL of gel-SH (working solution of 4.1%) was mixed with 6 µL of DAS (working solution of 2.4 mM), followed by 11.9 µL (working solution of 3.6%) of linker. The solution was mixed and pellets of 30 µL were rapidly pipetted onto a microscopy dish with a glass bottom before crosslinking could occur. The hydrogel pellets were stored in an incubator for 1 hour to ensure full crosslinking before cell culture medium was added. After 24 hours of incubation, the samples were transferred to the multi-photon lithography setup for cleaving.

4.4 Analytical biochemical assays

4.4.1 PrestoBlue cell viability assay

To test the cytocompatibility of the DSSA grafting agent, a PrestoBlue cell viability reagent (Thermo Fisher Scientific) was used. DSSA was dissolved at a concentration of 4

mM in EGM-2 5% and EGM-2 10% for RFP-HUVECs and ASCs, respectively and then diluted 1 to 1 to achieve concentrations of 2 mM and 1 mM. The cells were seeded in a 96-well plate at a density of 5 000 cells per well and incubated for 24 hours to let them attach to the surface. Afterwards the medium was exchanged for different concentrations of DSSA (4, 2 and 1 mM). One plate per cell type was placed in a UV crosslinker (Boekel) and irradiated with 1 J at a wavelength of 365 nm. After 24 hours of incubation with the DSSA grafting agent the PrestoBlue cell viability assay was performed. PrestoBlue was diluted 1 to 10 in the adequate medium and 100 µL per well was added. After 1 hour of incubation the fluorescent signal was measured with a plate reader (Synergy BioTek, excitation 560 nm, emission 590 nm). The values were corrected for the background fluorescent signal. Medium without diluted DSSA was used as a positive control and cells treated with 50% dimethyl sulfoxide (DMSO, Sigma-Aldrich) for 1 hour acted as the negative control. The effect of DSSA was compared to the positive control, which we assumed to have 100% metabolic activity.

The cytocompatability of DAS was tested similarly to DSSA. In brief, DAS was dissolved at a concentration of 2 mM in EGM-2 5% and diluted 1 to 1 to achieve concentrations of 1 mM and 0.5 mM. The cells were seeded in a 96-well plate at a density of 5 000 cells per well and incubated for 24 hours to let them attach to the surface. Afterwards the medium was exchanged for different concentrations of DAS (2, 1 and 0.5 mM). After a resting period of 24 hours in EGM-2 5%, 100 µL of PrestoBlue diluted 1 to 10 in EGM-2 5% was added. After 1 hour of incubation the fluorescent signal was measured with a plate reader. The values were corrected for the background fluorescent signal. The effect of DAS was compared to the positive control (EGM-2 5%), which we assumed to have 100% metabolic activity.

To identify the metabolic activity of encapsulated cells, a PrestoBlue cell viability assay was performed. PrestoBlue was diluted 1 to 10 in the adequate medium and 3 mL per sample was added. After 1 hour of incubation, 100 µL of solution per sample was transferred to a 96-well plate and the fluorescent signal was measured with a plate reader. The values were corrected for the background fluorescent signal.

4.4.2 Live/ dead staining

To identify the survival rate of encapsulated cells, a live/ dead staining was performed. Live cells were stained with calcein acetoxymethylester (calcein-AM), dead cells with propidium iodide (PI) and the nuclei of all cells with Hoechst. In short, a solution of

4 µL Calcein-AM, 8 µL PI and 5 µL Hoechst was prepared. EGM-2 was removed from the µ-dishes with glass bottom and the samples were washed once with warm PBS. The solution was added and the samples were incubated for an hour at 37 °C. After removing the staining solution and adding fresh medium the samples were imaged with a laser scanning microscope (LSM800, Carl-Zeiss).

4.4.3 Ki67 staining

To identify the proliferation rate of encapsulated cells, anti-Ki-67 staining was performed. The Ki-67 protein (also known as MKI67) is a cellular marker for proliferation The cells were fixed with 4% formaldehyde (1h), permeabilized with 0.1% Triton X-100 for 5 minutes and then blocked with 1% BSA in 0.1% PBS-Tween (1h). The cells were then stained with Anti-Ki67 antibody (Abcam, dilution 1:200) and Hoechst (dilution 1:1 000) and incubated overnight at +4 °C. After removing the staining solution and adding PBS the samples were imaged with the LSM.

The proliferation rate was quantified by normalizing the Ki-67 staining positive area to the Hoechst staining positive area, which were obtained by quantification of the respective fluorescent area using the ZEN Blue 2.6 software, according to the previously describe protocol [53]. Due to a sample size of one a statistical evaluation is not possible.

4.5 Printing procedure

Usually, except for time lapse experiments, each µ-dish with glass bottom contained 1 to 2 hydrogel pellets with 30 µL. For printing, these µ-dishes were transferred to the multi-photon lithography setup. With a maximum printing time of around 12 minutes per structure (1 to 2 structures per pellet) the time in which cells are taken from their ideal environment is well within a reasonable range according to our previous experimental observations.

CAD models for printing were sliced along the vertical direction and the slices were scanned with parallel lines. The horizontal and the vertical line spacings were, if not further specified, 0.5 µm and 1 µm, respectively. The vertical line spacing can be higher since the voxels are elongated in vertical direction. The orientation of the lines in either x- or y-direction was changed layer by layer, with an offset between the planes. Printing speed was between 500 mm/s and 1 500 mm/s and the printing power ranged from 20 mW to 300 mW. An Olympus 10x/ 0.4 NA objective was used. The printing direction

was from top to bottom in order to prevent the laser from passing through already photografted regions. A wavelength of 700 nm is most suitable for the applications of the present work and has therefore been used in the majority of experiments, however, due to laser performance issues at lower wavelengths it had to be increased to 725 nm for the later experiments. This is stated accordingly in the description of the respective images.

The power threshold, upon which a photochemical reaction is initiated, depends on the participating molecules. In general, the threshold scales with the inverse square root of the exposure time, for exposure times under 1 ms, which is directly dependent on the printing speed [187]. At this lower threshold, only a certain fraction of the possible number of chemical reactions are initiated. With an increase in power, at a given exposure time, this fraction increases until a upper threshold is reached, at which either all possible reactions have occurred or thermal effects lead to the destruction of the material. Therefore, threshold tests have been performed to identify suitable laser powers and printing speeds.

4.6 Image acquisition

A confocal laser scanning microscope was used to obtain the images. The DSSA was visualized by exciting at a wavelength of 410 nm, the GFP-hASCs were visualized by exciting at a wavelength of 488 nm and the RFP-HUVECs were visualized by exciting at a wavelength of 561 nm. The time-lapse imaging was performed under 37 °C and 5% CO2, in a humid environment. The migration distances were quantified using the ZEN Blue 2.6 software.

The fluorescent images of cell alignment were quantified using Fiji, which is an open-source image processing package based on ImageJ. Quantification was based on the fluorescent area to account for the potential overlapping of multiple cells. After thresholding the image, a watershed segmentation was performed. Ellipses were fitted to the particles and the angles between the primary axis and a horizontal line were analyzed. The area of particles within a deviation of 10 degrees from the horizontal and vertical line was counted as aligned.

4.7 Statistical analysis

The statistical analysis for the cytocompatibility tests was performed using the free Real Statistics Resource Pack software Release 7.2 [188]. After checking the prerequisites,

namely, a similar population variance, a normal distribution, independent samples and equal sample sizes, a one-way analysis of variance (ANOVA) was performed. If the null hypothesis was rejected ($p < 0.05$), there is a significant difference between the groups and a post-hoc Ryan, Einot, Gabriel, Welsh Studentized Range Q (REGWQ) test was performed to test if the difference between the groups is statistically significant. Results are presented as the mean value +/- the standard deviation (SD).

The statistical analysis for cell migration speed was performed using R (R Core Team 2017) with the lme4 package [189], to conduct a linear mixed effect analysis of the dependence of migration distance from laser power. We used time and laser power as fixed effects and observed sample as random effect. Visual inspection of the residuals did not reveal macroscopic deviations from normality and homoscedasticity. A likelihood ratio test of the full model against the same model without the effect of laser power was performed to obtain the p-value. Rejecting the null hypothesis ($p < 0.05$), indicates that laser power has a non-negligible influence on migration distance in time, therefore on migration speed.

5 Results and Discussion

5.1 Photocleaving of thiolated gelatin to induce guided cell migration

Gel-SH hydrogel pellets have been prepared according to the description in Section 4.3.3. A gel-SH with a degree of substitution of 56% and a concentration of roughly 4.1% was chosen for all experiments. The power values used for photocleaving in the present work are above the threshold that has previously been established. In terms of parameter optimization to improve guided cell migration, the design, the cell culture media and the printing power have been adapted similarly to gel-MA (see Section 5.2 for further details).

Upon multi-photon absorption, previously formed crosslinks were cleaved, leading to a decrease in the elastic modulus. At a certain laser power all crosslinks should be cleaved, which results in a liquid pre-crosslinked hydrogel. No measurements of the changes in the materials' properties upon photocleaving have been performed in the present work.

5.1.1 PEG-(oNB-A)$_2$ cytotoxicity

Coculture spheroids have been encapsulated in 4.1% gel-SH ds 56 and structures have been photocleaved around them to study their effect on cell migration. While ASCs migrated into the cleaved structures as well as the bulk hydrogel, HUVECs generally remained in the spheroid's core. We hypothesized therefore, that the hydrogel contains a cytotoxic component. DAS has proven to be cytocompatible with ASCs up to a concentration of 4 mM and up to 2 mM upon UV irradiation [186]. The viability of HUVECs was 76% after 24 hours of exposure to a 2 mM DAS solution as indicated in Fig. 5.1. Although a concentration of 2.4 mM, which was used in the present work, has an adverse effect on HUVECs, it is unlikely that this is the main factor causing the observed cell behavior. Firstly, not only HUVECs, but also ASCs suspended in the hydrogel did not migrate and proliferate and secondly, the observed behavior of encapsulated HUVECs does not coincide with the expected viability reported in 5.1. Still, it is worth testing whether photocleaving at suitable laser powers is also possible if the concentration is decreased to 2 mM or less, due to the cytotoxic tendency of DAS for higher concentrations upon UV

irradiation, which simulates the multi-photon absorption process [186] and the adverse effect on HUVECs.

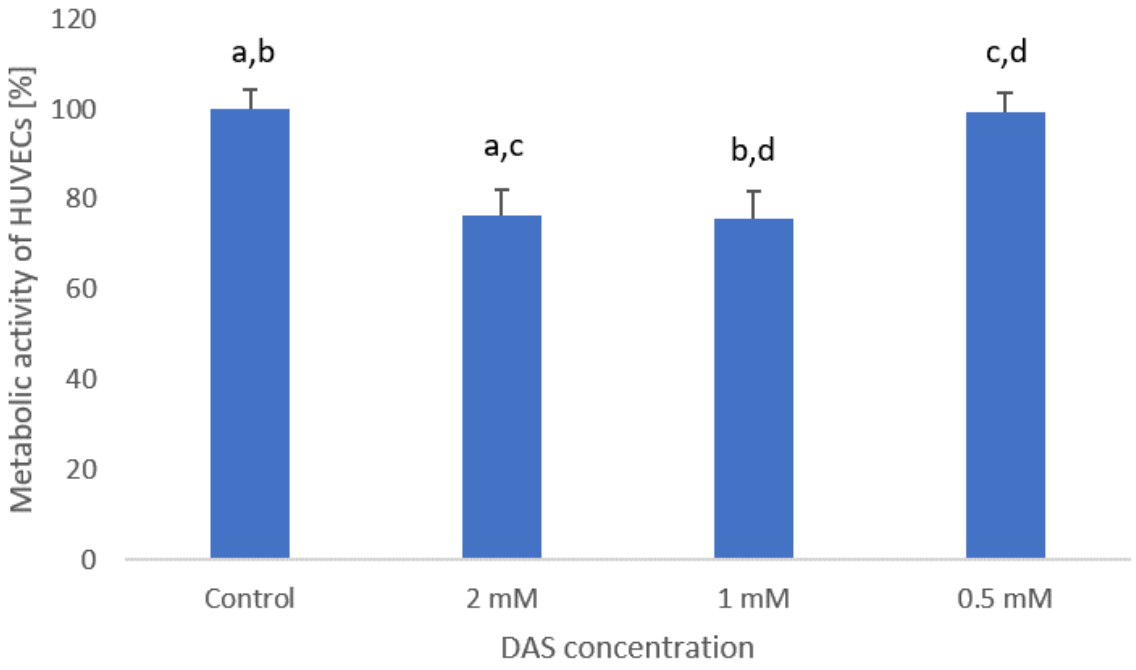

Figure 5.1. Determination of cytotoxic behavior of DAS on HUVECs using the PrestoBlue cell viability assay. Letters indicate significant difference at $p < 0.05$ level.

To test the cytotoxicity of the PEG-oNB photocleavable crosslinker, a comparative study with a commercially available Poly(ethylene glycol) diacrylate crosslinker (PEGda, Sigma-Aldrich), that does not contain the photocleavable moiety but is similar in all other aspects, was performed. HUVEC-RFP monoculture spheroids and ASCs in suspension were encapsulated in gel-SH according to the same protocol, crosslinked with either the PEG-oNB or the commercial crosslinker, and the cell behavior has been subsequently observed with a LSM. Fig. 5.2 displays a comparison of the cell behavior in the respective hydrogels. It is evident, latest on day 10 (compare Fig. 5.2A2 and 5.2B2), that both cell types have migrated and proliferated strongly in the commercially crosslinked gel-SH while in the oNB-PEG crosslinked gel-SH, the suspended ASCs have retained a round morphology and did not migrate into the hydrogel, which indicates that they are dead, and HUVECs remained aggregated as spheroids but they remained fluorescent, over the 14 days. On day 14, the commercially crosslinked hydrogel (see Fig. 5.2A3) was vastly populated by cells, and a quite extensive network of HUVEC sprouts has formed. This emphasizes the cytocompatible nature of gel-SH.

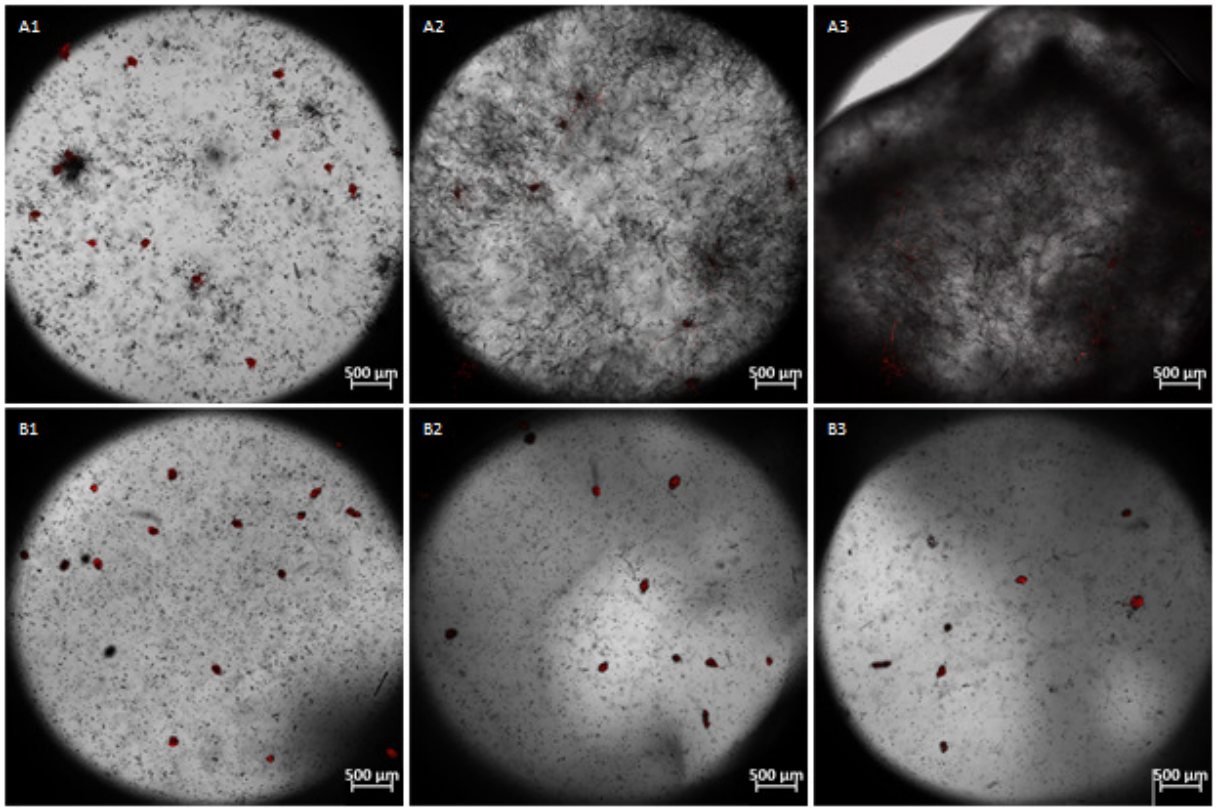

Figure 5.2. RFP-HUVEC spheroids with ASCs in suspension encapsulated in 4.1% gel-SH ds 56, crosslinked with (A1-A3) commercial PEG diacrylate crosslinker and (B1-B3) PEG-(oNB-A)$_2$ photocleavable crosslinker. Images were taken on (1) day 2, (2) day 10 and (3) day 15 after encapsulation. Images are magnified 2.5 times and the scale bars represent 500 µm.

The results strongly suggest that the PEG-(oNB-A)$_2$ photocleavable crosslinker, that has been used in the present work, is cytotoxic. As to the reason why, there are two possible explanations, one being that this linker contains cytotoxic molecules and the other one being that impurities during synthetization are responsible for the cytotoxic effect.

To test whether or not the linker itself is cytotoxic, an extensive literature research has been performed. In the study by Lunzer et al. [172], on which the present work is building upon, no cytotoxicy assessment of the PEG-oNB crosslinker was done. Microchannels have been cleaved around ASC spheroids and the cells have been reported to migrate into them over a period of 14 days, which is consistent with the findings of the present work. Generally, PEG-(oNB-A)$_2$ is referred to as PEG di-photogegradable acrylate (PEGdiPDA) in the literature. All analyzed papers, using either this linker or a similar adaptation, are based on a previously published preparation protocol [190]. Many of the studies have not included a cytotoxicity assay, probably because such an assay is included in the aforementioned preparation protocol. There, MSCs have been encapsulated in a hydrogel formed by free-radical chain polymerization between polyacrylate kinetic chains and PEGdiPDA,

and a live/ dead staining after encapsulation as well as a metabolic activity test after 24 and 48 hours have been performed. Some studies have included an assessment of the cytotoxicity, such as a live/dead staining of MSCs encapsulated in a PEGdiPDA crosslinked hydrogel, with a subsequent observation over 4 days without a reported cytotoxic behavior [191]. Tamura et al. [192] have encapsulated two cell types in a hydrogel formed by click-reaction of azide-modified gelatin with tetra arm-PEG (DBCO-PC-4armPEG) in different concentrations. They performed a live/dead cell viability assay after 24 hours and reported no cytotoxic behavior. Truong et al. [193] used a hydrogel formed by alkyne-azide cycloaddition (SPAAC) of PEG20k-4arm and gelatin, and performed a live/dead cell viability assay and a metabolic activity assay on day 1, day 3 and day 7 with L929 mouse fibroblast cells. They reported no cytotoxic behavior. Tsang et al. [194] formed a dydrogel by reaction of gel-MA and PEG-oNB-methacrylate. Encapsulated cells were imaged at days 0, 4, 6 and 14 and a live/dead cell viability assay was performed on cells seeded on hydrogel surface at day 3. They reported no cytotoxic behavior.

Cumulative, these results suggest that the PEGdiPDA crosslinker is cytocompatible. No publication in which a thiolated gelatin hydrogel is cross-linked with a PEGdiPDA cross-linker, besides the one mentioned above, has been identified during the literature research. Therefore, apart from our cross-linker being impure, the only other reason for cytotoxicity could arise from the Michael's type thiol-ene addition between the acrylate and the thiol groups. Since the commercial cross-linker undergoes the same reaction (and is non-cytotoxic) and this reaction should not yield cytotoxic side products [180], it is most likely that our cross-linker is cytotoxic due to impurities.

5.1.2 Guided cell migration

While the PEG-oNB crosslinker seems to be cytotoxic to ASCs in single cell suspension and HUVECs in general, as discussed in the previous section, ASC spheroids are an exception. It seems that the adverse effect is more pronounced for HUVECs than for ASCs. Moreover, the aggregation of ASCs into spheroids enables them to stay viable and to migrate into the hydrogel. This might be due to an interplay of different factors, such as the collective cell migration, which reduces the overall contact area with the cytotoxic component, the delayed exposure after encapsulation of the majority of ASCs and the general beneficial aspects of spheroids that have been discussed in Section 2.2. In Fig. 5.3 the migration of GFP-ASCs into cleaved microchannels is visualized over a period of 12 days. The ASCs have already significantly invaded the channels on day 2 and completed this process latest on day 5. Once the cells have reached the end of the channels, they are

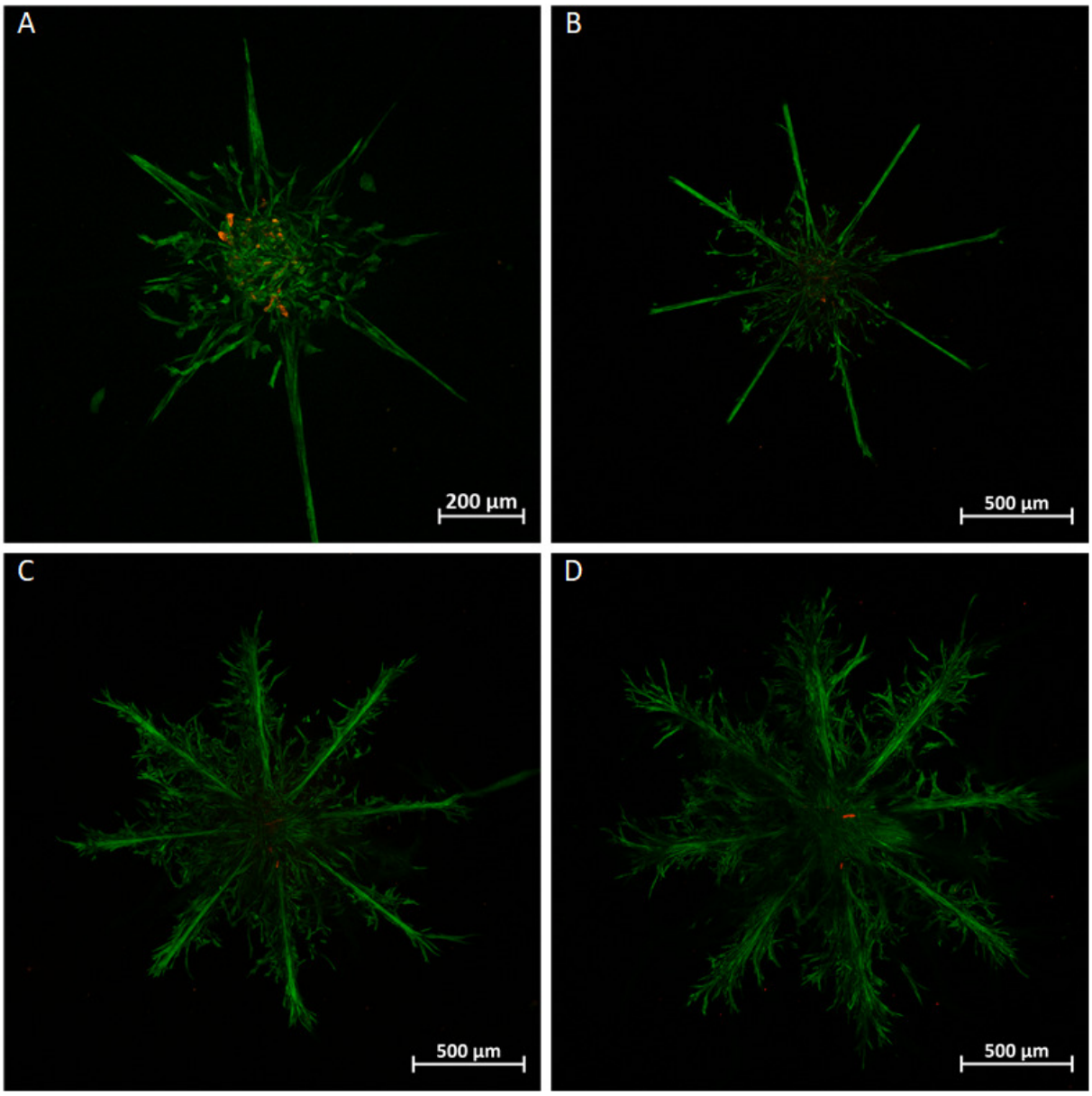

Figure 5.3. Coculture spheroid of RFP-HUVEC and GFP-ASCs in a 1:1 ratio encapsulated in 4.1% gel-SH ds 56, crosslinked with PEG-(oNB-A)$_2$ photocleavable crosslinker. Microchannels have been cleaved in a star shaped pattern around the spheroid. Images were taken on (A) day 2, (B) day 5, (C) day 8 and (D) day 12 after photocleaving. Printing parameters: power 130 to 300 mW, speed 1 000 mm/s, wavelength 700 nm. Images are magnified 10 times and the scale bars represent (A) 200 µm and (B-D) 500 µm.

migrating into the surrounding hydrogel and continue to do so over the whole observation period. Between day 8 and day 12 (compare Fig. 5.3C and Fig. 5.3D) the area covered by ASCs has noticeably increased, which indicates that they stayed highly active over the whole observation period. The red fluorescent signal of HUVECs seems to be decreasing over time. At day 12 only two red fluorescent spots remain visible in the center (see Fig. 5.3D).

The cleaved microchannels seem to be a promising tool for guiding cell migration and might be a viable method for guided HUVEC sprouting if the cytotoxicity problem can be resolved. Judging from the spontaneous HUVEC network formation in gel-SH with PEG diacrylate crosslinker (see Fig. 5.2), this could also be a well suitable hydrogel for photoinduced grafting.

5.2 Photografting of gelatin methacryloyl to induce guided cell migration

5.2.1 Material modification

The immobilization of a molecule on the hydrogel matrix upon multi-photon absorption can lead to a local change in the chemical and physical material properties. In the present work, DSSA, a hydrophilic molecule with two azide functional groups, which are capable of binding to C-H and N-H bonds upon their activation to nitrenes, was utilized as the photografting agent. If the two nitrenes are binding to different poplypeptides it is expected that the crosslinking density increases. It has been previously observed that the elastic modulus increases upon DSSA photografting for gel-MA with a high degree of substitution (95%) and decreases in gel-MA with a low ds (60%) [164]. The increase in elastic modulus, probably due to an increased crosslinking density, and the decrease in elastic modulus, probably due to a higher swelling ratio induced by the hydrophilic molecules, seem to be two counteractive effects. It is possible, that the diffusion of liquid in gel-MA is sufficiently impaired at higher degrees of substitution, so that the increased swelling in modified regions is not high enough to offset the influence of crosslinks, the number of which should increase with higher degrees of substitution.

We aimed to measure the changes in material properties for the gel-MA used in the present work, however, up to the concentration of 10% the hydrogel was too soft for reliable AFM measurements. Preliminary results suggest that the elastic modulus for 10% gel-MA ds 63 is roughly 0.4 kPa 24 hours after hydrogel formation and drops to roughly 0.1 kPa after another 24 hours. The estimated value for the 5% concentration is somewhere around 0.005 kPa. Considering that in previous rheology measurements of 5% and 10% gel-MA ds 63, with the same photoinitiator working solution, the elastic moduli were 0.54 kPA and 7.3 kPa, respectively, there is a big discrepancy to the present work [195]. Possible explanations will be discussed in Section 5.2.6. The effect of photografting on the material properties was of the greatest interest for the present work. While it was not possible to

obtain conclusive results in this regard, a trend towards a decrease in elastic modulus upon photografting in 10% gel-MA was observed. Previous measurements of grafted regions in 5% gel-MA ds 60 (DSSA working solution of 1 mM or 2 mM) yielded a range of elastic moduli from roughly 1.4 kPa to 0.1 kPA for a laser power of up to 190 mW and a laser scanning speed of 1 000 mm/s [164].

5.2.2 Threshold test

To determine the lower grafting threshold for different laser powers and printing speeds, an array of cubes, each column with a different printing power and each row with a different printing speed, was photografted in 5% gel-MA. The layout was an 19x3 array of cubes (100x100x100 µm feature size, 200 µm distance in x-direction, 250 µm distance in y-direction) with increasing power in x-direction from 20 mW to 200 mW in steps of 10 mW and with increasing printing speed in y-direction from 500 mm/s to 1 500 mm/s in steps of 500 mm/s. Two such tests have been performed, both with the same material concentration of 5% and the same DSSA concentration of 1 mM. Following the observations in the first experiment, the maximum printing speed was reduced to 1 000 mm/s and the maximum printing power to 140 mW. The DSSA soaking time has been increased from 2 hours in the first experiment to 24 hours in the subsequent experiment, to determine the influence of soaking time on the grafting threshold.

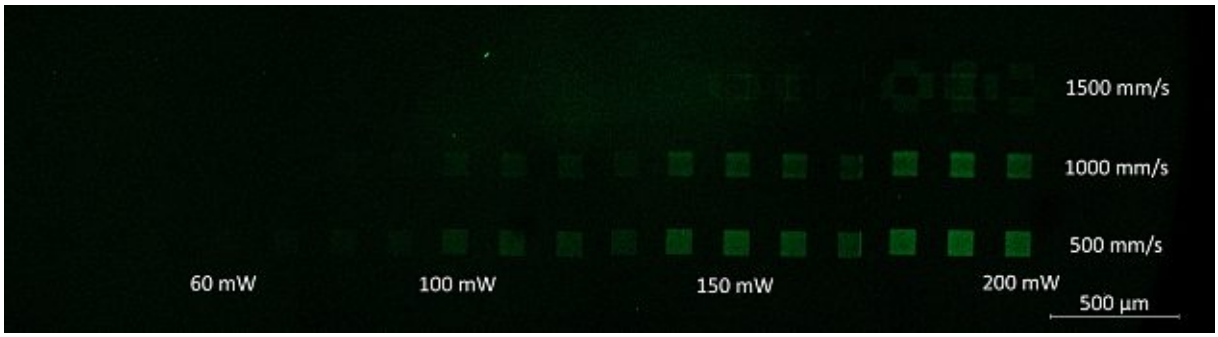

Figure 5.4. Photografted array of cubes in 5% gel-MA ds 63 after soaking in DSSA for 2 hours. Grafted areas are fluorescing in green. The scale bar represents 500 µm.

In the first experiment, with a DSSA soaking time of 2 hours, the cubes started to be visible at around 70 mW for 500 mm/s and 80 mW for 1 000 mm/s, as shown in Fig. 5.4. However, the background noise is quite high due to residual DSSA solution that remained in the pellet after the washing process. Grafting at 1 500 mm/s did not result in the desired cubes. This is due to the scanning velocity dependent time delay between the set position and the actual position caused by the inertia of the scanning mirror, which

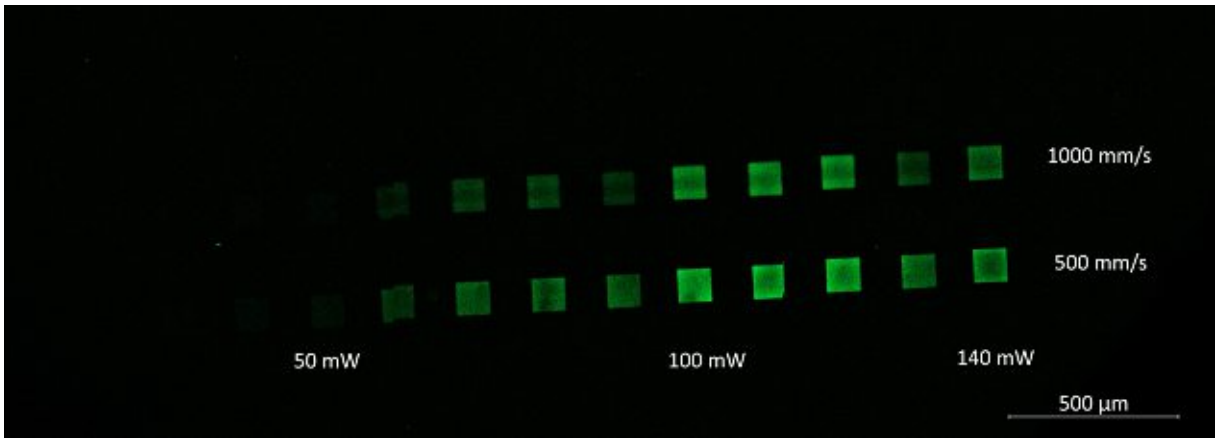

Figure 5.5. Photografted array of cubes in 5% gel-MA ds 63 after soaking in DSSA for 24 hours. Grafted areas are fluorescing in green. The scale bar represents 500 µm.

can only be compensated in a certain range of velocities [164]. With a longer soaking time of 24 hours, the cubes started to be visible at 50 mW for 500 mm/s and 60 mW for 1 000 mm/s (see Fig. 5.5). A comparison of the grafting results for samples that have been either stored in the incubator (37 °C, 5% CO_2, humid) or at room temperature throughout the DSSA soaking period displayed no difference in the threshold.

The maximum printing speed for DSSA photografting in 5% gel-MA ds 63 is between 1 000 mm/s and 1 500 mm/s, most likely at the lower end. An increase in printing speed from 500 mm/s to 1 000 mm/s shifts the lower laser power threshold only marginally, by roughly 10 mW. A longer DSSA soaking time (24 hours instead of 2 hours) decreases the grafting threshold by roughly 20 mW for both printing speeds, indicating that 3 hours might be a sufficient amount of time for DSSA to reach a diffusion equilibrium in a pellet of 30 µL of the tested hydrogel. The type of hydrogel, the degree of substitution, the hydrogel concentration or the degree of crosslinking influences the time until a homogeneous distribution of DSSA in the hydrogel is reached. Since 24 hours of DSSA soaking seems to be more than sufficient, it is not possible to draw any conclusions, in terms of increased speed of DSSA diffusion, from the comparison of incubator and non-incubator stored samples. One would need to perform this experiment at soaking times of 2 hours or less to evaluate the impact of this parameter.

5.2.3 DSSA cytotoxicity

The effect of the DSSA grafting agent on the metabolic activity of ASCs and RFP-HUVECs was tested for concentrations of 4, 2 and 1 mM with a PrestoBlue cell viability assay, which acts as an indication for the cytotoxicity of the grafting agent. As depicted

in Fig. 5.6A, ASCs exposed to DSSA and UV irradiation, show a significant higher metabolic activity compared to the control. There is no significant difference between different DSSA concentrations. Exposure of ASCs to DSSA without UV irradiation shows no significant effect on the metabolic activity. For RFP-HUVECs, displayed in Fig. 5.6B, there is a significant difference in comparison to the control for all tested concentrations, except for 2 and 1 mM in the non-UV irradiation group.

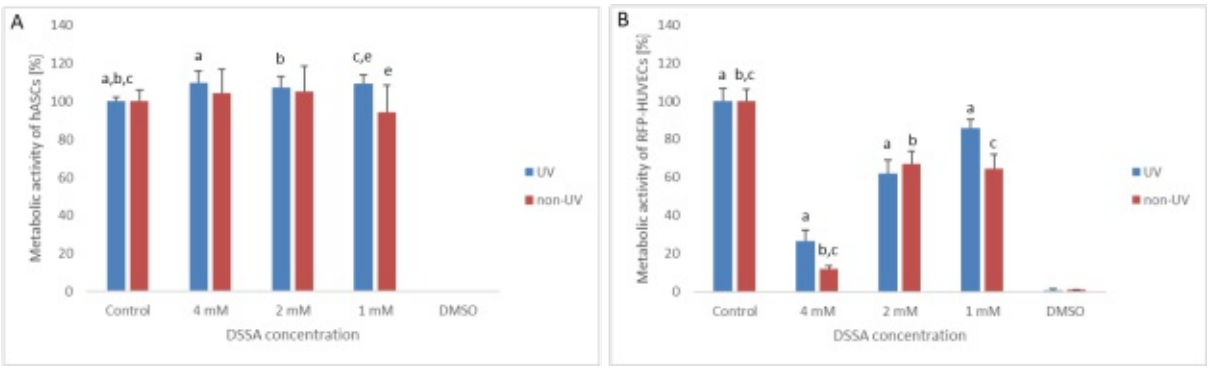

Figure 5.6. Determination of cytotoxic behavior of DSSA on (A) ASCs and (B) RFP-HUVECs using the PrestoBlue cell viability assay. Letters indicate significant difference at $p < 0.05$ level. In graph (B), all values are significantly different in comparison to the control within the UV group and within the non-UV group, except for 2 mM and 1 mM.

The results indicate that DSSA and UV irradiation has no adverse influence on ASCs, whereas RFP-HUVECs are strongly affected. A concentration dependent effect is visible for RFP-HUVECs, whereby the increase in DSSA concentration leads to a lower metabolic activity. Therefore, with a metabolic activity of around 86%, the 1 mM concentration has been selected for the following experiments.

5.2.4 Effect of hydrogel concentration on cell behavior

To test the effect of the gel-MA concentration on ASCs, 1.2 million cells/mL were encapsulated in hydrogel pellets at concentrations of 5%, 7.5%, 10% and 12.5%, and their proliferation rate was measured by staining of the Ki-67 protein and subsequent quantification of the fluorescent signal, the survival rate was visualized by live/dead staining and the metabolic activity was determined with a PrestoBlue cell viability assay, at day 1, 4, 7 and 13 after encapsulation.

Proliferation

Even though the anti-Ki-67 antigen was deliberately diluted in a higher concentration (1:200) to account for staining in a 3D hydrogel, the fluorescent signal was very low. Therefore, the results should be interpreted with caution and a new protocol for Ki-67 staining inside of hydrogel pellets needs to be established.

Under the assumption that cells are in a proliferative state upon encapsulation, the normalized fluorescent signal of the consecutive time points are displayed in Fig. 5.7 as a percentage of the fraction of the respective time point to day 1. A sharp drop in the proliferation rate is visible for all concentrations except 5%, with a tendency towards recovery between day 7 and day 13. Nevertheless, it is only in 5% (see Fig. 5.7) that the proliferation rate returns to or even exceeds the day 1 value. The only exception is 12.5%, for which a stark increase in proliferation rate between day 4 and 7 has been measured. However, considering the aforementioned problems with staining and the observations in further experiments in which encapsulated ASCs populated the hydrogel pellets less with increasing concentrations, this result is rather unlikely to be correct.

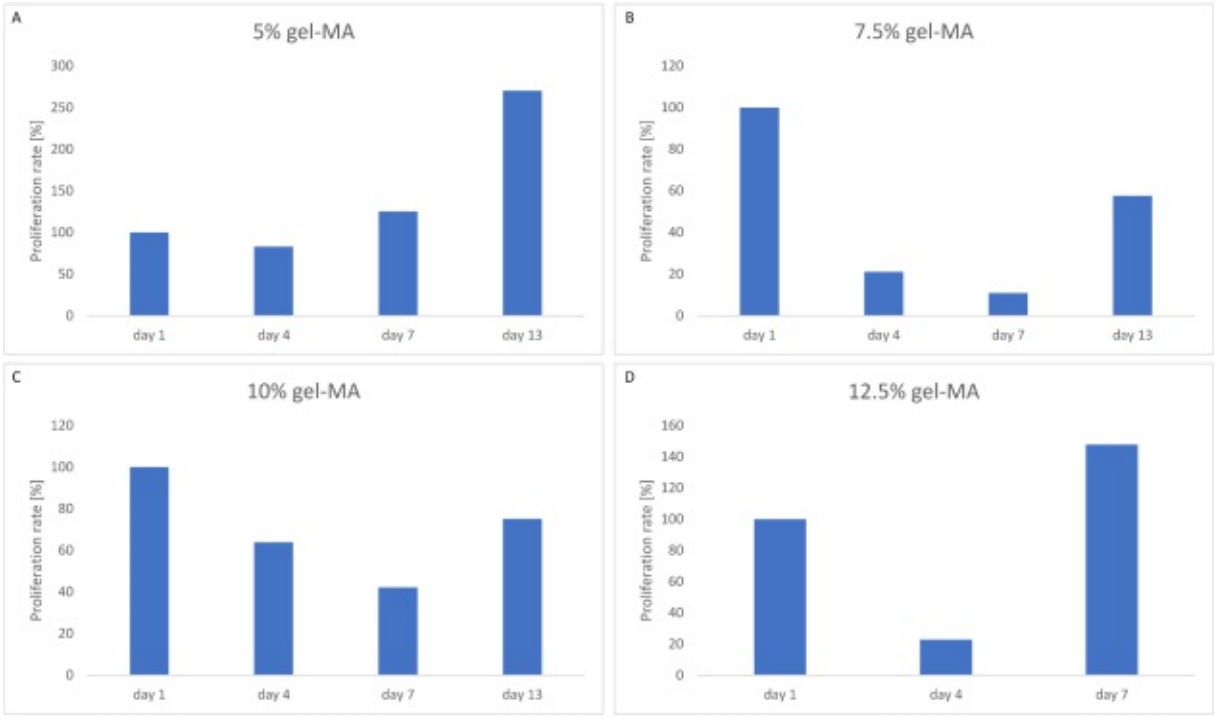

Figure 5.7. Quantification of the proliferation of ASCs encapsulated in gel-MA ds 63 with concentrations of (A) 5%, (B) 7.5%, (C) 10% and (D) 12.5%. Each consecutive time point is displayed as a fraction of the day 1 value. No usable data exists for 12.5% on day 13. The sample size is 1.

Due to the uncertainty of the data it is not possible to draw direct conclusions on the

influence of gel-MA concentration on the proliferation rate of ASCs. Nonetheless, the trend of an initial drop and a subsequent recovery of the proliferation rate seems to be quite robust.

Live/ dead staining

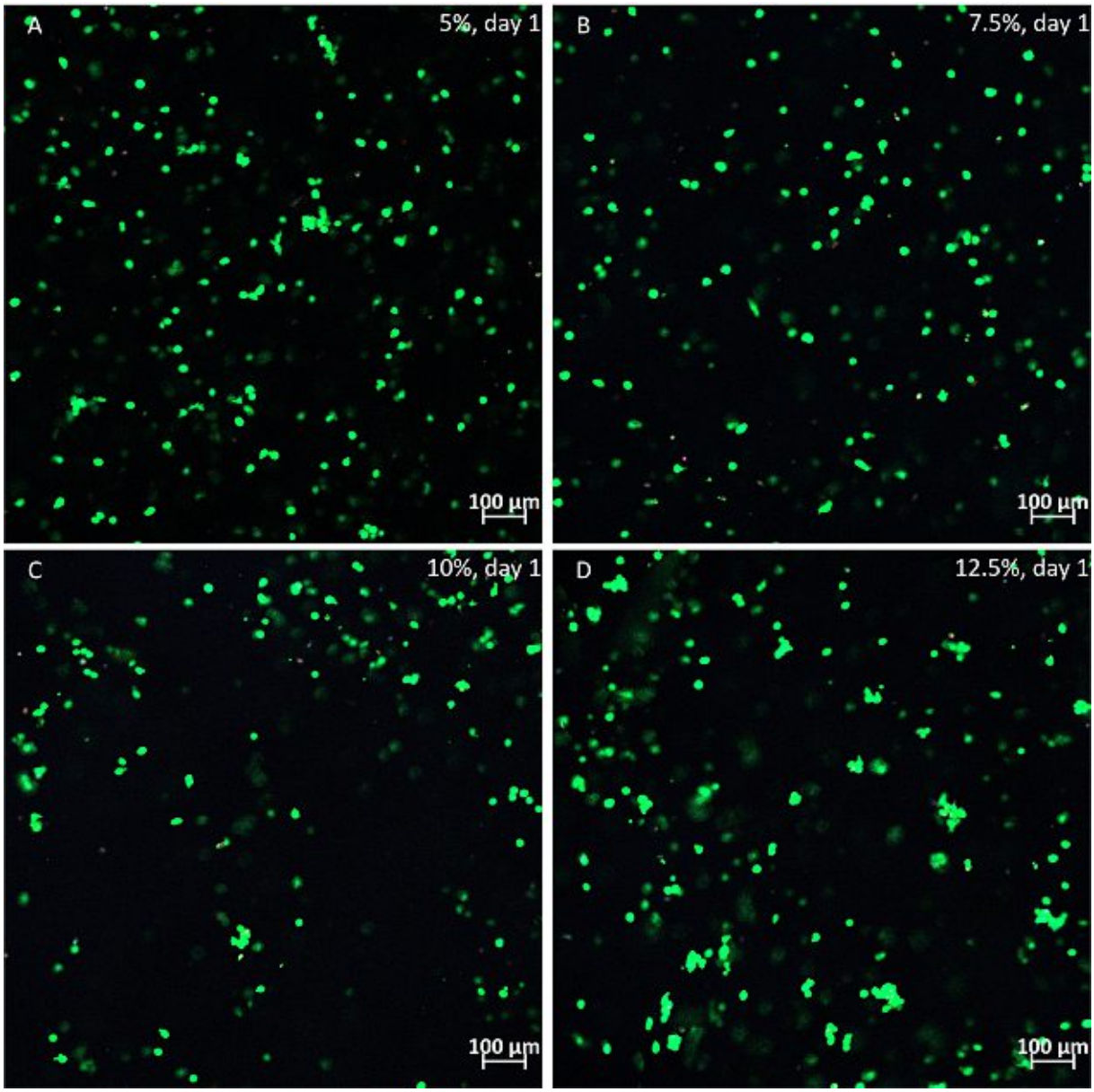

Figure 5.8. ASCs encapsulated in (A) 5%, (B) 7.5%, (C) 10% and (D) 12.5% gel-MA ds 63. The cells were stained on day 1 with Hoechst (nucleus, blue), calcein-AM (live cells, green) and PI (dead cells, red). Images are magnified 10 times and the scale bars represent 100 µm.

Encapsulated ASCs have been stained on day 1, 4, 7 and 13 after encapsulation. However, the staining did not work well on day 4, 7 and 13 for 5% gel-MA and on day 13 for all concentrations. While the reason for that is not known to the author, the 12.5%

concentration has been re-stained on day 14 with the same results, indicating that the problem did not arise from the staining procedure.

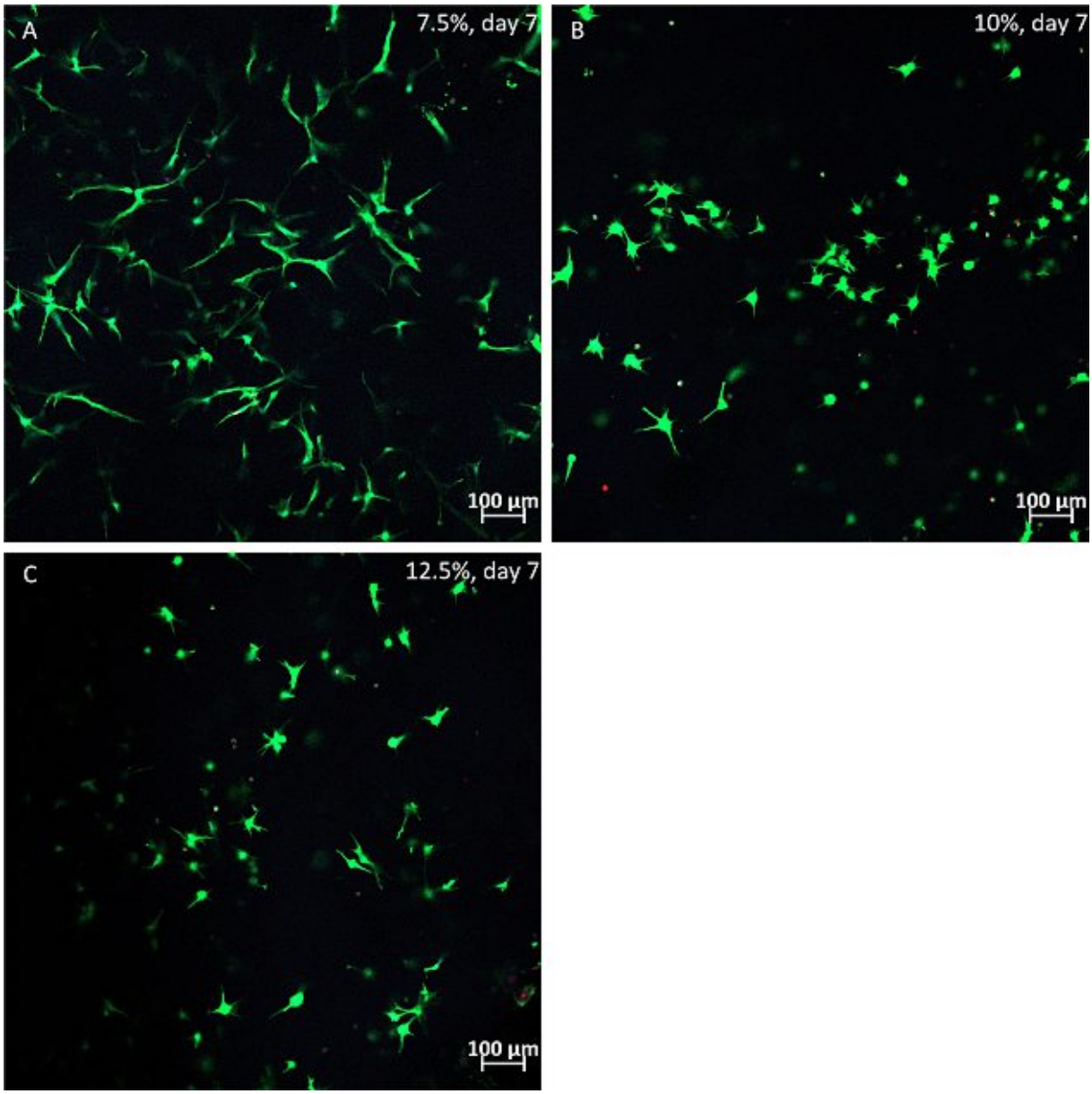

Figure 5.9. ASCs encapsulated in (A) 7.5%, (B) 10% and (C) 12.5% gel-MA ds 63. The cells were stained on day 7 with Hoechst (nucleus, blue), calcein-AM (live cells, green) and PI (dead cells, red). Images are magnified 10 times and the scale bars represent 100 µm.

As displayed in Fig. 5.8, the vast majority of ASCs were alive on day 1 after encapsulation for all tested material concentrations. This shows that the encapsulation process is cytocompatible and that the material concentration has no initial adverse effect on cell survival. On day 7, the majority of cells is still alive in all stainable concentrations, as shown in Fig. 5.9. While not very pronounced, a slight trend towards a higher fraction

of dead cells in hydrogels with higher concentrations is visible. It is well noticeable in Fig. 5.9 that the cells are spread a lot more in 7.5% compared to higher concentrations. This suggests that lower gel-MA concentrations provide a more suitable environment for ASCs.

Metabolic activity

The metabolic activity of ASCs encapsulated in 5%, 7.5%, 10% and 12.5% gel-MA is presented in Fig. 5.10, for days 1, 4, 7 and 13 after encapsulation, as the fluorescent intensity (Fig. 5.10A) or the percentage fraction with regard to day 1 (Fig. 5.10B). In general, the metabolic activity is increasing over time for all concentrations. The difference in metabolic activity between different concentrations on day 13 seems negligible. The metabolic activity on day 4 and 7 seems to be highest for 5% and 12.5%.

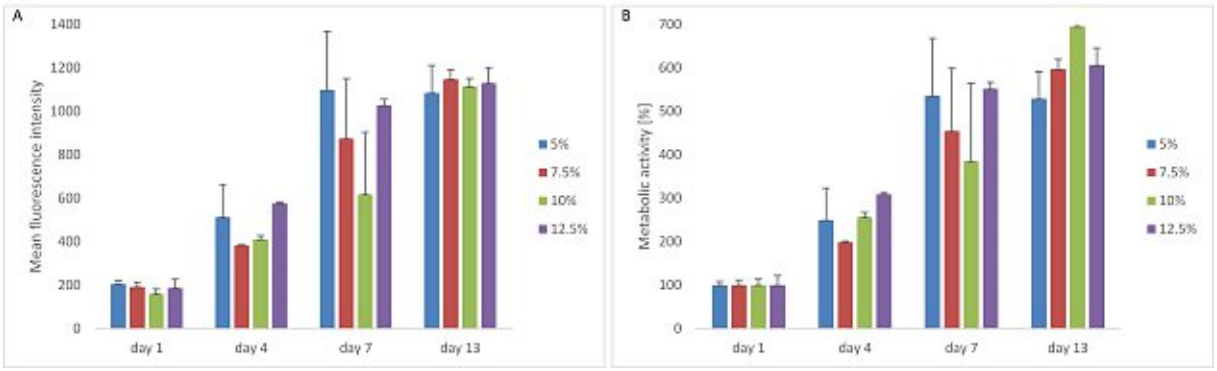

Figure 5.10. Quantification of the metabolic activity of ASCs encapsulated in 5%, 7.5%, 10% and 12.5% gel-MA ds 63. The metabolic activity is presented as either (A) the mean fluorescence intensity or (B) the percentage fraction compared to day 1. The sample size is 2.

While the results suggest that over longer encapsulation times the gel-Ma concentration has no effect on the metabolic activity of ASCs, it is odd that at intermediate time points (day 4 and 7) cells encapsulated in the highest and lowest tested concentrations (5% and 12.5%) show the highest metabolic activity. A subsequent test with a sufficient sample size to allow for a statistical analysis is necessary to validate the present data.

5.2.5 Cell alignment

To study the response of ASCs to DSSA-modified patterns, a mesh-like structure has been photografted within a cell-laden gel-MA pellet and the cell behavior has been observed over the course of 13 days. The structure consists of 10 parallel elongated cuboids (10x10x500 µm, separated by 50 µm), superimposed by 10 parallel elongated cuboids,

rotated at a 90-degree angle. Alternative mesh-like designs have shown that a decrease of either the feature size or the separation distance leads to seemingly less cell alignment. Fluorescent images visualizing the alignment on day 13 after grafting are displayed in Fig. 5.11. The modified regions are fluorescing in blue and the ASCs are fluorescing in green. By a direct comparison of the images with and without the blue-fluorescent channel (Fig. 5.11B and Fig. 5.11C) the alignment of ASCs is highlighted. It is well visible in Fig. 5.11C that the ASCs have a preferential orientation in the horizontal and vertical direction. A quantification assay has been performed on the basis of this data. The results (Fig. 5.11A) are in agreement with the observed patterns, stating that roughly 41% of cells are oriented horizontally and vertically, as compared to roughly 20% percent in the non-grafted control. This indicates that the cells can sense the modified regions and respond accordingly by orienting their shape in alignment with the given pattern.

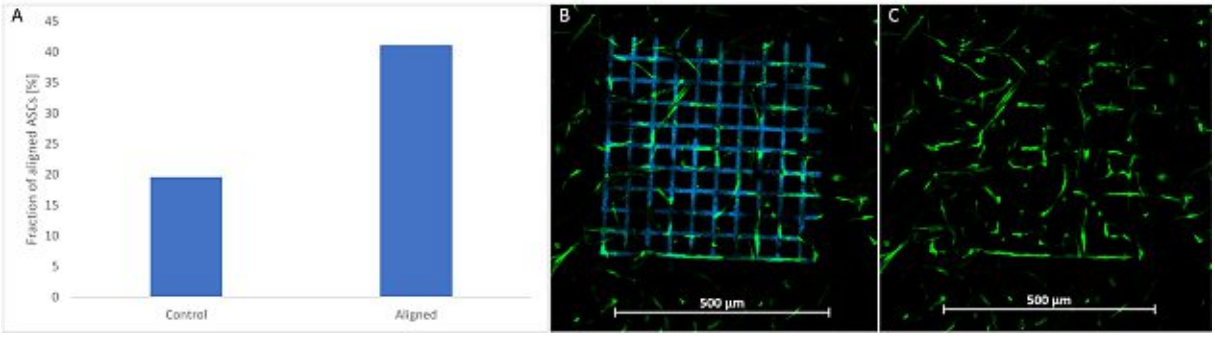

Figure 5.11. (A): Quantification of the orientation of hASCs in response to a photografted pattern on day 13. (B and C): GFP-ASCs encapsulated in 5% gel-MA ds 63 at a density of 1 000 cells per 1 µL. Image was taken on day 13 after grafting. In image (A) the grafted structure is fluorescing in blue. This signal is suppressed in image (B) to highlight the cellular alignment. Printing parameters: power 125 mW, speed 500 mm/s, wavelength 700 nm, layer spacing 0.5 µm. Images are magnified 10 times and the scale bars represent 500 µm.

5.2.6 Parameter optimization

It became evident early on that HUVEC sprouting is directly dependent on preceding ASC migration, in the sense that HUVECs only migrate into areas where ASCs are present and they seemingly do so in a ASC-density dependent manner. Therefore, in discussing the different parameters, that have been assessed for their potential to enhance guided cell migration, the emphasis will be on guided vs. random ASC migration and the subsequent impact on HUVEC sprouting. The analyzed parameters have been the printing power, the design of the grafting structure, the material concentration, the cell encapsulation methods and the coculture ratios.

Various factors, such as the cell passage, the spheroid formation process, the spheroid encapsulation process and the location of the spheroid within the hydrogel, introduce a high level of variability between different samples, which makes it rather difficult to reach comparative conclusions. The location of the spheroid has been identified as a major factor in influencing random and guided ASC and HUVEC migration. It seems that the presence of a certain number of ASCs is necessary to induce HUVEC migration. In interpreting the results, an effort is made to take this variability into account, by trying to draw conclusions from general trends that have been noticed throughout the experiments.

We observed in the initial experiments that ASCs are superior to HUVECs in terms of speed and extent of migration. As a result, the fraction of fetal calf serum in the cell culture medium, which was added to the hydrogel pellets, was changed from 10% to 5%, to favor the performance of HUVECs. The design of the photografting structure has been iteratively adapted to facilitate a maximal coverage of the spheroids' surface, in order to reduce random cell migration. By trying different cell encapsulation methods, we concluded that coculture spheroids are most suitable for the efforts of the present work. Different material concentrations of 5%, 7.5%, 10%, 15% and 20% have been tested, and 5% has proven to be most effective. Increasing the fraction of HUVECs in coculture spheroids did not allow us to draw a definite conclusion on the most suitable ratio due to the aforementioned variability between samples. A longer spheroid culture time (11 days) showed an enhanced ASC behavior and a dampened HUVEC behavior, which is exactly the opposite of what would be beneficial for the present work. Studying cell migration with varying printing powers revealed that this parameters has an effect on the migration speed of ASCs.

Printed structure

The CAD-files, which are to be printed within the hydrogel, have been designed in a way that facilitates spheroid grafting, with differently shaped structures facing outwards from a circular center, which roughly corresponds to the shape of the encapsulated spheroids. Following this general design principle, several iterations have been made according to previously obtained experimental results. The first printed structure resembles a vascular tree with two bifurcations and corresponding decreasing diameters from 30 µm to 20 µm to 15 µm, as depicted in Fig. 5.12A. Four such structures were grafted perpendicular to each other. The main problem was that a preferential migration of ASCs was barely discernible. Moreover, contrary to previous believes, guiding HUVEC sprouting turned

out to be difficult, consequently a simpler printing structure seemed more suitable. The design has been adapted to eight elongated cuboids assembled in a star-shaped pattern (see Fig. 5.12B), and developed further to isosceles trapezoidal-like structures (see Fig. 5.12C), a design which ensures that the printed area in close proximity to the spheroid is sufficiently large to direct the cells towards the printed structures and subsequently minimize random migration, and at the same time allows to study the capability of cells to migrate into structures with a small feature size. Since the spheroids are 3D constructs and sprouting can occur at any point on the spheroids' surface, the design has been enhanced by stacking three identical layers on top of each other, to maximize the overall amount of guided migration. Adding a connecting sphere in the middle has not led to visible improvements and exposed the cells to the possible adverse laser, and has therefore been discarded.

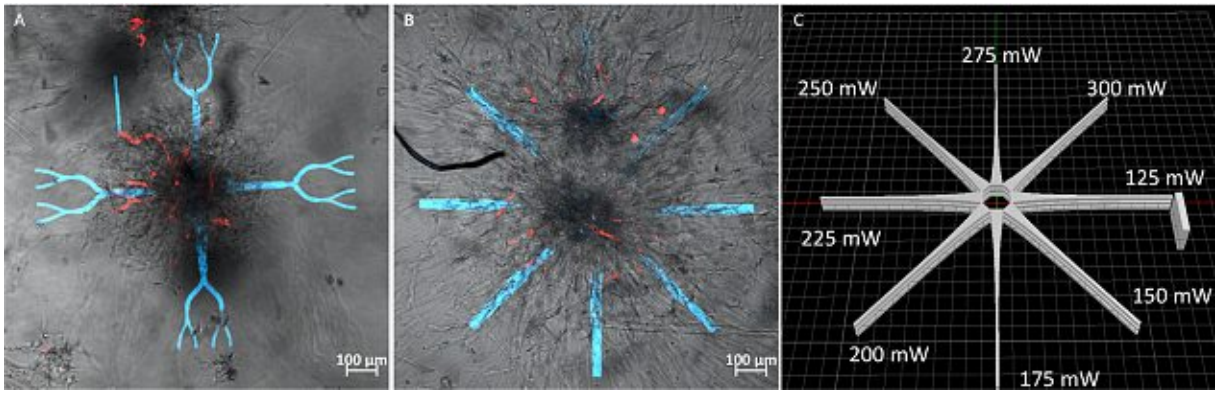

Figure 5.12. Overview of the evolution of the photografted structures. The design has changed from a (A) photografted vascular tree with two bifurcations (diameters of 30 µm, 20 µm and 15 µm, respectively) to (B) photografted elongated cuboids (30x30 µm) and the final 3D-station design (C) with three layers of isosceles trapezoidal-like structures (cross section: largest 100x30 µm, smallest 20x30 µm). Images (A and B) are magnified 10 times and the scale bars represent 100 µm.

To maximize the ratio between guided and random ASC migration, a final design, with 24 elongated isosceles trapezoidal-like structures (largest cross section: 100x30 µm; smallest cross section: 20x30 µm; length: 1200 µm), arranged in three star-shaped layers to ensure full coverage of the spheroid's vertical surface, displayed in Fig. 5.12C, has been created. Some experiments required an adaption of the length. Since the overall structure is essentially assembled by arranging the 24 elongated isosceles trapezoidal-like structures in the 3D-station, it is possible to change the individual printing parameters. In the present work, each direction was printed at a different power, the values of which are displayed in Fig. 5.12C, to study the influence of printing power on directional cell migration. A

cuboid has been printed to denote the structure with the starting power and to indicate the direction of increasing laser power.

Cell encapsulation method

Cells can be either encapsulated in suspension, as spheroids or as a combination of both. To induce HUVEC sprouting the presence of this cell type is indispensable. However, if HUVECs are encapsulated in gel-MA on their own, either in suspension or as spheroids, or the density of ASCs is too low, they retain a round morphology and do not migrate into the hydrogel. The following combinations have been explored in the present work; coculture spheroids, HUVEC spheroids with ASCs in suspension, ASC spheroids with HUVECs in suspension and both cell types in suspension. Experiments with HUVECs in suspension yielded overall bad results, possibly due to problems in achieving the right seeding density. This approach has not been further pursued because other approaches seemed more promising. It could be beneficial, though, to add HUVECs in suspension to encapsulated coculture spheroids.

The encapsulation of HUVEC spheroids and ASCs in suspension yielded ambiguous results. Fig. 5.13 displays the migration and alignment of ASCs and RFP-HUVECs to the photografted structure over the course of 7 days. By comparing the first row, which shows the grafted structure fluorescing in blue, and the second row the migration of ASCs towards the grafted structure, indicated by a difference in ASC density and highlighted by white arrows (see Fig. 5.13B2 and Fig. 5.13C2), is visible and most pronounced at the left facing vascular tree. ASC migration seems to be highest between day 1 and day 4 (compare Fig. 5.13A2 and Fig. 5.13B2), however, an increase in ASC density on the photografted structure is also visible between day 4 and day 7 (see white arrow on the far left in Fig. 5.13C2). In terms of HUVEC migration, only the left facing vascular tree shows an overlap with a sprout, indicated by the red arrows in Fig. 5.13B1 and Fig. 5.13B2. Arguably, this is also the structure with the highest perceived ASC density and the results could be interpreted as an indication for the potential of this method to achieve guided HUVEC migration. However, due to presence of ASCs in close proximity to the grafted structures it is easy for the HUVECs to deviate from their predetermined path (see green arrow in Fig. 5.13B1). A maximum intensity projection (MIP) of the RFP-HUVECs red fluorescent signal, displayed in Fig. 5.13B3 and Fig. 5.13C3 for day 4 and day 7, respectively, reveals that the shape of the vascular network is not resembling the grafted structure. It has to be kept in mind that some of the sprouts are outside of the 30 µm grafted layer and therefore have no incentive to follow the structure.

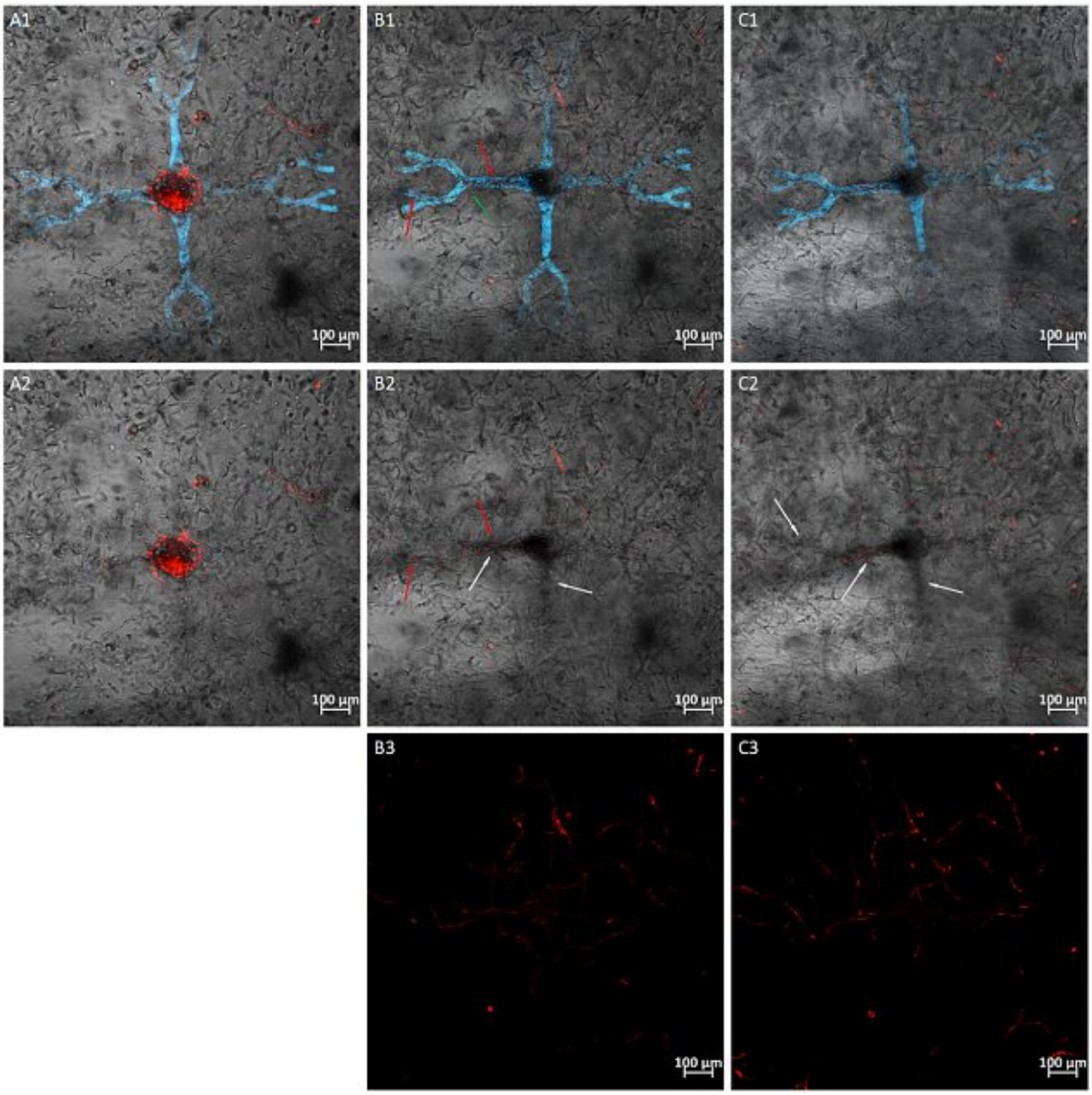

Figure 5.13. RFP-HUVEC spheroids with ASCs in suspension encapsulated in 10% gel-MA ds 63. Images were taken on day 1 (first column), day 4 (second column) and day 7 (third column) after photografting. The first row shows the photografted structure fluorescing in blue, the RFP-HUVECs fluorescing in red and a brightfield image of the ASCs. In the second row the fluorescent signal has been suppressed to visualize the ASC alignment. The third row is a MIP of the red fluorescent signal to highlight the vascular network that has been formed. Printing parameters: power 100 mW, speed 500 mm/s, wavelength 700 nm. Images are magnified 10 times and the scale bars represent 100 µm.

A big obstacle to this approach is the fact that the number of ASCs which are not aligned to the grafted structure, during the time that is relevant for HUVEC migration, seem to be too high to sufficiently confine the HUVEC migration. Still, it could make sense

to further explore this method and adapt the grafting design as well as the printing parameters. Generally, coculture spheroids seem like the most promising strategy and have therefore been selected for subsequent experiments.

Hydrogel concentration

The initial experiment with coculture spheroids was conducted in 5% gel-MA, following promising, previously reported results regarding spontaneous HUVEC sprouting and network formation [53]. No HUVEC sprouting was observed in this experiment, however, it became evident that ASC migration is quicker than HUVEC migration and that in this particular setup the ratio between random and guided ASC migration is high. The underlying hypothesis, for testing different hydrogel concentrations, was that an increased concentration will slow down ASC migration and favor guided over random migration, which is essentially dependent on the extent of the chemical and physical difference between modified and bulk hydrogel. To test this hypothesis, ASC spheroids were encapsulated in 10%, 15% and 20% gel-MA and cell migration was observed.

With increasing concentrations the process of cell encapsulation and pellet formation gets more and more difficult. A concentration of 20% is not suitable for recurrent experiments with a large sample size. In Fig. 5.14, an ASC spheroid encapsulated in 10% gel-MA is imaged over the course of 14 days. The migration of ASCs into the non-grafted regions was drastically impaired compared to previously conducted experiments in 5% gel-MA. Although slightly less pronounced, the same was observed for migration into the grafted regions. This trend was even stronger for higher concentrations, and spheroids in 20% gel-MA did not deviate from their original shape. Overall, the fraction between guided and random migration seems to have increased from 5% to 10%. Cell migration was negligible between day 5 (see Fig. 5.14B) and day 7 (see Fig. 5.14C), and came to a halt between day 7 and day 14 (see Fig. 5.14D).

To test whether the intermediate concentration of 7.5% is better suitable and whether there is a difference between mono- and coculture spheroids, coculture spheroids of different ratios have been encapsulated in 5% and 7.5% gel-MA and observed over a period of 12 days. The higher hydrogel concentration performed similarly to slightly worse in terms of guided cell migration.

It needs to be mentioned, that in other experiments with 10% gel-MA, namely the encapsulation of HUVEC spheroids and ASCs in suspensions (see Fig 5.13), and the en-

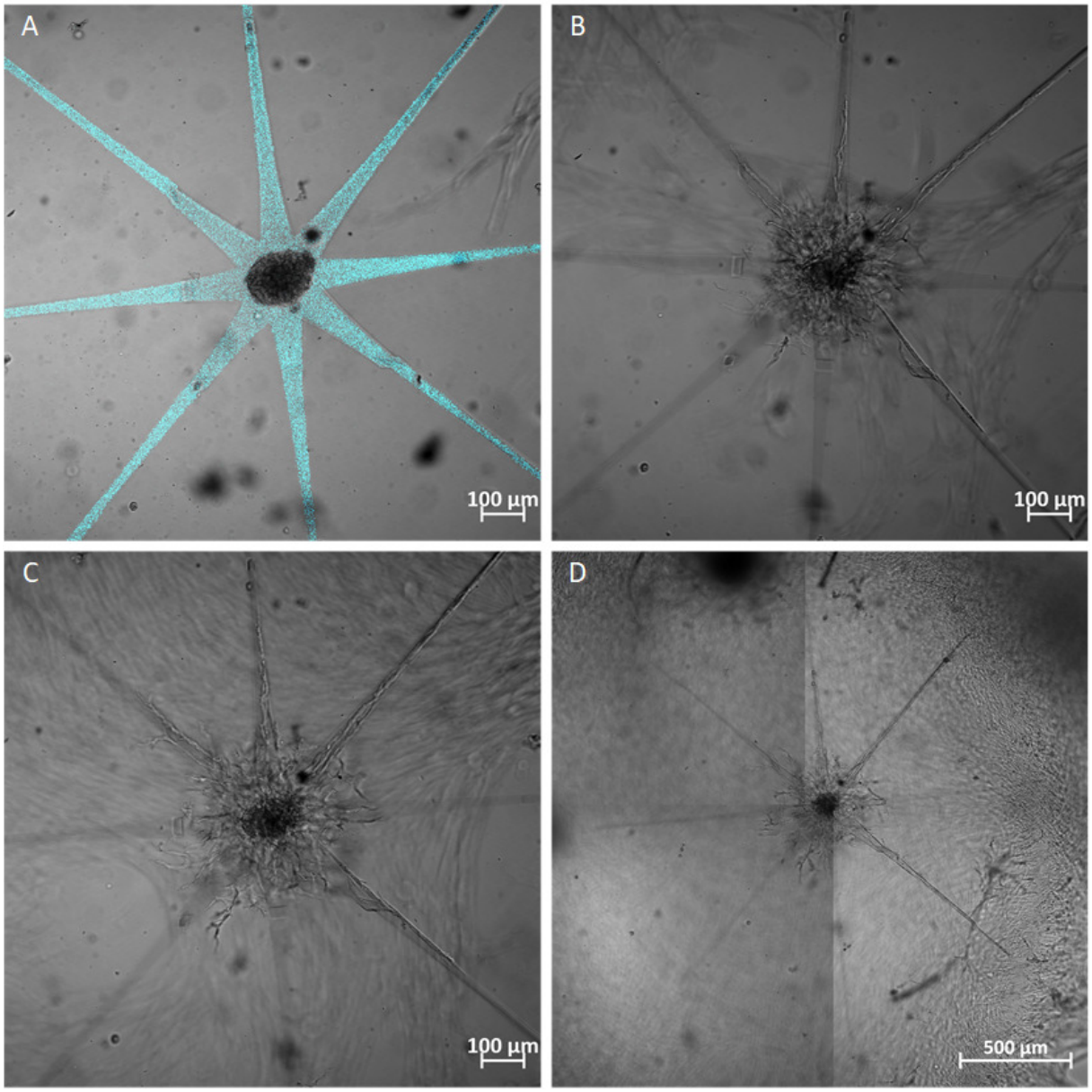

Figure 5.14. ASC spheroid encapsulated in 10% gel-MA ds 63. The photografted structure is fluorescing in blue (A) and has been suppressed in images (B-D) to better visualize ASC migration. The images have been taken on (A) day 1, (B) day 5, (C) day 7 and (D) day 14. Printing parameters: power 125 mW to 300 mW, speed 500 mm/s, wavelength 700 nm. Images are magnified 10 times and the scale bars represent (A-C) 100 µm and (D) 500 µm.

capsulation of coculture spheroids cultured for 14 days prior to encapsulation, the cells were performing better in terms of migration and proliferation. While it is coherent that longer cultivation periods lead to increased ASC migration, the reason for the better performance of ASCs in suspension might be caused by an incentive to migrate towards each other and form aggregates, which is already given in spheroids, or it might be due to variations between experiments, such as the cell passage or slight deviations in the grafting and imaging process. According to rheology measurements of 5%, 7.5% and 10% gel-MA

ds 63 in an equilibrium swollen state, crosslinked with 0.6 mM Li-TPO-L, the storage moduli are roughly 0.54 kPa, 3.6 kPa and 7.3 kPa, respectively [195]. Preliminary AFM measurements of the hydrogels used in the present work, which are in theory identically to the ones described above, indicated that 5% and 7.5% gel-MA are too soft to obtain reliable results of patterns at the micrometer scale with an AFM (estimation of elastic modulus far below 0.1 kPA), and that the elastic modulus of 10% gel-MA is around 0.4 kPA and 0.1 kPa for measurements on day 1 and day 2 after hydrogel formation. While the present observation of slower ASC migration with increasing gel-MA concentration aligns with the findings by Zigon Branc et al. [195], it is questionable whether the elastic modulus is the pivotal factor in the present case. Two possible explanations for the discrepancy are that there is either a difference in the photoinitiator, potentially tracing back to the synthesis or stock solution preparation, or in the UV irradiation, which would result in more unreacted, potentially cytotoxic functional groups (methacrylamide and methacrylate), an effect that should be more pronounced for higher concentrations. In terms of UV irradiation, two different sources and durations of irradiation are used, resulting in an irradiation of 15 J/cm^2 and 11x10^{-4} J/cm^2 in the work by Zigon Branc et al. [195] and the present work, respectively. It was not possible to address these questions in the present work due to delayed AFM measurements. Therefore, a comprehensive comparative study addressing these issues remains to be performed.

Regardless of the underlying reasons, the selection of 5% gel-MA as the concentration for subsequent experiments is coherent with the obtained results, that are in accordance with previous observations, according to which an increased material concentration/ storage modulus impairs ASC migration from spheroids [195].

Coculture ratio and early vs. late encapsulation

The choice to combine ASCs and HUVECs into spheroids in a 1 to 1 ratio was based on the results from a preceding study on the optimal ratio for spontaneous sprouting, which stated that increasing the fraction of HUVECs, up to a maximum fraction of 50%, increased the mean tubule length and mean number of sprouts [53]. Therefore, we speculated that a higher HUVEC fraction might lead to even better results in terms of spontaneous sprouting and, even more relevant for the present work, in terms of guided sprouting, by decreasing the delay in migration between HUVECs and ASCs and reducing random ASC migration. The aforementioned study also included a comparison of sprouting between coculture spheroids encapsulated in 5% gel-MA ds 63 after 1 day (early encapsulation) or 11 days (late encapsulation) in culture. Late encapsulation resulted in

a significant reduction in HUVEC sprouts [53]. This experiment was repeated slightly different, to test whether a late encapsulation is beneficial for guided ASC and HUVEC migration, whether a higher fraction of HUVECs has a positive impact and whether diluting the agarose powder in sterile water instead of PBS has an effect on the cell behavior.

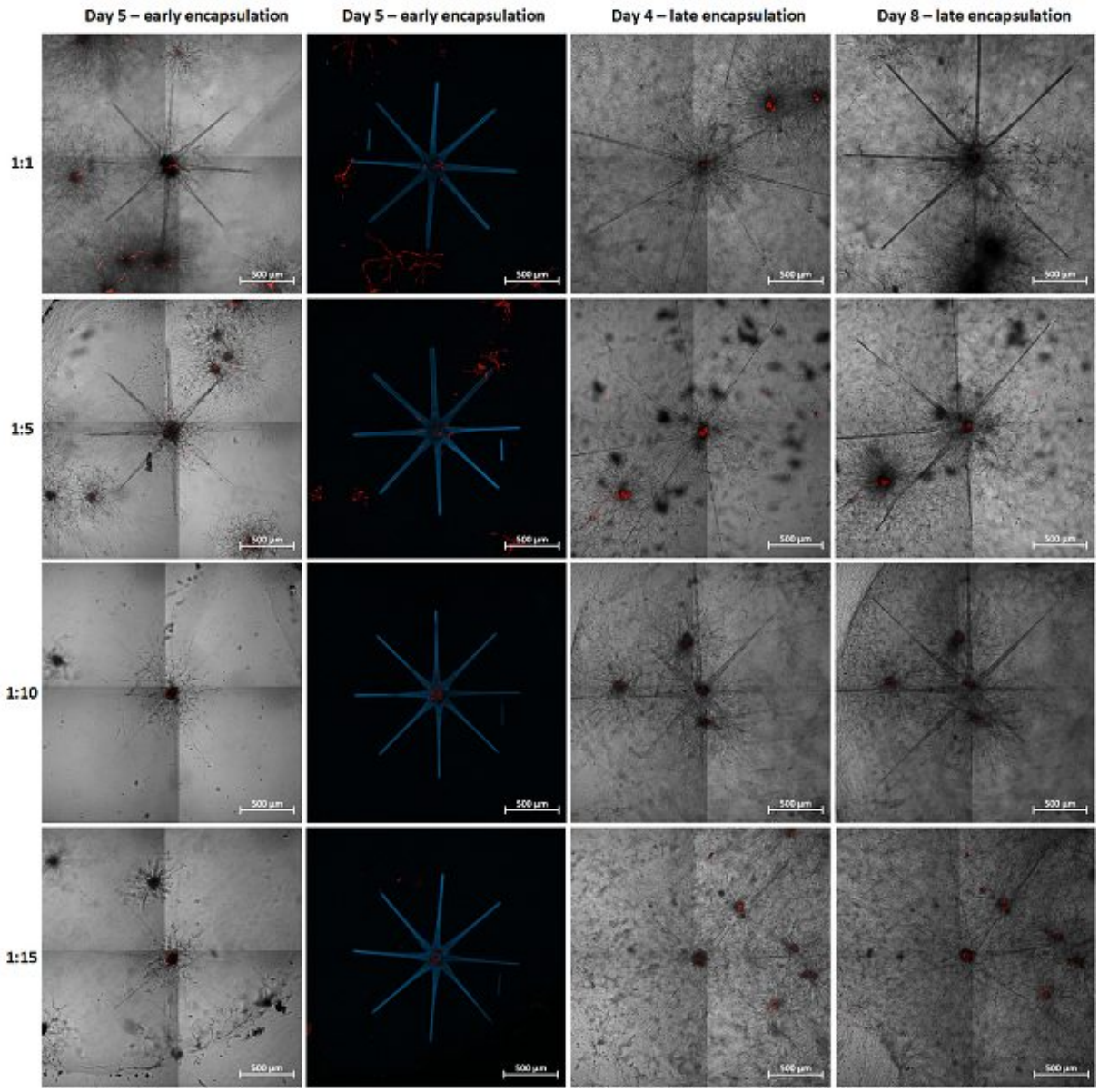

Figure 5.15. Coculture spheroids of ASCs and RFP-HUVECs encapsulated in 5% gelMA ds 63. The ratio of ASCs to HUVECs is indicated on the left of the figure and early (after 1 day) or late encapsulation (after 11 days) as well as the day on which the image was taken is indicated on the top of the figure. Images in the second column are a MIP. Printing parameters: power 125 mW to 300 mW, speed 1 000 mm/s, wavelength 700 nm. Images are magnified 10 times and the scale bars represent 500 µm.

Fig. 5.15 provides a direct comparison of the different ratios in vertical direction and between early and late encapsulation in horizontal direction. Regarding the migration of

ASCs, an increase in the fraction of HUVECs effectively leads to a decrease in the number of ASCs per spheroid, which results, as expected, in a decreased area of the hydrogel that is populated by ASCs. A bit more unexpected is the observation that from a certain ratio onward (i.e. 1:10, see Fig. 5.15) the directionality of ASC migration decreases. Longer culture times of the coculture spheroids resulted in an increased ASC migration/ proliferation. The increased length of the grafted structures (adapted for experiments in which an enhanced migration was expected) for late encapsulation in Fig. 5.15 needs to be taken into account when comparing the migration distances.

Only early encapsulated spheroids with the ratio of 1:1 and 1:5 experienced HUVEC migration. Comparing the grafted to the non-grafted spheroids (see Fig. 5.15 1:1 early encapsulation) in the 1:1 early encapsulation sample reveals that HUVEC sprouting is impaired in the former. The presence of other spheroids could be a crucial factor, which would be in agreement with previous observations according to which HUVECs already formed sprouts on day 4 [53], potentially due to the fact that a lot of spheroids are in close proximity to each other. It is also possible that the laser has a significant adverse effect on HUVECs, which is why the connecting central sphere has not been printed in subsequent experiments.

Since it is not clear, based on the aforementioned results, whether or not a coculture ratio in between 1:1 and 1:5 is best suitable to induce HUVEC migration, coculture spheroids with the intermediate ratios of 1:2 and 1:3 have been encapsulated and subsequently observed. While the number of sprouts is higher for both ratios (see Fig. 5.16, compared to the 1:1 ratio (see Fig. 5.15), the variability between samples is too high to draw a definite conclusion, especially given the fact that in other experiments 1:1 coculture spheroids have experienced significantly more sprouts than in the sample shown in Fig. 5.15.

Spheroid position

The parameter with the most impact on guided as well as random ASC and HUVEC migration is the location of the spheroid within the hydrogel. The hydrogel preparation and cell encapsulation method employed in the present work does not allow for the manual control of the spheroids' position. According to observations of an extensive sample size, there are two positions in which a noteworthy number of HUVEC sprouts are occurring. The first one is in close proximity to the glass bottom of the microscopy dish and the second one in close proximity to a sufficient amount of other spheroids. The common

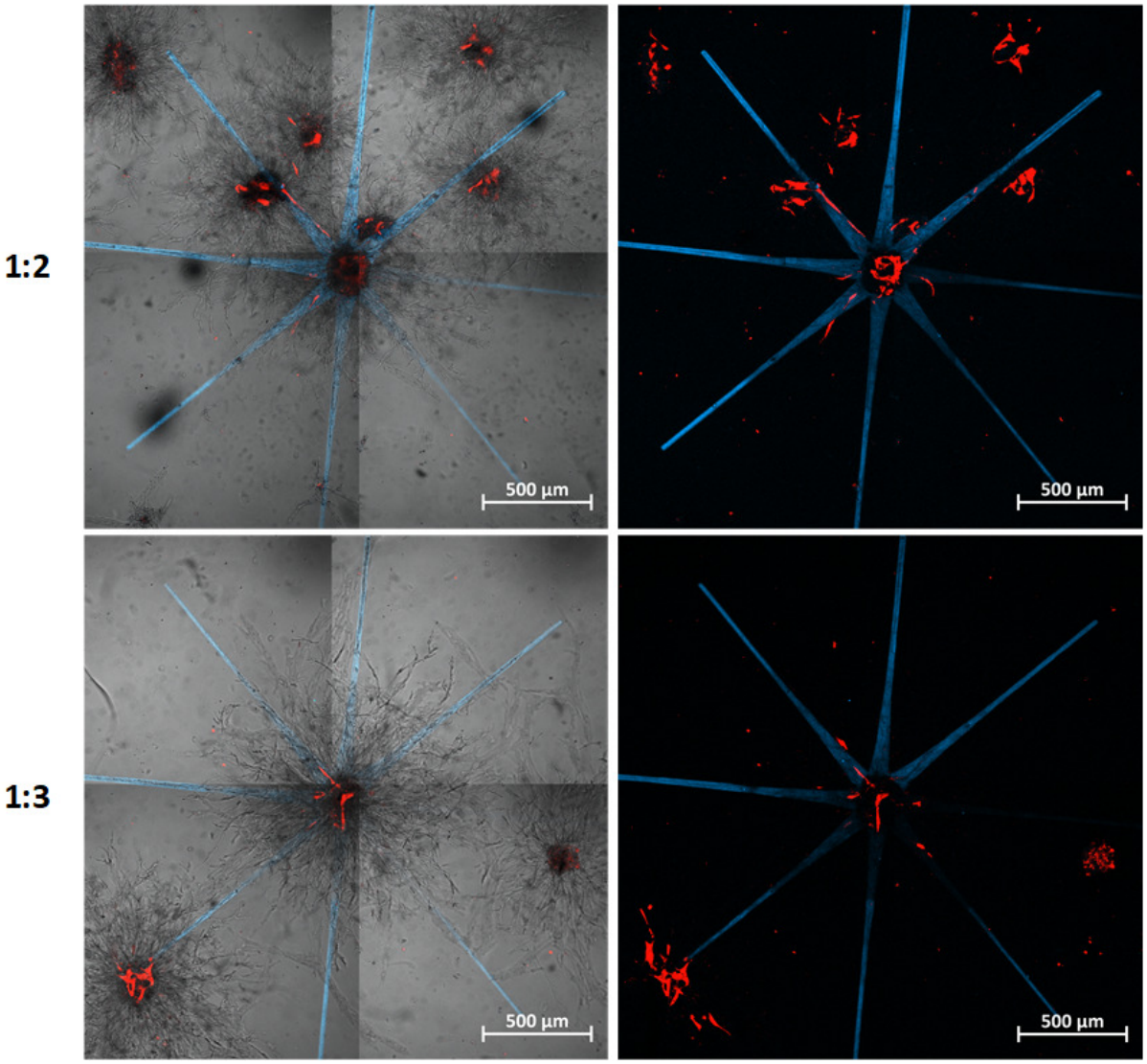

Figure 5.16. Coculture spheroids of ASCs and RFP-HUVECs encapsulated in 5% gel-MA ds 63, imaged on day 5 after grafting. The ratio of ASCs to HUVECs is indicated on the left of the figure. Images in the second column are a MIP. Printing parameters: power 125 mW to 300 mW, speed 1 000 mm/s, wavelength 700 nm. Images are magnified 10 times and the scale bars represent 500 µm.

denominator of both locations is the presence of a high number of ASCs, which, in the first location, results from an enhanced migration and proliferation of ASCs on the surface. This fact became obvious when the use of GFP-ASCs made it possible to visualize the position of ASCs layer by layer. In an effort to visualize photografting induced directional cell migration, the presence of spheroids in proximity to the grafted spheroids have initially been seen as a factor of disturbance, and it has therefore been actively tried to select standalone spheroids for grafting.

Printing power

In order to evaluate the impact of the printing power on directional ASC migration, the individual isosceles trapezoidal-like structures have been printed at different power settings, between 125 mW and 300 mW with a stepwise increase of 25 mW, as displayed in Fig. 5.12. The cell migration has been observed by means of time-lapse imaging over a period of 42 hours. The migration distance into the grafted structures has been plotted over the time in Fig. 5.17 for selected power values. Since the observed spheroids showed a large variability between each other, we used a linear mixed effect model to quantify the influence of both time and laser power on cell migration distance, to consider the random effects due to the individual samples. The model returned a strong effect of time on migration distance, coherent with the pictures we acquired and with the data in Fig. 5.17, and a weaker but still positive effect of power. The likelihood ratio test we performed against a model with no power confirmed that this effect is statistically relevant. This indicates that higher laser powers are better suitable for guiding cell migration. Since an overlapping between spheroids and grafted structure is unavoidable, potential adverse effects of the laser at higher powers remain to be addressed.

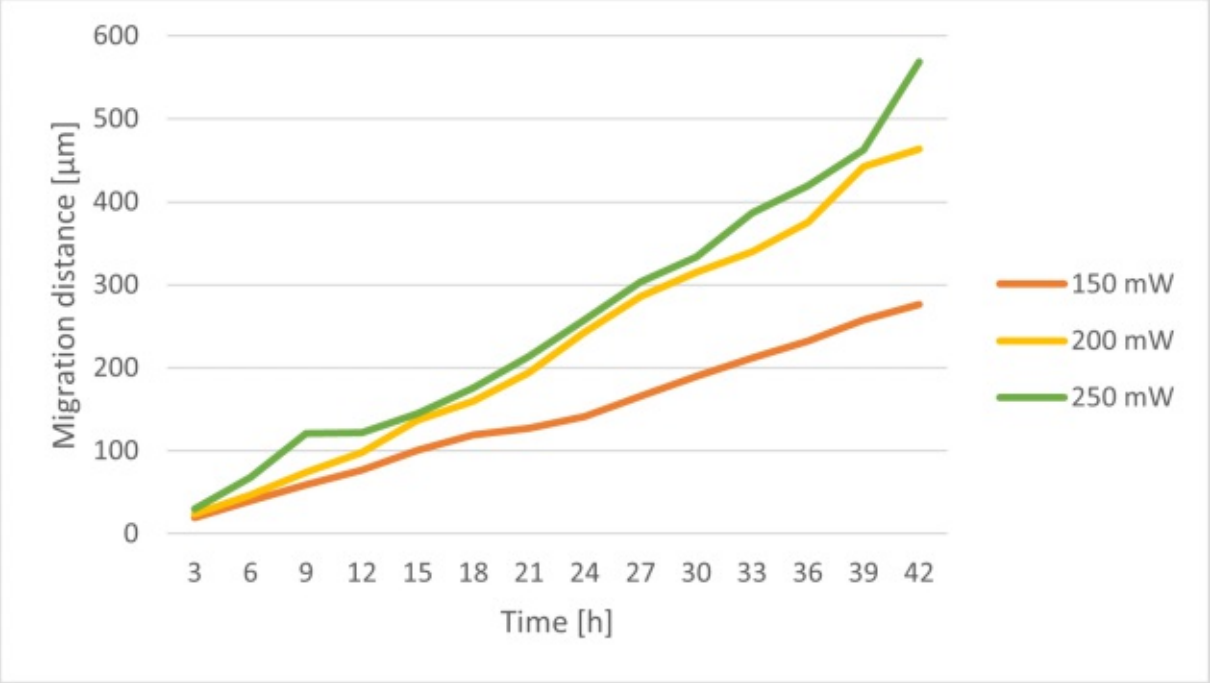

Figure 5.17. Quantificaton of the migration distance over time, for selected power values, of GFP-ASCs into the microchannels grafted at different power setting in 5% gel-MA ds 63, as observed with time lapse imaging over 42 hours. The results of up to five different samples are averaged. The standard deviation is high compared to the small sample size.

5.2.7 Guided cell migration

After having thoroughly discussed the various parameters that have been adapted in an effort to facilitate photografting induced guided cell migration and the limitations of the present approach in the previous section, the best results that have been obtained, in terms of directional ASC and HUVEC migration, are presented in the following.

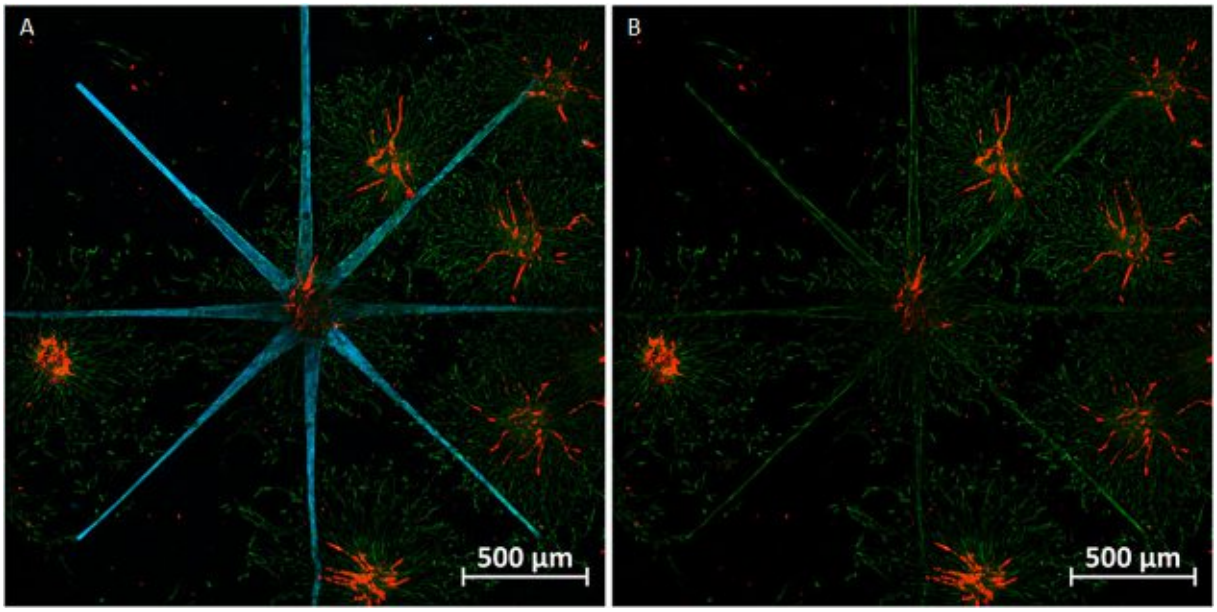

Figure 5.18. MIP of coculture spheroids of GFP-ASCs and RFP-HUVECs in a 1:1 ratio, encapsulated in gel-MA ds 63 at a concentration of 5%. Images were taken on day 3 after grafting. The blue fluorescent channel is not shown in image (B) to better highlight ASCs alignment along the grafted regions. Printing parameters: power 125 mW to 300 mW, speed 1 000 mm/s, wavelength 725 nm. The images are magnified 10 times and the scale bars represent 500 µm.

Guided ASC migration

In Fig. 5.18A, the grafted star-shaped structure, fluorescing in blue, is wrapped around the coculture spheroid located in the center of the image. The images have been taken on day 3 after grafting and are a MIP of a z-stack taken along the vertical diameter of the spheroid. Looking solely at the green fluorescent signal in Fig. 5.18B, the grafted star-shaped structure becomes clearly visible, confirming that the ASCs have migrated into the pre-defined regions. In areas where the photografted structure is in contact with other spheroids on the same plane the cell density is higher. This effect is especially pronounced in the top right region.

Guided HUVEC migration

Three of the samples that seem to show directional sprouting are displayed in Fig. 5.19. The images in the top row show the ASCs fluorescing in green and the HUVECs fluorescing in red, to highlight the dependence of HUVEC sprouting on the presence of ASCs. The bottom row of Fig. 5.19 displays the grafted structure fluorescing in blue and the HUVECs fluorescing in red. Although it seems that the sprouts are preferably oriented towards the grafted regions, there is still a considerable number of random sprouts that make it impossible to draw a definite conclusion on directionality given the limited sample size.

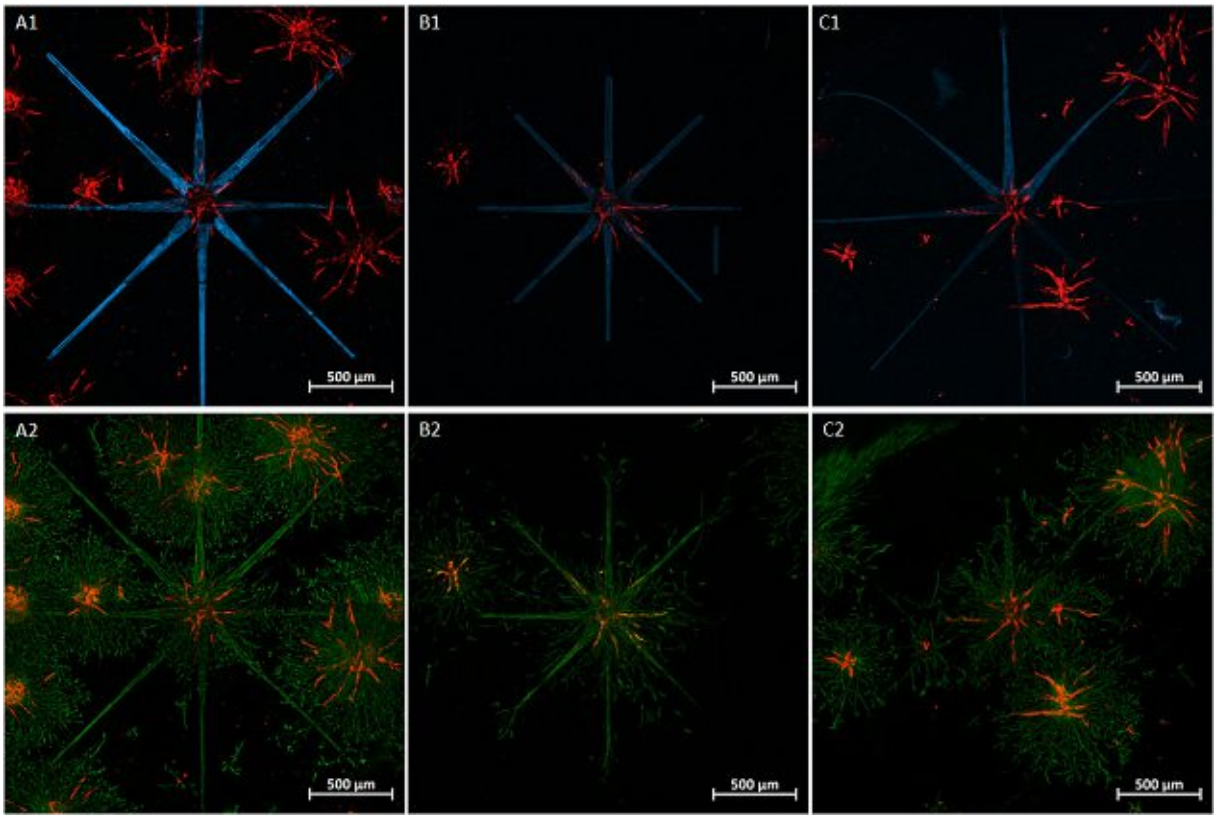

Figure 5.19. MIP of HUVEC sprouting: Coculture spheroids of GFP-ASCs and RFP-HUVECs in a 1:1 ratio, encapsulated in 5% gel-MA ds 63. Every column displays the same sample, with the first row showing the blue and red fluorescent channel to illustrate the dependence of sprouting on the positions of GFP-ASCs, and in the second row the green and red fluorescent channels are displayed to illustrate the directional sprouting in accordance with the photografted structure. The images have been taken on (A) day 3 and (B and D) day 5. Printing parameters: power 125 mW to 300 mW, speed 1 000 mm/s, wavelengths (B) 700 nm and (A and C) 725 nm. The magnification is 10 times and the scale bars represent 500 µm.

5.3 Photografting of collagen type 1 to induce guided cell migration

Collagen has been tested for its suitability as a hydrogel for photografting. The general mechanisms regarding the grafting-induced material modifications are the same as for gel-MA, and the reader is referred to Section 5.2.1 for further information.

5.3.1 Concentration and threshold test

Different collagen concentrations (3.6-4.95 mg/mL, 4.4-6.05 mg/mL and 5.6-7.7 mg/mL) have been prepared by mixing the collagen solution (high protein density of 8-11 mg/mL) with 10% of DSSA solution and either EGM-2 or PBS in the desired ratio as described in Section 4.3.2. The hydrogel turned opaque after gelation. This effect was more pronounced for increasing collagen concentrations. Since multi-photon lithography requires a certain level of optical transparency it was not possible to graft within concentrations higher than 3.6-4.95 mg/mL.

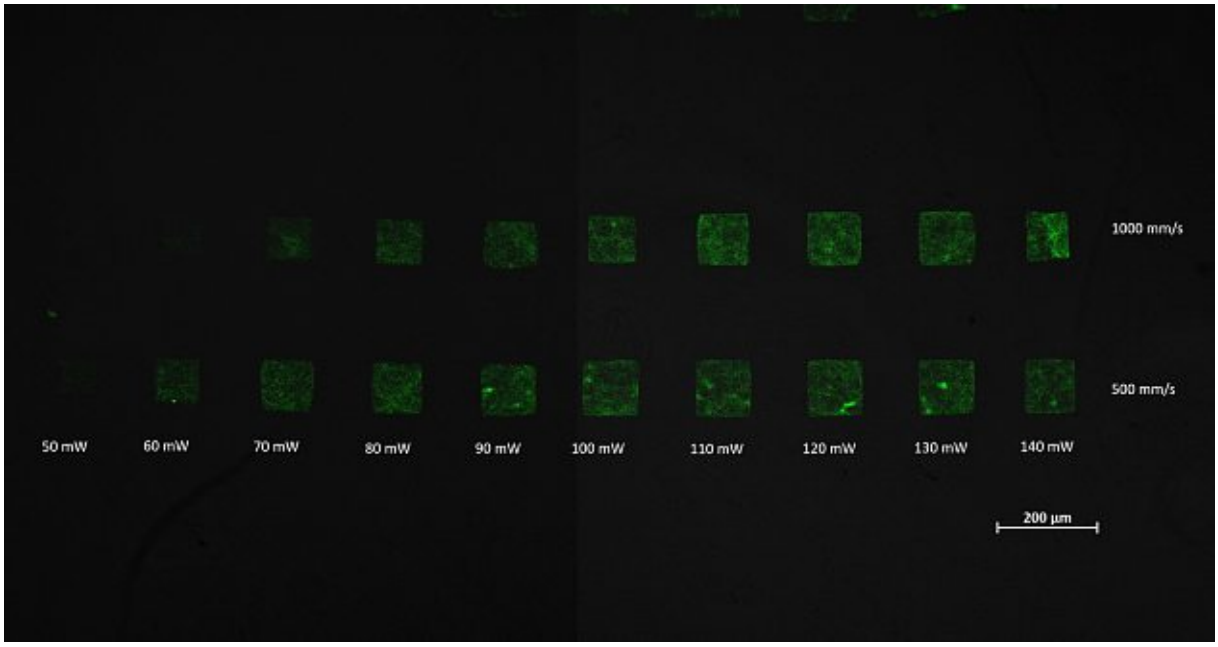

Figure 5.20. Photografted array of cubes in collagen type 1 at a concentration of 3.6-4.95 mg/mL. Grafted areas are fluorescing in green. The image is magnified 10 times and the scale bar represents 200 µm.

A threshold test was performed with the 3.6-4.95 mg/mL collagen concentration. A grid consisting of 13x2 cubes with 100 µm sides, with the power varying between 20 and 140 mW in uniform steps of 10 mW in x-direction and the speed varying in y-direction between 500 and 1 000 mm/s, as displayed in Fig. 5.20, was photografted. The grafted

structures were not visible with the µ-Eye camera of the printer. Fluorescent imaging of the structure revealed the photografted grid (see Fig. 5.20). The fluorescent intensity within the grafted cubes seems to be inhomogeneous. The shapes are deviating from the defined parameters and are different between individual cubes. In Fig. 5.20, the cubes start to be visible at 60 mW for 500 mm/s and at 70 mW for 1 000 mm/s, which are threshold values similar to those of gel-MA.

5.3.2 Problems and perspectives

As discussed in the previous section, photografting in collagen does not seem to produce structures with a consistent shape, most likely due to the opaqueness of the hydrogel. Another problem is that the pellets are not sticking to the glass bottom of the microscopy dish and start collapsing and dissolving after a couple of days. This seemed to happen even earlier in cell-laden collagen.

In the setup of the present work, it is impossible to create a collagen hydrogel with sufficient long-term structural stability that is at the same time transparent enough to enable multi-photon induced photografting. However, according to the protocol of the manufacturer, physical gelation is pH dependent and sodium hydroxide (NaOH) or sodium bicarbonate (NaHCO3) are recommended to be used for adjusting the pH to a value of 7.4. It is therefore very likely that the collagen hydrogel created in the present work was only slightly or not at all physically gelated. This could also explain the difference in structural stability of cell-laden (collagen mixed with EGM-2) and non cell-laden (collagen mixed with PBS) hydrogels. The suitability of properly gelated collagen as a hydrogel for multi-photon induced photografting remains to be evaluated in further experiments.

6 Outlook and Conclusion

It has been previously reported that cocultures of ASCs and HUVECs are capable of forming endothelial sprouts, expressing CD31 and VE-Cadherin, which are connecting to form a microvascular-like network [53]. This thesis aimed to utilize multi-photon lithography to control the spatial formation of this network. Specifically, the goal was to induce a directional migration of ASCs and HUVECs via multi-photon lithography. To this end, two different multi-photon lithography-based mechanisms, photo-induced grafting and photo-induced cleaving, have been tested in gelatin-based hydrogels.

Photo-induced cleaving has been applied to gel-SH. While it proved to be a good method to guide ASC migration, HUVECs did not form notable sprouts in any of the conducted experiments. By comparing the photocleavable PEG-oNB crosslinker to a commercial PEG diacrylate crosslinker, we found that the former has a cytotoxic effect on cells. Given the fact that gel-SH with PEG diacrylate seems to be highly cytocompatible and that photo-induced cleaving is a suitable tool for confining the migration of ASCs to cleaved microchannels, this setup promises to be very effective for guiding HUVEC sprouting once the cytotoxicity problem has been resolved. To this end, it would be reasonable to expose ASCs and HUVECs directly to the PEG-oNB linker and subsequently perform a 2D cell PrestoBlue cell viability assay, to confirm the observations of the present work. The next step should be to synthesize a new linker and test potential improvements regarding its cytocompatibility.

Two different hydrogels, namely gel-MA and collagen type 1, have been used for photografting experiments. The big advantage of photografting is that it can be applied to any transparent hydrogel.

While it was possible to graft inside collagen at a concentration of 3.6-4.95 mg/mL, the hydrogel did not have the necessary long-term stability to use it for cell guiding experiments. Higher concentrations were not graftable due to the increasing opaqueness. However, by adding NaOH or $NaHCO_3$ which induces physical gelation according to the collagen manufacturer, it could be possible to form a hydrogel that satisfies the requirements of structural stability and optical transparency.

The main focus of this thesis was on multi-photon induced grafting in gel-MA. Estimations based on preliminary AFM measurements indicate that the elastic modulus for 5% gel-MA ds 63 is somewhere in the single digits, which is significantly lower than previous measurements. The reason for this discrepancy remains to be addressed. Threshold tests revealed that a shorter DSSA soaking time (2 hours instead of 24 hours) as well as a higher laser scanning speed (1 000 mm/s instead of 500 mm/s) are increasing the threshold by 20 mW and 10 mW, respectively. The cytotoxicity of DSSA has been tested with a PrestoBlue metabolic activity assay, which showed that ASCs are not adversly affected whereas HUVECs are strongly affected in a concentration dependent manner. It is therefore sensible to reduce the soaking time in subsequent experiments and to determine the effect of lower concentrations on the grafting threshold.

Various parameters, namely the printing power, the design of the grafted structure, the material concentration, the cell encapsulation method, the printing parameters and the coculture ratios, have been analyzed for their potential to facilitate directional cell migration. We found the best setup to be coculture spheroids in a 1 to 1 ratio, encapsulated in 5% gel-MA with a grafting design that is simple, yet covers big parts of the spheroids' surface. Timelapse microscopy revealed that the speed in which ASCs are migrating into the grafted structures is dependent on the laser power. The major discovery of the experiments is the fact that the location of the spheroid within the hydrogel has a huge influence on the behavior of the cells. If the spheroid is in close proximity to other spheroids or the glass bottom, HUVEC migration is greatly enhanced. This is probably due to the presence of a greater number of ASCs. Especially near the glass bottom, where the proliferation and migration of ASCs seems to be strongly augmented, the number of ASCs that are migrating into the grafted channels seems to be higher, which in turn influences the direction of HUVEC migration. Even if this location dependency is accounted for, there remains a variability between samples which can be traced back to any number of variables regarding the materials or experimental processes. The next step in enhancing this setup should be the spatially controlled deposition of spheroids, which could be combined with a microfluidic chip in which other factors, such as a chemical gradient or shear force, can be applied to the sprouts.

All samples in which directional sprouting was observed were located in close proximity to the surface of the microscopy dish. It seems that the initial goal of guiding HUVEC sprouting has been achieved, although, the sample size is too small to draw a definite conclusion on directionality.

References

[1] K. T. Nguyen and J. L. West, "Photopolymerizable hydrogels for tissue engineering applications," *Biomaterials*, vol. 23, no. 22, pp. 4307–4314, 2002.

[2] F. Pampaloni, E. G. Reynaud, and E. H. K. Stelzer, "The third dimension bridges the gap between cell culture and live tissue," *Nature Reviews Molecular Cell Biology*, vol. 8, no. 10, pp. 839–845, 2007.

[3] M. Ravi, V. Paramesh, S. R. Kaviya, E. Anuradha, and F. D. P. Solomon, "3d cell culture systems: advantages and applications," *Journal of cellular physiology*, vol. 230, no. 1, pp. 16–26, 2015.

[4] A. D. Doyle, N. Carvajal, A. Jin, K. Matsumoto, and K. M. Yamada, "Local 3d matrix microenvironment regulates cell migration through spatiotemporal dynamics of contractility-dependent adhesions," *Nature Communications*, vol. 6, no. 1, p. 8720, 2015.

[5] G. Huang, F. Li, X. Zhao, Y. Ma, Y. Li, M. Lin, G. Jin, T. J. Lu, G. M. Genin, and F. Xu, "Functional and biomimetic materials for engineering of the three-dimensional cell microenvironment," *Chem. Rev.*, vol. 117, pp. 12764–12850, Oct. 2017.

[6] T. A. Ulrich, E. M. de Juan Pardo, and S. Kumar, "The mechanical rigidity of the extracellular matrix regulates the structure, motility, and proliferation of glioma cells," *Cancer research*, vol. 69, no. 10, pp. 4167–4174, 2009.

[7] J. Schrader, T. T. Gordon-Walker, R. L. Aucott, M. van Deemter, A. Quaas, S. Walsh, D. Benten, S. J. Forbes, R. G. Wells, and J. P. Iredale, "Matrix stiffness modulates proliferation, chemotherapeutic response, and dormancy in hepatocellular carcinoma cells," *Hepatology (Baltimore, Md.)*, vol. 53, no. 4, pp. 1192–1205, 2011.

[8] A. T. Alsop, J. C. Pence, D. W. Weisgerber, B. A. Harley, and R. C. Bailey, "Photopatterning of vascular endothelial growth factor within collagen-glycosaminoglycan scaffolds can induce a spatially confined response in human umbilical vein endothelial cells," *Acta Biomaterialia*, vol. 10, no. 11, pp. 4715–4722, 2014.

[9] A. J. Engler, S. Sen, H. L. Sweeney, and D. E. Discher, "Matrix elasticity directs stem cell lineage specification," *Cell*, vol. 126, no. 4, pp. 677–689, 2006.

[10] D. Karamichos, R. A. Brown, and V. Mudera, "Collagen stiffness regulates cellular contraction and matrix remodeling gene expression," *J. Biomed. Mater. Res.*, vol. 83A, pp. 887–894, Dec. 2007.

[11] R. O. Hynes, "The extracellular matrix: Not just pretty fibrils," *Science*, vol. 326, p. 1216, Nov. 2009.

[12] J. S. Park, J. S. Chu, A. D. Tsou, R. Diop, Z. Tang, A. Wang, and S. Li, "The effect of matrix stiffness on the differentiation of mesenchymal stem cells in response to TGF-β," *Biomaterials*, vol. 32, pp. 3921–3930, jun 2011.

[13] Y. Duan, X. Li, X. Zuo, T. Shen, S. Yu, L. Deng, and C. Gao, "Migration of endothelial cells and mesenchymal stem cells into hyaluronic acid hydrogels with different moduli under induction of pro-inflammatory macrophages," *Journal of Materials Chemistry B*, vol. 7, no. 36, pp. 5478–5489, 2019.

[14] Y. Hosseini, M. Agah, and S. S. Verbridge, "Endothelial cell sensing, restructuring, and invasion in collagen hydrogel structures," *Integrative Biology*, vol. 7, no. 11, pp. 1432–1441, 2015.

[15] V. L. Cross, Y. Zheng, N. Won Choi, S. S. Verbridge, B. A. Sutermaster, L. J. Bonassar, C. Fischbach, and A. D. Stroock, "Dense type i collagen matrices that support cellular remodeling and microfabrication for studies of tumor angiogenesis and vasculogenesis in vitro," *Biomaterials*, vol. 31, no. 33, pp. 8596–8607, 2010.

[16] C. M. Lo, H. B. Wang, M. Dembo, and Y. L. Wang, "Cell movement is guided by the rigidity of the substrate," *Biophysical journal*, vol. 79, no. 1, pp. 144–152, 2000.

[17] W. J. Hadden, J. L. Young, A. W. Holle, M. L. McFetridge, Y. Du Kim, P. Wijesinghe, H. Taylor-Weiner, J. H. Wen, A. R. Lee, K. Bieback, B.-N. Vo, D. D. Sampson, B. F. Kennedy, J. P. Spatz, A. J. Engler, and Y. S. Choi, "Stem cell migration and mechanotransduction on linear stiffness gradient hydrogels," *Proceedings of the National Academy of Sciences*, vol. 114, no. 22, p. 5647, 2017.

[18] L. G. Vincent, Y. S. Choi, B. Alonso-Latorre, J. C. del Álamo, and A. J. Engler, "Mesenchymal stem cell durotaxis depends on substrate stiffness gradient strength," *Biotechnology journal*, vol. 8, no. 4, pp. 472–484, 2013.

[19] M. Rajabi and S. A. Mousa, "The role of angiogenesis in cancer treatment," *Biomedicines*, vol. 5, p. 34, June 2017.

[20] M. De Palma, D. Biziato, and T. V. Petrova, "Microenvironmental regulation of tumour angiogenesis," *Nature Reviews Cancer*, vol. 17, no. 8, pp. 457–474, 2017.

[21] H. Naito, T. Iba, and N. Takakura, "Mechanisms of new blood-vessel formation and proliferative heterogeneity of endothelial cells," *Int Immunol*, vol. 32, pp. 295–305, May 2020.

[22] S. Grebenyuk and A. Ranga, "Engineering organoid vascularization," *Frontiers in Bioengineering and Biotechnology*, vol. 7, p. 39, 2019.

[23] J. Rouwkema, B. F. J. M. Koopman, C. A. V. Blitterswijk, W. J. A. Dhert, and J. Malda, "Supply of nutrients to cells in engineered tissues," *null*, vol. 26, pp. 163–178, Jan. 2009.

[24] P. Carmeliet and R. K. Jain, "Angiogenesis in cancer and other diseases," *Nature*, vol. 407, no. 6801, pp. 249–257, 2000.

[25] M. W. Laschke and M. D. Menger, "Vascularization in tissue engineering: Angiogenesis versus inosculation," 2012.

[26] E. R. Clark and E. L. Clark, "Microscopic observations on the growth of blood capillaries in the living mammal," *American Journal of Anatomy*, vol. 64, no. 2, pp. 251–301, 1939.

[27] V. Mastrullo, W. Cathery, E. Velliou, P. Madeddu, and P. Campagnolo, "Angiogenesis in tissue engineering: As nature intended?," *Frontiers in Bioengineering and Biotechnology*, vol. 8, p. 188, 2020.

[28] J. Rouwkema and A. Khademhosseini, "Vascularization and angiogenesis in tissue engineering: Beyond creating static networks," *Trends in Biotechnology*, vol. 34, no. 9, pp. 733–745, 2016.

[29] M. Nikkhah, N. Eshak, P. Zorlutuna, N. Annabi, M. Castello, K. Kim, A. Dolatshahi-Pirouz, F. Edalat, H. Bae, Y. Yang, and A. Khademhosseini, "Directed endothelial cell morphogenesis in micropatterned gelatin methacrylate hydrogels," *Biomaterials*, vol. 33, no. 35, pp. 9009–9018, 2012.

[30] W. Jia, P. S. Gungor-Ozkerim, Y. S. Zhang, K. Yue, K. Zhu, W. Liu, Q. Pi, B. Byambaa, M. R. Dokmeci, S. R. Shin, and A. Khademhosseini, "Direct 3d bioprinting of

perfusable vascular constructs using a blend bioink," *Biomaterials*, vol. 106, pp. 58–68, 2016.

[31] B. Sun, X.-J. Jiang, S. Zhang, J.-C. Zhang, Y.-F. Li, Q.-Z. You, and Y.-Z. Long, "Electrospun anisotropic architectures and porous structures for tissue engineering," *Journal of Materials Chemistry B*, vol. 3, no. 27, pp. 5389–5410, 2015.

[32] Y. Abe, M. Watanabe, S. Chung, R. D. Kamm, K. Tanishita, and R. Sudo, "Balance of interstitial flow magnitude and vascular endothelial growth factor concentration modulates three-dimensional microvascular network formation," *APL bioengineering*, vol. 3, pp. 036102–036102, July 2019.

[33] M. S. Hahn, J. S. Miller, and J. L. West, "Three-dimensional biochemical and biomechanical patterning of hydrogels for guiding cell behavior," *Advanced Materials*, vol. 18, no. 20, pp. 2679–2684, 2006.

[34] A. Fritschen and A. Blaeser, "Biosynthetic, biomimetic, and self-assembled vascularized organ-on-a-chip systems," *Biomaterials*, p. 120556, nov 2020.

[35] S. Dikici, F. Claeyssens, and S. MacNeil, "Bioengineering vascular networks to study angiogenesis and vascularization of physiologically relevant tissue models in vitro," *ACS Biomaterials Science & Engineering*, vol. 6, pp. 3513–3528, apr 2020.

[36] Y. Zheng, J. Chen, and J. A. López, "Flow-driven assembly of VWF fibres and webs in in vitro microvessels," *Nature Communications*, vol. 6, jul 2015.

[37] Y. Zheng, J. Chen, M. Craven, N. W. Choi, S. Totorica, A. Diaz-Santana, P. Kermani, B. Hempstead, C. Fischbach-Teschl, J. A. Lopez, and A. D. Stroock, "In vitro microvessels for the study of angiogenesis and thrombosis," *Proceedings of the National Academy of Sciences*, vol. 109, pp. 9342–9347, may 2012.

[38] P. A. Iaizzo, "General features of the cardiovascular system," in *Handbook of Cardiac Anatomy, Physiology, and Devices* (P. A. Iaizzo, ed.), pp. 3–12, Cham: Springer International Publishing, 2015.

[39] A. K. Miri, A. Khalilpour, B. Cecen, S. Maharjan, S. R. Shin, and A. Khademhosseini, "Multiscale bioprinting of vascularized models," *Biomaterials*, vol. 198, pp. 204–216, 2019.

[40] A. McCormack, C. B. Highley, N. R. Leslie, and F. P. Melchels, "3d printing in suspension baths: Keeping the promises of bioprinting afloat," *Trends in Biotechnology*, vol. 38, pp. 584–593, jun 2020.

[41] M. Yanez, J. Rincon, A. Dones, C. De Maria, R. Gonzales, and T. Boland, "In vivo assessment of printed microvasculature in a bilayer skin graft to treat full-thickness wounds," *Tissue Engineering Part A*, vol. 21, pp. 224–233, July 2014.

[42] J. S. Miller, K. R. Stevens, M. T. Yang, B. M. Baker, D.-H. T. Nguyen, D. M. Cohen, E. Toro, A. A. Chen, P. A. Galie, X. Yu, R. Chaturvedi, S. N. Bhatia, and C. S. Chen, "Rapid casting of patterned vascular networks for perfusable engineered three-dimensional tissues," *Nature Materials*, vol. 11, no. 9, pp. 768–774, 2012.

[43] O. Kérourédan, J.-M. Bourget, M. Rémy, S. Crauste-Manciet, J. Kalisky, S. Catros, N. B. Thébaud, and R. Devillard, "Micropatterning of endothelial cells to create a capillary-like network with defined architecture by laser-assisted bioprinting," *Journal of Materials Science: Materials in Medicine*, vol. 30, feb 2019.

[44] W. Zhu, X. Qu, J. Zhu, X. Ma, S. Patel, J. Liu, P. Wang, C. S. E. Lai, M. Gou, Y. Xu, K. Zhang, and S. Chen, "Direct 3d bioprinting of prevascularized tissue constructs with complex microarchitecture," *Biomaterials*, vol. 124, pp. 106–115, apr 2017.

[45] A. Ovsianikov, A. Deiwick, S. Van Vlierberghe, P. Dubruel, L. Möller, G. Dräger, and B. Chichkov, "Laser fabrication of three-dimensional cad scaffolds from photosensitive gelatin for applications in tissue engineering," *Biomacromolecules*, vol. 12, pp. 851–858, Apr. 2011.

[46] W. Meyer, S. Engelhardt, E. Novosel, B. Elling, M. Wegener, and H. Krüger, "Soft polymers for building up small and smallest blood supplying systems by stereolithography," *Journal of Functional Biomaterials*, vol. 3, pp. 257–268, mar 2012.

[47] J. C. Culver, J. C. Hoffmann, R. A. Poché, J. H. Slater, J. L. West, and M. E. Dickinson, "Three-dimensional biomimetic patterning in hydrogels to guide cellular organization," *Adv. Mater.*, vol. 24, pp. 2344–2348, May 2012.

[48] A. Farrukh, J. I. Paez, and A. del Campo, "4d biomaterials for light-guided angiogenesis," *Adv. Funct. Mater.*, vol. 29, p. 1807734, Feb. 2019.

[49] C. K. Arakawa, B. A. Badeau, Y. Zheng, and C. A. DeForest, "Multicellular vascularized engineered tissues through user-programmable biomaterial photodegradation," *Adv. Mater.*, vol. 29, p. 1703156, Oct. 2017.

[50] Z. Xiong, H. Li, P. Kunwar, Y. Zhu, R. Ramos, S. Mcloughlin, T. Winston, Z. Ma, and P. Soman, "Femtosecond laser induced densification within cell-laden hydrogels results in cellular alignment," *Biofabrication*, vol. 11, no. 3, p. 035005, 2019.

[51] N. Brandenberg and M. P. Lutolf, "In situ patterning of microfluidic networks in 3d cell-laden hydrogels," *Adv. Mater.*, vol. 28, pp. 7450–7456, Sept. 2016.

[52] O. Sarig-Nadir, N. Livnat, R. Zajdman, S. Shoham, and D. Seliktar, "Laser photoablation of guidance microchannels into hydrogels directs cell growth in three dimensions," *Biophysical journal*, vol. 96, no. 11, pp. 4743–4752, 2009.

[53] M. Jergitsch, "Investigation of vascularization strategies for 3d tissue engineering," *M.S. thesis, FH Technikum Wien*, p. 74, July 2018.

[54] R. P. Mecham, "Overview of extracellular matrix," *Current Protocols in Cell Biology*, vol. 57, pp. 10.1.1–10.1.16, Dec. 2012.

[55] P. Lu, K. Takai, V. M. Weaver, and Z. Werb, "Extracellular matrix degradation and remodeling in development and disease," *Cold Spring Harbor perspectives in biology*, vol. 3, p. a005058, Dec. 2011.

[56] C. Frantz, K. M. Stewart, and V. M. Weaver, "The extracellular matrix at a glance," *J. Cell Sci.*, vol. 123, p. 4195, Dec. 2010.

[57] A. D. Theocharis, S. S. Skandalis, C. Gialeli, and N. K. Karamanos, "Extracellular matrix structure," *Advanced Drug Delivery Reviews*, vol. 97, pp. 4–27, 2016.

[58] B. Yue, "Biology of the extracellular matrix: an overview," *Journal of glaucoma*, vol. 23, no. 25275899, pp. S20–S23, 2014.

[59] Y.-H. Lin, T.-M. Pan, M.-H. Wu, and M. Moo-Young, "5.12 - microfluidic technology and its biological applications," in *Comprehensive Biotechnology (Second Edition)*, pp. 141–157, Burlington: Academic Press, 2011.

[60] S. A. Langhans, "Three-dimensional in vitro cell culture models in drug discovery and drug repositioning," *Frontiers in Pharmacology*, vol. 9, p. 6, 2018.

[61] D. M. Dean, A. P. Napolitano, J. Youssef, and J. R. Morgan, "Rods, tori, and honeycombs: the directed self-assembly of microtissues with prescribed microscale geometries," *The FASEB Journal*, vol. 21, pp. 4005–4012, Dec. 2007.

[62] N.-E. Ryu, S.-H. Lee, and H. Park, "Spheroid culture system methods and applications for mesenchymal stem cells," *Cells*, vol. 8, p. 1620, Dec. 2019.

[63] K. Duval, H. Grover, L.-H. Han, Y. Mou, A. F. Pegoraro, J. Fredberg, and Z. Chen, "Modeling physiological events in 2d vs. 3d cell culture," *Physiology*, vol. 32, pp. 266–277, June 2017.

[64] E. K. F. Yim and K. W. Leong, "Proliferation and differentiation of human embryonic germ cell derivatives in bioactive polymeric fibrous scaffold," *null*, vol. 16, pp. 1193–1217, Jan. 2005.

[65] S. Levenberg, N. F. Huang, E. Lavik, A. B. Rogers, J. Itskovitz-Eldor, and R. Langer, "Differentiation of human embryonic stem cells on three-dimensional polymer scaffolds," *Proceedings of the National Academy of Sciences of the United States of America*, vol. 100, pp. 12741–12746, Oct. 2003.

[66] G. A. Silva, C. Czeisler, K. L. Niece, E. Beniash, D. A. Harrington, J. A. Kessler, and S. I. Stupp, "Selective differentiation of neural progenitor cells by high-epitope density nanofibers," *Science*, vol. 303, p. 1352, Feb. 2004.

[67] S. S. Rao, J. Dejesus, A. R. Short, J. J. Otero, A. Sarkar, and J. O. Winter, "Glioblastoma behaviors in three-dimensional collagen-hyaluronan composite hydrogels," *ACS applied materials & interfaces*, vol. 5, pp. 9276–9284, Oct. 2013.

[68] J. Yang, J. Richards, P. Bowman, R. Guzman, J. Enami, K. McCormick, S. Hamamoto, D. Pitelka, and S. Nandi, "Sustained growth and three-dimensional organization of primary mammary tumor epithelial cells embedded in collagen gels," *Proceedings of the National Academy of Sciences of the United States of America*, vol. 76, pp. 3401–3405, July 1979.

[69] M. W. Tibbitt and K. S. Anseth, "Hydrogels as extracellular matrix mimics for 3d cell culture," *Biotechnology and bioengineering*, vol. 103, pp. 655–663, July 2009.

[70] L. W. Dunne, Z. Huang, W. Meng, X. Fan, N. Zhang, Q. Zhang, and Z. An, "Human decellularized adipose tissue scaffold as a model for breast cancer cell growth and drug treatments," *Biomaterials*, vol. 35, no. 18, pp. 4940–4949, 2014.

[71] M. Mirbagheri, V. Adibnia, B. R. Hughes, S. D. Waldman, X. Banquy, and D. K. Hwang, "Advanced cell culture platforms: a growing quest for emulating natural tissues," *Mater. Horiz.*, vol. 6, no. 1, pp. 45–71, 2019.

[72] H.-D. Kim and S. R. Peyton, "Bio-inspired materials for parsing matrix physicochemical control of cell migration: A review," *Int Bio (Cam)*, vol. 4, pp. 37–52, Jan. 2012.

[73] M. Whang and J. Kim, "Synthetic hydrogels with stiffness gradients for durotaxis study and tissue engineering scaffolds," *Tissue Engineering and Regenerative Medicine*, vol. 13, no. 2, pp. 126–139, 2016.

[74] M. V. Turturro and G. Papavasiliou, "Generation of mechanical and biofunctional gradients in peg diacrylate hydrogels by perfusion-based frontal photopolymerization," *null*, vol. 23, pp. 917–939, Jan. 2012.

[75] J. He, Y. Du, J. L. Villa-Uribe, C. Hwang, D. Li, and A. Khademhosseini, "Rapid generation of biologically relevant hydrogels containing long-range chemical gradients," *Adv. Funct. Mater.*, vol. 20, pp. 131–137, Jan. 2010.

[76] J. Y. Wong, A. Velasco, P. Rajagopalan, and Q. Pham, "Directed movement of vascular smooth muscle cells on gradient-compliant hydrogels," *Langmuir*, vol. 19, pp. 1908–1913, Mar. 2003.

[77] Y. K. Cheung, E. U. Azeloglu, D. A. Shiovitz, K. D. Costa, D. Seliktar, and S. K. Sia, "Microscale control of stiffness in a cell-adhesive substrate using microfluidics-based lithography," *Angewandte Chemie International Edition*, vol. 48, pp. 7188–7192, Sept. 2009.

[78] P.-h. G. Chao, S.-C. Sheng, and W.-R. Chang, "Micro-composite substrates for the study of cell-matrix mechanical interactions," *Journal of the Mechanical Behavior of Biomedical Materials*, vol. 38, pp. 232–241, 2014.

[79] S. Kidoaki and T. Matsuda, "Microelastic gradient gelatinous gels to induce cellular mechanotaxis," *Journal of Biotechnology*, vol. 133, no. 2, pp. 225–230, 2008.

[80] J. R. Tse and A. J. Engler, "Stiffness gradients mimicking in vivo tissue variation regulate mesenchymal stem cell fate," *PLOS ONE*, vol. 6, p. e15978, Jan. 2011.

[81] M. Raab, J. Swift, P. C. D. P. Dingal, P. Shah, J.-W. Shin, and D. E. Discher, "Crawling from soft to stiff matrix polarizes the cytoskeleton and phosphoregulates myosin-ii heavy chain," *J Cell Biol*, vol. 199, pp. 669–683, Nov. 2012.

[82] K. A. Mosiewicz, L. Kolb, A. J. van der Vlies, and M. P. Lutolf, "Microscale patterning of hydrogel stiffness through light-triggered uncaging of thiols," *Biomater. Sci.*, vol. 2, no. 11, pp. 1640–1651, 2014.

[83] Y. J. He, D. A. Young, M. Mededovic, K. Li, C. Li, K. Tichauer, D. Venerus, and G. Papavasiliou, "Protease-sensitive hydrogel biomaterials with tunable modulus and adhesion ligand gradients for 3d vascular sprouting," *Biomacromolecules*, vol. 19, no. 11, pp. 4168–4181, 2018.

[84] J. E. Samorezov, C. M. Morlock, and E. Alsberg, "Dual ionic and photo-crosslinked alginate hydrogels for micropatterned spatial control of material properties and cell behavior," *Bioconjugate Chem.*, vol. 26, pp. 1339–1347, July 2015.

[85] C. Monge, N. Saha, T. Boudou, C. Pózos-Vásquez, V. Dulong, K. Glinel, and C. Picart, "Rigidity-patterned polyelectrolyte films to control myoblast cell adhesion and spatial organization," *Adv. Funct. Mater.*, vol. 23, pp. 3432–3442, July 2013.

[86] E. Boulpaep, *Chapter 19 Arteries and Veins*, pp. 467–482. Philadelphia, PA: Elsevier, 2017.

[87] D. A. Hartmann, R. G. Underly, R. I. Grant, A. N. Watson, V. Lindner, and A. Y. Shih, "Pericyte structure and distribution in the cerebral cortex revealed by high-resolution imaging of transgenic mice," *Neurophotonics*, vol. 2, pp. 1–13, May 2015.

[88] D. C. Darland and P. A. D'Amore, "Blood vessel maturation: vascular development comes of age," *J Clin Invest*, vol. 103, pp. 157–158, Jan. 1999.

[89] J. M. Rhodes and M. Simons, "The extracellular matrix and blood vessel formation: not just a scaffold," *Journal of cellular and molecular medicine*, vol. 11, no. 17488472, pp. 176–205, 2007.

[90] C. Sanina, O. L. Bockeria, K. A. Wiley, J. E. Feig, C. Sanina, G. D. Dangas, P. Faries, J. M. Wiley, P. Krishnan, and I. Conde, "Vascular biology," 2018.

[91] J. Eble and S. Niland, "The extracellular matrix of blood vessels," *Current Pharmaceutical Design*, vol. 15, pp. 1385–1400, apr 2009.

[92] Y.-C. Fung, "Mechanical properties and active remodeling of blood vessels," in *Biomechanics: Mechanical Properties of Living Tissues*, pp. 321–391, New York, NY: Springer New York, 1993.

[93] J. A. G. Rhodin, "Architecture of the vessel wall," pp. 1–31.

[94] G. Bergers and S. Song, "The role of pericytes in blood-vessel formation and maintenance," *Neuro-oncology*, vol. 7, pp. 452–464, Oct. 2005.

[95] M. Potente and T. Mäkinen, "Vascular heterogeneity and specialization in development and disease," *Nature Reviews Molecular Cell Biology*, vol. 18, no. 8, pp. 477–494, 2017.

[96] C. Viallard and B. Larrivée, "Tumor angiogenesis and vascular normalization: alternative therapeutic targets," *Angiogenesis*, vol. 20, no. 4, pp. 409–426, 2017.

[97] S. Ziyad and M. L. Iruela-Arispe, "Molecular mechanisms of tumor angiogenesis," *Genes & Cancer*, vol. 2, pp. 1085–1096, Dec. 2011.

[98] S. Negri, P. Faris, V. Rosti, M. R. Antognazza, F. Lodola, and F. Moccia, "Endothelial trpv1 as an emerging molecular target to promote therapeutic angiogenesis," *Cells*, vol. 9, p. 1341, May 2020.

[99] V. Djonov, O. Baum, and P. H. Burri, "Vascular remodeling by intussusceptive angiogenesis," *Cell and Tissue Research*, vol. 314, no. 1, pp. 107–117, 2003.

[100] S. Patan, "Vasculogenesis and angiogenesis," in *Angiogenesis in Brain Tumors* (M. Kirsch and P. M. Black, eds.), pp. 3–32, Boston, MA: Springer US, 2004.

[101] W. Risau and I. Flamme, "Vasculogenesis," *Annu. Rev. Cell Dev. Biol.*, vol. 11, pp. 73–91, Nov. 1995.

[102] W. Risau, H. Sariola, H. G. Zerwes, J. Sasse, P. Ekblom, R. Kemler, and T. Doetschman, "Vasculogenesis and angiogenesis in embryonic-stem-cell-derived embryoid bodies," *Development*, vol. 102, p. 471, Mar. 1988.

[103] L. Pardanaud, C. Altmann, P. Kitos, F. Dieterlen-Lievre, and C. A. Buck, "Vasculogenesis in the early quail blastodisc as studied with a monoclonal antibody recognizing endothelial cells," *Development*, vol. 100, p. 339, June 1987.

[104] F. P. Reagan, "Vascularization phenomena in fragments of embryonic bodies completely isolated from yolk-sac blastoderm," *Anat. Rec.*, vol. 9, pp. 329–341, Apr. 1915.

[105] J. Tongers, J. G. Roncalli, and D. W. Losordo, "Role of endothelial progenitor cells during ischemia-induced vasculogenesis and collateral formation," *Microvascular research*, vol. 79, pp. 200–206, May 2010.

[106] T. Asahara, H. Masuda, T. Takahashi, C. Kalka, C. Pastore, M. Silver, M. Kearne, M. Magner, and J. M. Isner, "Bone marrow origin of endothelial progenitor cells responsible for postnatal vasculogenesis in physiological and pathological neovascularization," *Circulation Research*, vol. 85, no. 3, pp. 221–228, 1999.

[107] T. Asahara, T. Murohara, A. Sullivan, M. Silver, R. van der Zee, T. Li, B. Witzenbichler, G. Schatteman, and J. M. Isner, "Isolation of putative progenitor endothelial cells for angiogenesis," *Science*, vol. 275, p. 964, Feb. 1997.

[108] S. Patel-Hett and P. A. D'Amore, "Signal transduction in vasculogenesis and developmental angiogenesis," *The International journal of developmental biology*, vol. 55, no. 21732275, pp. 353–363, 2011.

[109] J. Folkman, "Tumor angiogenesis: Therapeutic implications," *N Engl J Med*, vol. 285, pp. 1182–1186, Nov. 1971.

[110] J. Folkman, "Angiogenesis," in *Biology of Endothelial Cells* (E. A. Jaffe, ed.), pp. 412–428, Boston, MA: Springer US, 1984.

[111] W. Risau, "Mechanisms of angiogenesis," *Nature*, vol. 386, no. 6626, pp. 671–674, 1997.

[112] D. Kolte, J. A. McClung, and W. S. Aronow, "Chapter 6 vasculogenesis and angiogenesis," in *Translational Research in Coronary Artery Disease*, no. pub.1038508301, pp. 49–65, 2016.

[113] D. H. Ausprunk and J. Folkman, "Migration and proliferation of endothelial cells in preformed and newly formed blood vessels during tumor angiogenesis," *Microvascular Research*, vol. 14, no. 1, pp. 53–65, 1977.

[114] R. Blanco and H. Gerhardt, "Vegf and notch in tip and stalk cell selection," *Cold Spring Harbor perspectives in medicine*, vol. 3, pp. a006569–a006569, Jan. 2013.

[115] U. R. Michaelis, "Mechanisms of endothelial cell migration," *Cellular and Molecular Life Sciences*, vol. 71, no. 21, pp. 4131–4148, 2014.

[116] A. Lenard, E. Ellertsdottir, L. Herwig, A. Krudewig, L. Sauteur, H.-G. Belting, and M. Affolter, "In vivo analysis reveals a highly stereotypic morphogenetic pathway of vascular anastomosis," *Developmental Cell*, vol. 25, no. 5, pp. 492–506, 2013.

[117] M. L. Iruela-Arispe and G. E. Davis, "Cellular and molecular mechanisms of vascular lumen formation," *Developmental Cell*, vol. 16, no. 2, pp. 222–231, 2009.

[118] R. K. Jain, "Molecular regulation of vessel maturation," *Nature Medicine*, vol. 9, no. 6, pp. 685–693, 2003.

[119] J. H. Caduff, L. C. Fischer, and P. H. Burri, "Scanning electron microscope study of the developing microvasculature in the postnatal rat lung," *Anat. Rec.*, vol. 216, pp. 154–164, Oct. 1986.

[120] P. H. Burri and M. R. Tarek, "A novel mechanism of capillary growth in the rat pulmonary microcirculation," *Anat. Rec.*, vol. 228, pp. 35–45, Sept. 1990.

[121] D. Ribatti and V. Djonov, "Intussusceptive microvascular growth in tumors," *Cancer Letters*, vol. 316, no. 2, pp. 126–131, 2012.

[122] V. G. Djonov, H. Kurz, and P. H. Burri, "Optimality in the developing vascular system: Branching remodeling by means of intussusception as an efficient adaptation mechanism," *Dev. Dyn.*, vol. 224, pp. 391–402, Aug. 2002.

[123] V. Djonov, M. Schmid, A. Tschanz S., and H. Burri P., "Intussusceptive angiogenesis," *Circulation Research*, vol. 86, pp. 286–292, Feb. 2000.

[124] G. F. Muschler, C. Nakamoto, and L. G. Griffith, "Engineering principles of clinical cell-based tissue engineering," *JBJS*, vol. 86, no. 7, 2004.

[125] R. Langer and J. P. Vacanti, "Tissue engineering," *Science*, vol. 260, p. 920, May 1993.

[126] G. C. Gurtner, M. J. Callaghan, and M. T. Longaker, "Progress and potential for regenerative medicine," *Annu. Rev. Med.*, vol. 58, pp. 299–312, Jan. 2007.

[127] P. K. Chandra, S. Soker, A. Atala, R. Lanza, R. Langer, J. P. Vacanti, and A. Atala, "Chapter 1 - tissue engineering: current status and future perspectives," in *Principles of Tissue Engineering (Fifth Edition)*, pp. 1–35, Academic Press, 2020.

[128] G. Matsumura, N. Nitta, S. Matsuda, Y. Sakamoto, N. Isayama, K. Yamazaki, and Y. Ikada, "Long-term results of cell-free biodegradable scaffolds for in situ tissue-engineering vasculature: In a canine inferior vena cava model," *PLOS ONE*, vol. 7, p. e35760, Apr. 2012.

[129] L. G. Griffith and G. Naughton, "Tissue engineering–current challenges and expanding opportunities," *Science*, vol. 295, p. 1009, Feb. 2002.

[130] T. Hoffman, A. Khademhosseini, and R. Langer, "Chasing the paradigm: Clinical translation of 25 years of tissue engineering," *Tissue Engineering Part A*, vol. 25, pp. 679–687, Feb. 2019.

[131] K. Dzobo, N. E. Thomford, D. A. Senthebane, H. Shipanga, A. Rowe, C. Dandara, M. Pillay, and K. S. C. M. Motaung, "Advances in regenerative medicine and tissue engineering: Innovation and transformation of medicine," *Stem Cells International*, vol. 2018, p. 2495848, 2018.

[132] G. Zhou, H. Jiang, Z. Yin, Y. Liu, Q. Zhang, C. Zhang, B. Pan, J. Zhou, X. Zhou, H. Sun, D. Li, A. He, Z. Zhang, W. Zhang, W. Liu, and Y. Cao, "In vitro regeneration of patient-specific ear-shaped cartilage and its first clinical application for auricular reconstruction," *EBioMedicine*, vol. 28, pp. 287–302, 2018.

[133] A. Atala, S. B. Bauer, S. Soker, J. J. Yoo, and A. B. Retik, "Tissue-engineered autologous bladders for patients needing cystoplasty," *The Lancet*, vol. 367, no. 9518, pp. 1241–1246, 2006.

[134] L. A. Lavery, J. Fulmer, K. A. Shebetka, M. Regulski, D. Vayser, D. Fried, H. Kashefsky, T. M. Owings, J. Nadarajah, and T. G. D. F. U. S. Group, "The efficacy and safety of grafix® for the treatment of chronic diabetic foot ulcers: results of a multi-centre, controlled, randomised, blinded, clinical trial," *Int Wound J*, vol. 11, pp. 554–560, Oct. 2014.

[135] P. Behrens, T. Bitter, B. Kurz, and M. Russlies, "Matrix-associated autologous chondrocyte transplantation/implantation (mact/maci)–5-year follow-up," *The Knee*, vol. 13, no. 3, pp. 194–202, 2006.

[136] J. Gille, P. Behrens, A. P. Schulz, R. Oheim, and B. Kienast, "Matrix-associated autologous chondrocyte implantation: A clinical follow-up at 15 years," *Cartilage*, vol. 7, pp. 309–315, Oct. 2016.

[137] F. Colombo, G. Sampogna, G. Cocozza, S. Y. Guraya, and A. Forgione, "Regenerative medicine: Clinical applications and future perspectives," *Journal of Microscopy and Ultrastructure*, vol. 5, no. 1, pp. 1–8, 2017.

[138] Y. Liu, G. Zhou, and Y. Cao, "Recent progress in cartilage tissue engineering–our experience and future directions," *Engineering*, vol. 3, no. 1, pp. 28–35, 2017.

[139] K. Ghosal, P. Sarkar, R. Saha, S. Ghosh, and K. Sarkar, "Advances in tissue engineering and regeneration," in *Racing for the Surface: Antimicrobial and Interface Tissue Engineering* (B. Li, T. F. Moriarty, T. Webster, and M. Xing, eds.), pp. 577–646, Cham: Springer International Publishing, 2020.

[140] A. Khademhosseini and R. Langer, "A decade of progress in tissue engineering," *Nature Protocols*, vol. 11, no. 10, pp. 1775–1781, 2016.

[141] A. Shafiee and A. Atala, "Tissue engineering: Toward a new era of medicine," *Annu. Rev. Med.*, vol. 68, pp. 29–40, Jan. 2017.

[142] R. Langer and J. Vacanti, "Advances in tissue engineering," *Journal of pediatric surgery*, vol. 51, pp. 8–12, Jan. 2016.

[143] P. M. Baptista, M. M. Siddiqui, G. Lozier, S. R. Rodriguez, A. Atala, and S. Soker, "The use of whole organ decellularization for the generation of a vascularized liver organoid," *Hepatology*, vol. 53, pp. 604–617, Feb. 2011.

[144] J. F. Vander, C. M. Morgan, and H. Schatz, "Growth rate of subretinal neovascularization in age-related macular degeneration," *Ophthalmology*, vol. 96, no. 9, pp. 1422–1429, 1989.

[145] O. O. Akintewe, E. G. Roberts, N.-G. Rim, M. A. H. Ferguson, and J. Y. Wong, "Design approaches to myocardial and vascular tissue engineering," *Annu. Rev. Biomed. Eng.*, vol. 19, pp. 389–414, June 2017.

[146] F. Couet, N. Rajan, and D. Mantovani, "Macromolecular biomaterials for scaffold-based vascular tissue engineering," *Macromol. Biosci.*, vol. 7, pp. 701–718, May 2007.

[147] C. Vyas, R. Pereira, B. Huang, F. Liu, W. Wang, and P. Bartolo, "Engineering the vasculature with additive manufacturing," *Current Opinion in Biomedical Engineering*, vol. 2, pp. 1–13, 2017.

[148] I. Kocherova, A. Bryja, P. Mozdziak, A. Angelova Volponi, M. Dyszkiewicz-Konwińska, H. Piotrowska-Kempisty, P. Antosik, D. Bukowska, M. Bruska, D. Iżycki, M. Zabel, M. Nowicki, and B. Kempisty, "Human umbilical vein endothelial cells (huvecs) co-culture with osteogenic cells: From molecular communication to engineering prevascularised bone grafts," *Journal of clinical medicine*, vol. 8, p. 1602, Oct. 2019.

[149] J. V. Serbo and S. Gerecht, "Vascular tissue engineering: biodegradable scaffold platforms to promote angiogenesis," *Stem Cell Research & Therapy*, vol. 4, no. 1, p. 8, 2013.

[150] S. Hauser, F. Jung, and J. Pietzsch, "Human endothelial cell models in biomaterial research," *Trends in Biotechnology*, vol. 35, no. 3, pp. 265–277, 2017.

[151] M. Sweeney and G. Foldes, "It takes two: Endothelial-perivascular cell cross-talk in vascular development and disease," *Frontiers in Cardiovascular Medicine*, vol. 5, p. 154, 2018.

[152] N. Koike, D. Fukumura, O. Gralla, P. Au, J. S. Schechner, and R. K. Jain, "Creation of long-lasting blood vessels," *Nature*, vol. 428, no. 6979, pp. 138–139, 2004.

[153] S. Pati, A. Y. Khakoo, J. Zhao, F. Jimenez, M. H. Gerber, M. Harting, J. B. Redell, R. Grill, Y. Matsuo, S. Guha, C. S. Cox, M. S. Reitz, J. B. Holcomb, and P. K. Dash, "Human mesenchymal stem cells inhibit vascular permeability by modulating vascular endothelial cadherin/β-catenin signaling," *Stem cells and development*, vol. 20, pp. 89–101, Jan. 2011.

[154] J. M. Melero-Martin, M. E. De Obaldia, S.-Y. Kang, Z. A. Khan, L. Yuan, P. Oettgen, and J. Bischoff, "Engineering robust and functional vascular networks in vivo with human adult and cord blood-derived progenitor cells," *Circulation research*, vol. 103, pp. 194–202, July 2008.

[155] F. Verseijden, S. J. Posthumus-van Sluijs, P. Pavljasevic, S. O. P. Hofer, G. J. V. M. van Osch, and E. Farrell, "Adult human bone marrow- and adipose tissue-derived stromal cells support the formation of prevascular-like structures from endothelial cells in vitro," *Tissue Engineering Part A*, vol. 16, pp. 101–114, July 2009.

[156] S. Rohringer, P. Hofbauer, K. H. Schneider, A.-M. Husa, G. Feichtinger, A. Peterbauer-Scherb, H. Redl, and W. Holnthoner, "Mechanisms of vasculogenesis in 3d fibrin matrices mediated by the interaction of adipose-derived stem cells and endothelial cells," *Angiogenesis*, vol. 17, no. 4, pp. 921–933, 2014.

[157] S. J. Grainger and A. J. Putnam, "Assessing the permeability of engineered capillary networks in a 3d culture," *PLOS ONE*, vol. 6, p. e22086, July 2011.

[158] S. Merfeld-Clauss, N. Gollahalli, K. L. March, and D. O. Traktuev, "Adipose tissue progenitor cells directly interact with endothelial cells to induce vascular network formation," *Tissue engineering. Part A*, vol. 16, pp. 2953–2966, Sept. 2010.

[159] S. Kachgal and A. J. Putnam, "Mesenchymal stem cells from adipose and bone marrow promote angiogenesis via distinct cytokine and protease expression mechanisms," *Angiogenesis*, vol. 14, no. 1, pp. 47–59, 2011.

[160] W. Holnthoner, K. Hohenegger, A.-M. Husa, S. Muehleder, A. Meinl, A. Peterbauer-Scherb, and H. Redl, "Adipose-derived stem cells induce vascular tube formation of outgrowth endothelial cells in a fibrin matrix," *J Tissue Eng Regen Med*, vol. 9, pp. 127–136, Feb. 2015.

[161] M. Göppert-Mayer, "Über elementarakte mit zwei quantensprüngen," *Ann. Phys.*, vol. 401, pp. 273–294, Jan. 1931.

[162] W. Kaiser and C. G. B. Garrett, "Two-photon excitation in caf_2: eu^{2+}," *PRL*, vol. 7, pp. 229–231, Sept. 1961.

[163] J. Fourkas and N. A. Vainos, "5 - multiphoton lithography, processing and fabrication of photonic structures," in *Laser Growth and Processing of Photonic Devices*, pp. 139–161, Woodhead Publishing, 2012.

[164] P. Gruber, "Development of a novel wavelength-tunable high-speed 2-photon lithography setup," *Ph.D. dissertation, TU Wien*, p. 142, July 2018.

[165] S. Jaumotte-Thelen, I. Dozot-Dupont, J. Marchand-Brynaert, and Y.-J. Schneider, "Covalent grafting of fibronectin and asialofetuin at surface of poly(ethylene terephthalate) track-etched membranes improves adhesion but not differentiation of rat hepatocytes," *J. Biomed. Mater. Res.*, vol. 32, pp. 569–582, Dec. 1996.

[166] G. Ashkenasy, D. Cahen, R. Cohen, A. Shanzer, and A. Vilan, "Molecular engineering of semiconductor surfaces and devices," *Acc. Chem. Res.*, vol. 35, pp. 121–128, Feb. 2002.

[167] Z. Li, A. Ajami, E. Stankevičius, W. Husinsky, G. Račiukaitis, J. Stampfl, R. Liska, and A. Ovsianikov, "3d photografting with aromatic azides: A comparison between three-photon and two-photon case," *Optical Materials*, vol. 35, no. 10, pp. 1846–1851, 2013.

[168] M. A. Holden and P. S. Cremer, "Light activated patterning of dye-labeled molecules on surfaces," *J. Am. Chem. Soc.*, vol. 125, pp. 8074–8075, July 2003.

[169] A. Ovsianikov, Z. Li, J. Torgersen, J. Stampfl, and R. Liska, "Selective functionalization of 3d matrices via multiphoton grafting and subsequent click chemistry," *Adv. Funct. Mater.*, vol. 22, pp. 3429–3433, Aug. 2012.

[170] Y. Luo and M. S. Shoichet, "A photolabile hydrogel for guided three-dimensional cell growth and migration," *Nature Materials*, vol. 3, no. 4, pp. 249–253, 2004.

[171] A. M. Kloxin, A. M. Kasko, C. N. Salinas, and K. S. Anseth, "Photodegradable hydrogels for dynamic tuning of physical and chemical properties," *Science*, vol. 324, p. 59, Apr. 2009.

[172] M. Lunzer, L. Shi, O. G. Andriotis, P. Gruber, M. Markovic, P. J. Thurner, D. Ossipov, R. Liska, and A. Ovsianikov, "A modular approach to sensitized two-photon patterning of photodegradable hydrogels," *Angew. Chem. Int. Ed.*, vol. 57, pp. 15122–15127, Nov. 2018.

[173] H. Zhao, E. S. Sterner, E. B. Coughlin, and P. Theato, "o-nitrobenzyl alcohol derivatives: Opportunities in polymer and materials science," *Macromolecules*, vol. 45, pp. 1723–1736, Feb. 2012.

[174] M. A. Azagarsamy, D. D. McKinnon, D. L. Alge, and K. S. Anseth, "Coumarin-based photodegradable hydrogel: Design, synthesis, gelation, and degradation kinetics," *ACS Macro Lett.*, vol. 3, pp. 515–519, June 2014.

[175] W. Shen, J. Zheng, Z. Zhou, and D. Zhang, "Approaches for the synthesis of o-nitrobenzyl and coumarin linkers for use in photocleavable biomaterials and bioconjugates and their biomedical applications," *Acta Biomaterialia*, vol. 115, pp. 75–91, 2020.

[176] B. Judkewitz, A. Roth, and M. Häusser, "Dendritic enlightenment: Using patterned two-photon uncaging to reveal the secrets of the brain's smallest dendrites," *Neuron*, vol. 50, pp. 180–183, Apr. 2006.

[177] R. G. Wylie and M. S. Shoichet, "Two-photon micropatterning of amines within an agarose hydrogel," *J. Mater. Chem.*, vol. 18, no. 23, pp. 2716–2721, 2008.

[178] C. D. Spicer, "Hydrogel scaffolds for tissue engineering: the importance of polymer choice," *Polym. Chem.*, vol. 11, no. 2, pp. 184–219, 2020.

[179] K. Y. Lee and D. J. Mooney, "Hydrogels for tissue engineering," *Chemical Reviews*, vol. 101, no. 7, pp. 1869–1880, 2001.

[180] J. Van Hoorick, L. Tytgat, A. Dobos, H. Ottevaere, J. Van Erps, H. Thienpont, A. Ovsianikov, P. Dubruel, and S. Van Vlierberghe, "(photo-)crosslinkable gelatin derivatives for biofabrication applications," *Acta Biomaterialia*, vol. 97, pp. 46–73, 2019.

[181] K. Yue, G. Trujillo-de Santiago, M. M. Alvarez, A. Tamayol, N. Annabi, and A. Khademhosseini, "Synthesis, properties, and biomedical applications of gelatin methacryloyl (gelma) hydrogels," *Biomaterials*, vol. 73, pp. 254–271, 2015.

[182] E. E. Antoine, P. P. Vlachos, and M. N. Rylander, "Review of collagen i hydrogels for bioengineered tissue microenvironments: characterization of mechanics, structure, and transport," *Tissue engineering. Part B, Reviews*, vol. 20, pp. 683–696, Dec. 2014.

[183] S. V. Vlierberghe, E. Schacht, and P. Dubruel, "Reversible gelatin-based hydrogels: Finetuning of material properties," *European Polymer Journal*, vol. 47, no. 5, pp. 1039–1047, 2011.

[184] L. Knezevic, M. Schaupper, S. Mühleder, K. Schimek, T. Hasenberg, U. Marx, E. Priglinger, H. Redl, and W. Holnthoner, "Engineering blood and lymphatic microvascular networks in fibrin matrices," *Frontiers in Bioengineering and Biotechnology*, vol. 5, p. 25, 2017.

[185] M. Markovic, J. van Hoorick, K. Hölzl, M. Tromayer, P. Gruber, S. Nürnberger, P. Dubruel, S. van Vlierberghe, R. Liska, and A. Ovsianikov, "Hybrid tissue engineering scaffolds by combination of three-dimensional printing and cell photoencapsulation," *Journal of nanotechnology in engineering and medicine*, vol. 6, no. 2, pp. 0210011–210017, 2015.

[186] M. Tromayer, A. Dobos, P. Gruber, A. Ajami, R. Dedic, A. Ovsianikov, and R. Liska, "A biocompatible diazosulfonate initiator for direct encapsulation of human stem cells via two-photon polymerization," *Polym. Chem.*, vol. 9, no. 22, pp. 3108–3117, 2018.

[187] L. Yang, A. Münchinger, M. Kadic, V. Hahn, F. Mayer, E. Blasco, C. Barner-Kowollik, and M. Wegener, "On the schwarzschild effect in 3d two-photon laser lithography," *Adv. Optical Mater.*, vol. 7, p. 1901040, Nov. 2019.

[188] C. Zaiontz, "Real statistics using excel."

[189] D. Bates, M. Mächler, B. Bolker, and S. Walker, "Fitting linear mixed-effects models using lme4," *Journal of Statistical Software; Vol 1, Issue 1 (2015)*, Oct. 2015.

[190] A. M. Kloxin, M. W. Tibbitt, and K. S. Anseth, "Synthesis of photodegradable hydrogels as dynamically tunable cell culture platforms," *Nature Protocols*, vol. 5, no. 12, pp. 1867–1887, 2010.

[191] A. M. Kloxin, M. W. Tibbitt, A. M. Kasko, J. A. Fairbairn, and K. S. Anseth, "Tunable hydrogels for external manipulation of cellular microenvironments through controlled photodegradation," *Adv. Mater.*, vol. 22, pp. 61–66, Jan. 2010.

[192] M. Tamura, F. Yanagawa, S. Sugiura, T. Takagi, K. Sumaru, and T. Kanamori, "Click-crosslinkable and photodegradable gelatin hydrogels for cytocompatible optical cell manipulation in natural environment," *Scientific Reports*, vol. 5, no. 1, p. 15060, 2015.

[193] V. X. Truong, K. M. Tsang, G. P. Simon, R. L. Boyd, R. A. Evans, H. Thissen, and J. S. Forsythe, "Photodegradable gelatin-based hydrogels prepared by bioorthogonal click chemistry for cell encapsulation and release," *Biomacromolecules*, vol. 16, pp. 2246–2253, July 2015.

[194] K. M. C. Tsang, N. Annabi, F. Ercole, K. Zhou, D. J. Karst, F. Li, J. M. Haynes, R. A. Evans, H. Thissen, A. Khademhosseini, and J. S. Forsythe, "Facile one-step

micropatterning using photodegradable gelatin hydrogels for improved cardiomyocyte organization and alignment," *Adv. Funct. Mater.*, vol. 25, pp. 977–986, Feb. 2015.

[195] S. Žigon Branc, M. Markovic, J. Van Hoorick, S. Van Vlierberghe, P. Dubruel, E. Zerobin, S. Baudis, and A. Ovsianikov, "Impact of hydrogel stiffness on differentiation of human adipose-derived stem cell microspheroids," *Tissue Engineering Part A*, vol. 25, pp. 1369–1380, Jan. 2019.

Abbreviations

AFM	Atomic force microscope
AOM	Acousto optical modulator
ASC	Adipose-derived stem cell
DAS	Tetrapotassium 4,4'-(1,2-ethenediyl)bis[2-(3-sulfophenyl) diazenesulfonate]
ds	Degree of substitution
DSSA	4,4'-Diazido-2,2'-stilbenedisulfonic acid
EBM-2	Endothelial Cell Basal Medium-2
EC	Endothelial cell
ECM	Extra cellular matrix
EGM-2	Endothelial Cell Growth Medium-2
EPC	Endothelial progenitor cell
FCS	Fetal calf serum
Gel-MA	Gelatin methacryloyl
Gel-SH	Thiolated gelatin
HUVEC	Human umbilical vein endothelial cell
Li-TPO-L	Lithium (2,4,6-trimethylbenzoyl)phenylphosphinate
LSM	Laser scanning microscope
MIP	Maximum intensity projection
MMP	Metalloproteinase
MSC	Mesenchymal stem/ stromal cell
PBS	Phosphate buffered saline
PEG-(oNB-A)$_2$	Poly(ethylene) glycol-(o-nitrobenzyl acrylate)
SMC	Smooth muscle cells
TE	Tissue engineering
UV	Ultraviolet
VEGF	Vascular endothelial growth factor
VTE	Vascular tissue engineering